



HAL
open science

Super-resolution microscopy by saturated speckle illumination

Marco Pascucci

► **To cite this version:**

Marco Pascucci. Super-resolution microscopy by saturated speckle illumination. Optics [physics.optics]. Université Paris V Descartes, 2017. English. NNT: . tel-02573823

HAL Id: tel-02573823

<https://theses.hal.science/tel-02573823>

Submitted on 8 Jun 2020

HAL is a multi-disciplinary open access archive for the deposit and dissemination of scientific research documents, whether they are published or not. The documents may come from teaching and research institutions in France or abroad, or from public or private research centers.

L'archive ouverte pluridisciplinaire **HAL**, est destinée au dépôt et à la diffusion de documents scientifiques de niveau recherche, publiés ou non, émanant des établissements d'enseignement et de recherche français ou étrangers, des laboratoires publics ou privés.



UNIVERSITÉ
PARIS
DESCARTES



THÈSE DE DOCTORAT

en physique optique

École Doctorale: Physique en Île-de-France

présentée par:

Marco Pascucci

sujet:

Super-resolution microscopy
by saturated speckle illumination

pour obtenir le grade de

DOCTEUR de l'UNIVERSITÉ PARIS DESCARTES

Soutenance le 30 Octobre 2017 à Paris, devant le jury composé de:

Dr. Sophie Brasselet
Dr. Allard Pieter Mosk
Dr. Ori Katz
Dr. Jacques Boutet de Monvel

Rapporteur
Rapporteur
Examineur
Examineur

Dr. Valentina Emiliani
Dr. Marc Guillon

Directrice de thèse
Co-directeur de thèse

Acknowledgements

A thesis manuscript is just too small to narrate the whole adventure of three years of Ph.D. research. It is conceived to demonstrate the scientific maturity of the student, therefore it does not leave much space for all the people and circumstances which made it all possible to happen. I believe that it is only fair to do justice here and say *thank you* to the amazing people that walked the long distance all along with me.

My greatest reconnaissance goes to my advisors, Valentina Emiliani and Marc Guillon. The former for being a wise and understanding person and a motivating and trustworthy leader. The latter for his great encouragement, continuous teaching and inspiring scientific ideas, and above all, for having always and surely been there when I needed (consciously or not). I had the honour to be his first student and I learnt from our encounter, besides great science, to believe in one's own ideas and follow them, in spite of the first appearances.

I wish to thank the exceptional jury that made me the honour of accepting to examine my work. My reviewers Pr. Sophie Brasselet and Pr. Allard Pieter Mosk and examiners Dr. Ori Katz and Dr. Jacques Boutet de Monvel. Some of them are coming from far away: I did and will do my best to make this manuscript and its presentation worth their long journeys.

A special thanks goes to Sivaramakrishnan Ganesan, an excellent master student (and a friend now) who shared with me the last intense six months of experiments, for his commitment, kindness and his constant optimism. I also acknowledge Laura Caccianini and Dr. Julien Pernier (Curie Institute - Paris), Dany Khamsing and Dr. Brigitte Delhomme (Université Paris Descartes), for their help in the choice and preparation of the biological samples and for providing us with other useful material.

Dimitrii, Alexis, Marta and all the amazing people from the Neurophotonics laboratory in Paris deserve great reconnaissance for their careful reading of this manuscript, for their invaluable support, instructive remarks and interesting lunch (...and dinner) conversations. A special acknowledgement goes to Pr. Gilles Tessier, for his help and advices. I am grateful to Mme Sylvie Hénon and the doctoral school for offering me interesting formations and following the evolution of my work.

I sincerely wish to acknowledge the astonishing open-source software community, that gave me the best tools for realizing this work.

Clara, Federico, Luca, Igazio, Yanis Ouabdesselman, Matteo, Laura Dora Piero e tutta Radio Parigi, Ghislaine, Bernard et tous les Huynh, Zippo, Errichetta Underground, Kosmopolitevitch Orkestra, Warrior Guareschi, Elli and Savvia, Yanik et le crew de Villa Samba 2.0, Samuel, Juliette, Valentine, Ottavia, Marco and his puppet theatre, le BBQBB, la fanfare Khusek, l'orchestre Nymphonique de Paris, la fanfare au Carreau du Temple, Aïe-Aïe, l'Orchestre de scene du Theatre de Montreuil, les Zôtres, le Cnam, have all been my precious fuel during this last intense months and all along these three amazing years.

Many other people did not contribute directly to this adventure but made it possible with their love, friendship and patience, I cannot cite all of them here, it would require another manuscript, but I reserve the rest of my life to thank them every day for being around.

Ma tra queste, due persone eccezionali, conoscendo tutta la storia, credo che saranno particolarmente orgogliose. Dedico loro questo lavoro: a Tamara e Francesco.

Foreword

I remember that, three years ago, when I was starting my Ph.D. work, a friend told me: "a Ph.D. is a tremendous effort, a stressful sacrifice and an excruciating personal journey, but when you finally get it, eventually you're happy to have it... like a baby." As of today, I must admit that he was absolutely right, at least for the first part of the expression, the second lacking the experimental evidence to be verified yet.

Marc, my advisor, is undoubtedly a brilliant scientist, but initially the dense and concise scientific content of his speech was difficult for me to understand clearly. At the beginning of my adventure in France, my French was a little bit too Italian, I didn't have the smallest idea of what working in a laboratory means and was starting to deal with a field totally new to me. So, at that time, Marc's speech seemed to me something more similar to a randomly-generated signal than an information-rich message. Even if I felt that some degree of coherence was there. Only now that I look back, I see how many things I have learned from this slow and intense deciphering and analysis process.

This short personal story helps me to introduce my thesis subject. Very often it happens, indeed, that someone's noise is someone else's signal and where a person sees only chaos, another might find useful and precious information, if he/she learns to mine it. I find this concept fascinating. Maybe for the same reason for which I love learning languages in a broader sense, from human to programming languages through drawing, mathematics and music.

Learning a language is a highly rewarding experience: I believe that this comes from the fact that our brains are made for this task. This rewarding feeling must also be the reason why babies spontaneously learn their mother tongue. When one learns a new language, he slowly discovers patterns and schemes, in a recursive compression mechanism which is driven by memory optimization.

For these reasons, maybe, when I saw the effect of disordered scattering and the possibility of finding useful information in the resulting apparently random speckle patterns, all this seemed to me a familiar topic, something on which I had speculated often before. I believe I made my point: when I write "this thesis is dedicated to saturated speckle imaging, a novel technique which uses speckle patterns as a super-resolution imaging tool", it might sound very technical and arid, but in reality it means only "this thesis is dedicated to learning a new language".

Contents

1	Super-resolution microscopy and scattering	1
1.1	Super-resolution microscopy	1
1.1.1	Optical resolution and super-resolution	1
1.1.2	Numerical deconvolution	4
1.1.3	Physical super-resolution	7
1.1.4	Super-resolution in biological samples	20
1.2	Diffusion of light in random media	21
1.3	Imaging with speckles	24
1.3.1	Exploiting some knowledge of the diffraction process	24
1.3.2	Double blind speckle imaging	25
1.4	Motivation and outlook of this thesis	29
2	Speckle for super-resolution	31
2.1	Characteristics of speckle patterns	31
2.1.1	Phase singularities in speckle patterns	34
2.2	Speckle/STED analogy	37
2.3	Imaging the phase singularities in a speckle pattern	42
2.3.1	The bleaching/imaging setup	42
2.3.2	Photo-bleaching model	43
3	Imaging with Saturated Speckle Patterns	51
3.1	The saturated speckle scanning microscope	52
3.2	Super-resolution speckle imaging	58
3.2.1	Principle	58
3.2.2	Super resolution imaging of fluorescent nano beads	61
3.2.3	Images of actin filaments	63
3.2.4	The finest reachable resolution is NA-independent	66
3.2.5	Noise and bleaching	70
3.2.6	Blind reconstruction	72
3.2.7	On the axial component in random wave-fields.	76
3.3	3D reconstruction by 2D scanning	78
3.3.1	Speckle orthogonality	78
3.3.2	Exploiting speckle orthogonality for 3D imaging	83
4	Conclusions	87
	Appendices	91
A	Speckles	93
A.1	Model of a speckle pattern	94
A.2	Amplitude distribution	95
A.3	Intensity distribution	95
A.4	Grain size	99
A.5	Distribution of fluorescence in saturated speckle patterns	103
A.6	Eccentricity of the phase singularities	106

B	Noise model in saturated speckle patterns	111
C	Fluorescence model under pulsed illumination	113
D	Wiener and RL deconvolution	117
E	Acronyms	119

Chapter 1

Super-resolution microscopy and scattering

This thesis is dedicated to saturated speckle imaging, a novel technique which uses speckle patterns as a super-resolution imaging tool.

This technique and the principal result obtained with it are deeply discussed in chapters 2 and 3, while chapter 1 contextualizes our work.

In this chapter we present the primary ingredients of our study. Namely in section 1.1 we will introduce the concept of super-resolution optical microscopy. We will also discuss the application of super-resolution in complex media, such as biological tissues, where scattering is a major issue. Section 1.2 covers this topic and introduces some first considerations on speckle patterns. In section 1.3 we illustrate how imaging is possible exploiting the properties of speckle patterns and describe the imaging techniques that made use of such a random illumination.

The motivations and outlines of this work are summarized in section 1.4.

1.1 Super-resolution microscopy

1.1.1 Optical resolution and super-resolution

Optical resolution

The resolution of an imaging instrument is its ability to resolve details in the object that is imaged. Due to the wave nature of light, all classical optical systems (microscopes, telescopes, cameras...) are intrinsically limited in resolution by diffraction laws.

If an object is smaller than the resolution of an optical system¹, it is considered *point-like* because the system loses any details of the object's shape. The image of such a point-like object is called Point Spread Function (PSF). The PSF is larger than the object itself and its shape depends only on the system, therefore, it can be regarded as the system's "impulse response",

¹ensemble of one or more optical elements (lenses, mirrors, ...) used to produce images. Microscopes, cameras, and telescopes are examples of optical systems.

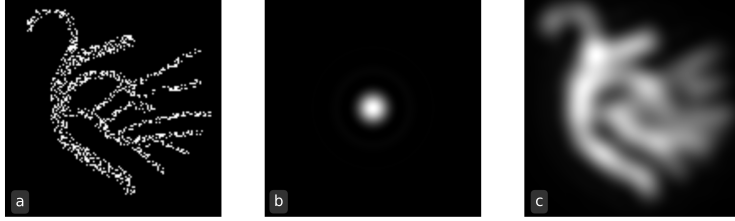


Figure 1.1 – An object (a) is imaged with a the PSF showed in (b). The resulting image (c) is a blurred version of the object.

which means that every point in the image is mapped by the system into a replica of the PSF, as illustrated in fig. 1.1, or in more precise terms, the obtained image is a convolution of the object and the system's PSF:

$$i(\mathbf{x}) = h(\mathbf{x}) \otimes o(\mathbf{x}) \quad (1.1.1)$$

where h is the system's PSF, o is the object i the image and \mathbf{x} is a point in the image plane.

Applying a Fourier Transform (FT) to equation (1.1.1), the convolution becomes a multiplication

$$\tilde{i}(\mathbf{k}) = \tilde{h}(\mathbf{k})\tilde{o}(\mathbf{k}) \quad (1.1.2)$$

Here \mathbf{k} is a point in the reciprocal space (i.e. the space of spatial frequencies). $H = \tilde{h}$, is the FT of the PSF and is called Optical Transfer Function (OTF). In this representation, we do not consider the real images but their spectrum, obtained by FT, and represented by the operator $\tilde{}$ (*tilda*). Small details in an image correspond to high frequencies in its spectrum, as illustrated in figure 1.2.

We make the assumption that an object's spectrum features much higher frequencies than afforded by the system's resolution, meaning that it contains infinitely small details. Saying that all optical systems have a finite resolution, is equivalent to affirm that they operate like low-pass filters: the spectrum of the images that can be produced is limited in frequency. The higher this limit, the smaller the detail that a system can resolve. In equation (1.1.2) the spatial filtering operated by the optical system is represented by the multiplication² of the object the object $\tilde{o}(\mathbf{k})$ by \tilde{h} .

Whatever the representation (in real or reciprocal space), there is not such thing as an imaging system with an infinitely small PSF or equivalently, an OTF with unlimited support. A direct consequence is that if two point-like objects are closer than the PSF size, it is difficult, or even impossible to distinguish them.

Empirically, the resolution of an optical system such as a microscope can be defined as the

²if the images are represented as matrices of pixels, this operation is an element-wise multiplication.

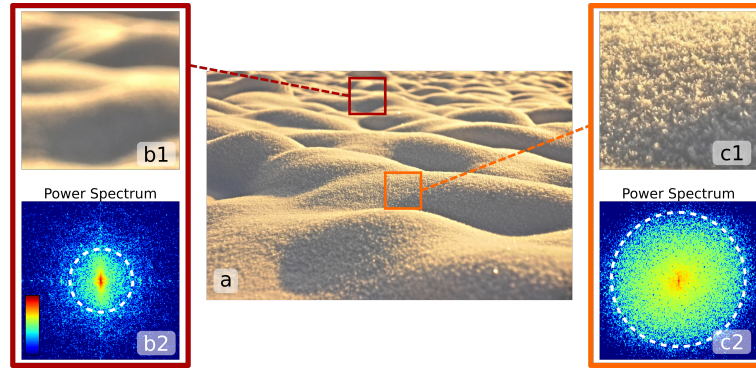


Figure 1.2 – The extension of the powers spectrum of an image increases with the level of details that it features. (b1) and (c1) are two details of image (a). The respective power spectra are plotted in (b2) and (c2). (b1) is blurred by because it corresponds to a portion of the image which was not perfectly at focus, whereas (c1) is sharp and we can distinguish the grains of sand. This finesse of the detail reflects in the extension of the power spectra.

minimum distance R at which two points in the object can be distinguished (e.g. Rayleigh criterion[F.R79]). The smallest detail that a system can resolve depends on the collecting aperture of the objective lens and is given by:

$$d = \frac{\lambda}{2n \sin(\theta)} = \frac{\lambda}{2NA} \quad (1.1.3)$$

where λ is the system wavelength and $NA = n \sin(\theta)$ is its Numerical Aperture defined, with respect to the optical axis, as the maximum half-angle θ of the cone of light that can enter or exit the system, times the refractive index n of the medium between the last lens of the system and the object (see schematic representation in figure 1.3).

This intrinsic resolution limit was demonstrated in the late XIX century by Abbe [Abb81]. It corresponds roughly to half of the wavelength of the light used. A minimum value of d can be obtained evaluating equation (1.1.3) in the best possible conditions, i.e. with the shortest visible wavelength ($\simeq 400$ nm) and the best objective (aberration-free, $NA \simeq 1.4$). This value ($\simeq 200$ nm) represents the classical resolution limit of traditional optical microscopy.

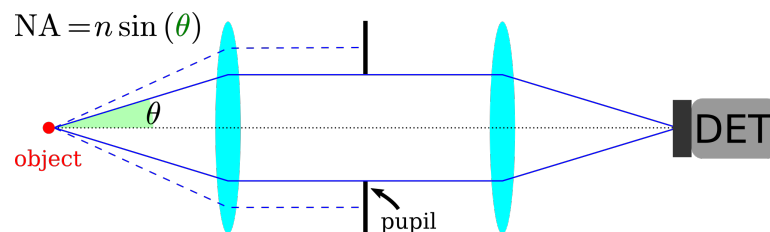


Figure 1.3 – Scheme of a simple imaging system, illustrating the maximum half-angle α of the cone of light that can enter or exit the system, used to define the Numerical Aperture $NA = n \sin(\alpha)$.

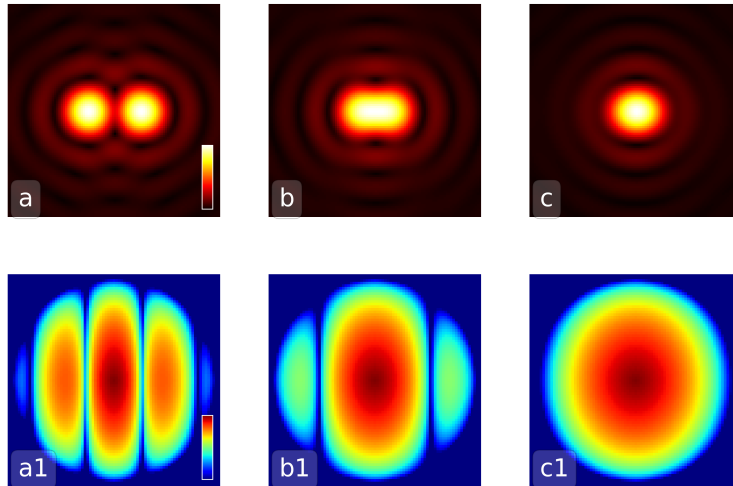


Figure 1.4 – two point-like objects imaged with the PSF of a perfect lens (Airy disk) and their respective (zoomed) power spectra. When the points get too close, they can not be distinguished, which corresponds to the disappearance of the fringe pattern in the power spectrum.

This limit, considered definitive at the time of its discovery, has recently been broken and it is now possible to perform **super-resolution** (SR) imaging (with a better detail than what allowed by diffraction). Super-resolution does not mean that a systems can be physically designed to break the diffraction laws, but that some smart ideas can be applied to pass some "extra" information, that would be normally blocked by the system, through the allowed bandwidth. This supplementary information belongs to details which are smaller than the PSF size, or equivalently, to frequencies that lie outside the system's OTF support. Only in this sense a super-resolution optical system can be said to have a PSF smaller than (or an OTF broader than) those allowed by the classical diffraction limit.

1.1.2 Numerical deconvolution

One way of increasing an image resolution consists in numerically compensating the blurring caused by the finite size of the PSF of the optical system. This is the approach of *deconvolution microscopy* and, since its introduction in 1983[Aga84], it has become a very popular and broadly used technique. It has the advantage to be a completely numerical approach that does not require any special apparatus and can be applied to potentially all kind of microscopy techniques, also to 3-dimensional data[Sib05]. In this section we describe this technique.

In analogy with eq. (1.1.1) we think of an imaging system as a function with a real object

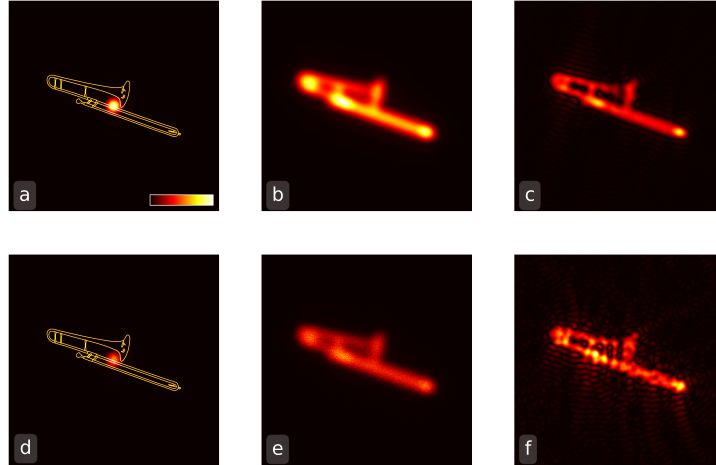


Figure 1.5 – Numerical simulation of deconvolution. An object (trombone) is represented in (a) together with an imaging PSF which is used to image it. The resulting image is the convolution of the object and the PSF (b). By deconvolving the image with exactly the same PSF, the object is partially recovered (c). If a random noise (here Poissonian) is added in the process, the reconstruction is degraded (d,e,f).

O as an input and its image I as an output.

$$I = HO \quad (1.1.4)$$

The imaging process is represented by an operator H , which can easily be identified with the system's PSF and operates on O to produce its image I .

Digital deconvolution is a mathematical process that computes an object's approximation \hat{O} , or in more technical terms, an estimate, given the acquired image I and some model of the imaging function \hat{H} .

$$\hat{O} = \hat{H}^{-1}I \quad (1.1.5)$$

It is important to point out that the notation \hat{H}^{-1} in equation (1.1.5) is only symbolic. Generally, since the application of H on O implies a loss of information, it is not invertible. The "hat" symbol is used to remind the reader that \hat{H} is only an approximation of H , both because H cannot be inverted and because its knowledge is generally only partial. Moreover, in practice, the presence of noise makes the problem much more delicate (see figure 1.5). Taking into account the noise N , we can get a more realistic version of eq (1.1.5):

$$I = HO + N \quad (1.1.6)$$

Usually our knowledge of N is limited to some statistical properties, making image retrieval

more difficult.

The deconvolution problem, as an image-restoration problem, belongs to the ill-posed problem category, meaning that the uniqueness of the solution is not guaranteed. even iMany deconvolution algorithm exist[Sib05, SDS⁺17], some of them are iterative, others make use of some statistical assumptions or constraints, blind-deconvolution algorithm assume that also the PSF is unknown. But they all try to reconstruct the most probable object³, which could have generated the detected image, by using an image representing the system's PSF⁴. Unfortunately, there is no such thing as the best deconvolution algorithm: one might be better than another depending on the specific imaging condition and sample features. Whatever the algorithm, computational image restoration tries to assign out-of-focus intensity back to its originating position in space, resulting in a significantly improved image contrast and a modest increase in spatial resolution[SHL10].

As previously said, deconvolution is intrinsically limited by the fact that some information is completely lost during the imaging process, therefore an image cannot be recovered with infinite detail, even if the system's PSF were known with infinite precision. Moreover, most of the proposed algorithms assume the PSF to be translation-symmetric and, unfortunately, the PSF (often) depends on position in the object space. Moreover, even if the system is aberration-free, any local aberration introduced by the sample itself makes deconvolution imprecise.

In conclusion, even though deconvolution is practical because it does not need any highly engineered system or sample and allows an increasing of the image contrast and a small gain in resolution, it does not transform a traditional microscope in a "nanoscope". To reach that scale of detail, the rules of the game need to be changed and, as said before, one has to violate of some traditional assumptions on optical microscopy.

³in the sense of the minimization of a likelihood function, specific to a given the algorithm

⁴an image of the system PSF cab be obtained by imaging a point object, by the definition of PSF.

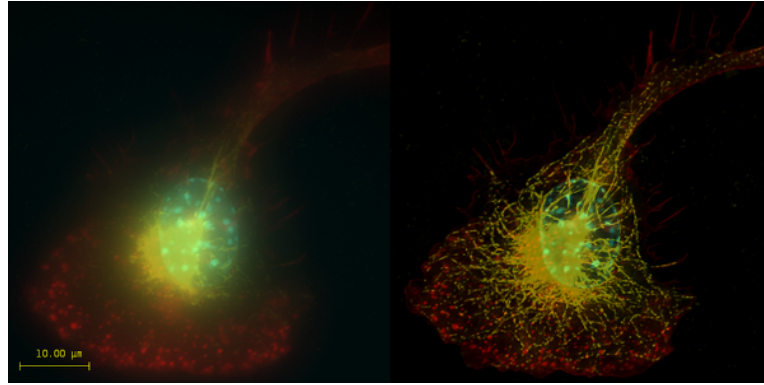


Figure 1.6 – Image of a labelled macrophage, before and after numerical deconvolution (image source: Dr. James Evans, Whitehead Institute, MIT Boston MA, USA).

1.1.3 Physical super-resolution

When discussing the classical optical resolution limit we silently accepted two hypothesis: the illumination is uniform in the sample and the sample's response to the illumination intensity is linear. The relaxation of these hypothesis is the great idea behind the super-resolution techniques that have physically broken the diffraction barrier and allowed to reach a detail which was considered impossible in optical microscopy (some example images are shown in figure 1.7).

The main ingredients that allow this result are, of course, the recent advancements in optics, molecular engineering⁵ and computational power, but at the very heart lays the great intuition on releasing the aforementioned assumptions.

In the following section we give a general idea of what the term "super-resolution" is referred to, and explain the ideas underlying the most popular techniques.

Non-uniform illumination

A way to increase image resolution consists of using non-uniform illumination. This is the basic principle of *Structured Illumination Microscopy* (SIM)[Gus00,HJC02].

In SIM the sample is illuminated with patterned light (e.g a grid-like periodical fringe pattern) that only excites some parts of the sample, while others stay dark. From the interaction between the illumination pattern and the sample's features some information can be extracted which would not be accessible in uniform illumination.

The concept of aliasing is very close to the principle of SIM. Aliasing occurs when sampling a signal at a frequency which is lower than its characteristic frequency. The result is the

⁵super-resolution microscopy was awarded the Nobel Prize of Chemistry in 2014.

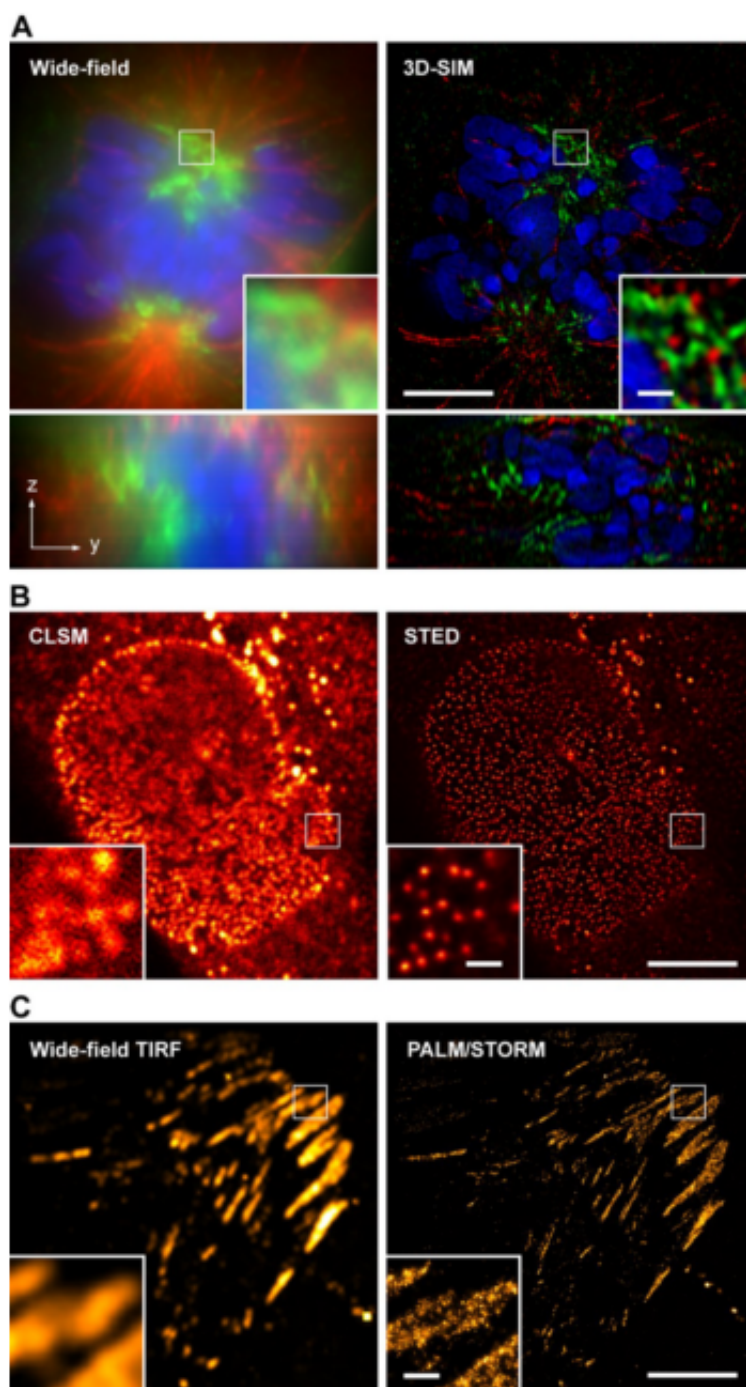


Figure 1.7 – Super-resolution microscopy of biological samples. (A) Conventional wide-field image (left) and 3D-SIM image of a mouse C2C12 prometaphase cell. The bottom panel shows the respective orthogonal cross sections. (B) HeLa cell. The image was acquired with a TCS STED confocal microscope (Leica). (C) Hep G2 cell. The image was acquired using TIRF illumination. Single molecule positional information was projected from 10,000 frames recorded at 30 frames per second. On the left, signals were summed up to generate a TIRF image with conventional wide-field lateral resolution. Bars: 5 μm (insets, 0.5 μm). Image source [SHL10].

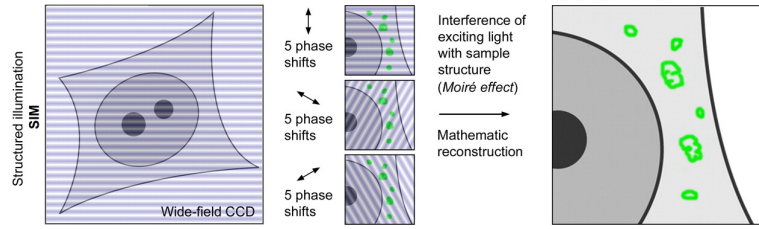


Figure 1.8 – Schematic principle of SIM (Image source [SHL10]).

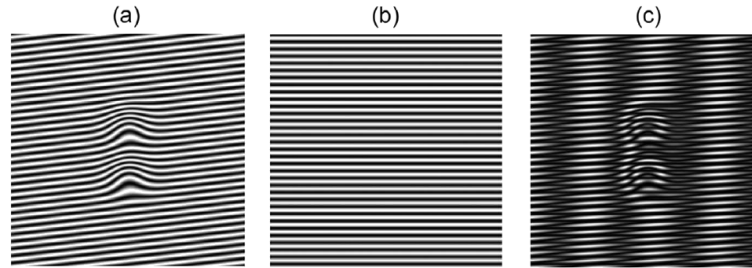


Figure 1.9 – (a), a sample containing unknown structures, (b) a known structure patterns, (c) the moiré pattern generated by overlapping. Image source [LC11].

appearance of low frequency artifacts which depend on both the sampling and the signal frequency and therefore encode a partial information on the actual signal. In SIM, the object is the signal and the sampling is given by structured illumination.

Alternatively, *Moiré fringes* are often used as a similitude to explain SIM (fig. 1.9). They appear when overlaying similar but not identical patterns. In SIM one of the two patterns (illumination) is known, the other pattern is the unknown sample. Though the *Moiré fringes* are aesthetically attractive and depict well the interaction between sample and illumination, they do not clearly illustrate the basic principle of SIM.

SIM enhances spatial resolution by collecting information from outside the allowed region in the reciprocal space, i.e. outside the OTF support of the imaging system. This information is encoded in every SIM image at a lower spatial frequency, which is allowed to pass through the system. With a linear combination of several SIM images, it is possible to extract the higher frequency signal, obtaining *de facto* a reconstructed image with a wider spectrum than what allowed by the system's OTF. A wider spectrum corresponds to a finer detail, whence the super-resolution.

What follows is a non-rigorous, but explicative example for a better understanding of SIM. Imagine we can produce a modulated illumination in the sample with an intensity I_e given by:

$$I_e = 1 + \sin(\mathbf{k}_0 \cdot \mathbf{x}) \quad (1.1.7)$$

Where \mathbf{x} is the coordinate in the sample plane and \mathbf{k}_0 the modulation wave vector. The

corresponding image acquired by the system is then:

$$I_{det}(\mathbf{x}) = [I_e(\mathbf{x}) \times O(\mathbf{x})] \otimes \text{PSF}(\mathbf{x}) \quad (1.1.8)$$

And the corresponding FT is:

$$\widetilde{I}_{det}(\mathbf{k}) = [\widetilde{I}_e(\mathbf{k}) \otimes \widetilde{O}(\mathbf{k})] \times \text{OTF}(\mathbf{k}) \quad (1.1.9)$$

$$\widetilde{I}_{det}(\mathbf{k}) = \left[\left(\delta(\mathbf{k}) + \frac{1}{2l} (\delta(\mathbf{k} - \mathbf{k}_0) - \delta(\mathbf{k} + \mathbf{k}_0)) \right) \otimes \widetilde{O}(\mathbf{k}) \right] \times \text{OTF}(\mathbf{k}) \quad (1.1.10)$$

Equation (1.1.10) contains the convolution of the Object FT \widetilde{O} with three delta functions. The first term gives an exact copy of \widetilde{O} , whereas the two others are shifted replicas of it. Then the product with the OTF simply cuts high frequencies which the system does not allow to pass. Nevertheless, thanks to the shifted replicas of \widetilde{O} , a part of the information regarding those higher frequencies is now shifted in the OTF transmission bandwidth. Eventually, with a linear combination of at least 3 images taken with a translated version of the same illumination pattern (i.e. adding a phase in the reciprocal space), it is possible to isolate this high frequency information.

Therefore, with an accurate choice of the pattern orientation (\mathbf{k}_0) and its translation, a wider spectrum of the object can be explored, thus allowing super-resolution.

Here, we presented SIM with fringe illumination for historical reasons but in principle, any pattern containing high spatial frequencies can be used, and in particular speckle patterns[MBG⁺12, LAI⁺16].

SIM is a technique that does not require a very complex optical system nor highly sophisticated reconstruction algorithms. On the other hand, the widening of the spectrum obtained does not allow more than a factor 2 (compared to uniform illumination) in resolution enhancement[LC11]. In order to push this limit even forward, we need to break the linearity assumption on the sample response.

Non-linear response

Even though structured illumination, as seen in section 1.1.3, allows already super-resolution, the best results obtained in this field come from the violation of the assumption that the sample responds linearly to illumination. A linear response is what is usually expected from a microscope: the sample is visible when one shines light on it, dark otherwise, and the brighter the illumination, the stronger the measured signal.

Many well established super-resolution techniques such as PALM [BPS⁺06] / STORM [RSM⁺12],

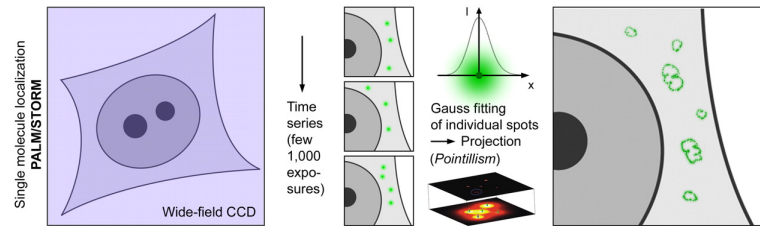


Figure 1.10 – Schematic principle of PALM/STORM. This techniques use uniform illumination but only some FP are stochastically excited. The signal is collected from the isolated FP and numerically fitted to find its centre, which corresponds to the FP location in the sample.(source [SHL10])

STED [HW94a, LGSE13], SSIM[HJC02, Hei03, Gus05], SAX [FKK⁺07, HBE⁺09] and others are based on the idea of getting a non-linear response from the sample. We will briefly describe these techniques in this section.

Stochastic photo-activation/switching super-resolution techniques. As we have seen in section 1.1.1, once a system PSF is known, one knows how a point-like object is imaged by this system. Therefore it is possible to localize a point-like object with extreme accuracy⁶. Moreover, at least in fluorescence microscopy, the light sources are fluorescent molecules, which can be indeed regarded as point-like objects in comparison to the classical resolution limit. This means that one emitting light molecule can be extremely well located in space. This super-localization is possible as long as light is emitted by a single and well isolated emitter⁷. This is the case of *sparse* samples, where the fluorescent objects are small and separated, and this is not the general case. Usually, for example in biology, tissues are dyed with high densities of fluorescent molecules. Nevertheless, if one can get light emission from one molecule at a time, while the others stay dark⁸, each emission can be attributed to a well determined location in the sample with a very high precision, well beyond the diffraction limit.

Two very well known super resolution techniques (among others) rely on this idea: Photo-Activated Localization Microscopy (PALM) [BPS⁺06] and Stochastic Optical Reconstruction Microscopy (STORM)[RSM⁺12]. In both of them the fluorophores (FP) in the sample are stochastically switched between a light emitting and a dark state in order to isolate them. Even though PALM and STORM are based on the same idea, they differ basically on the kind of optical transition addressed by the switching process.

⁶For example if the system PSF is centro-symmetric, a point-like object can be localized in the centre of the measured PSF.[SHL10]

⁷The additional information of knowing that signal comes only from an isolated "very small" object makes the crucial difference between localization and deconvolution.

⁸In this case the sample can be considered sparse in the space-time.

PALM was first carried out using a *photo-activable* FP named EosFP[BPS⁺06]. Under normal conditions, EosFP emits green fluorescence at 516 nm. Upon irradiation near 400 nm, its fluorescence changes to 581 nm because of a photo-induced modification[WON09]. This optical property makes it possible to convert a subset of EosFPs to emit in the yellow region (581 nm). When the number of converted proteins is small, the proteins will be well separated and can be imaged (localized) in the yellow region with high resolution. When this particular subset of EosFPs is photobleached, another subset of EosFPs can be converted and imaged. This process may be cycled 10^2 to 10^5 times until the population of EosFPs is depleted. Since then, many other photoconvertible, photoactivatable, and photoswitchable FPs have been developed. Photoactivatable FPs can be activated from a dark state to a bright state using UV light, and photoswitchable FPs can alternatively be switched on or off with specific illumination. A review of these proteins can be found in Ref. [PDMLS10].

STORM[RBZ06] and dSTORM[EH14] differ from PALM in that they use FP which can be reversibly cycled between a fluorescent state and a dark state (photo-switching). The optical switch can be cycled on and off hundreds or thousands of times before becoming permanently photo-bleached. For both techniques a resolution down to ~ 20 nm has been proven in biological samples[SPM⁺09]. fluoro

In all aforementioned super-resolution techniques the scientist has no control on which molecule will be in its fluorescent state, but only, and up to a certain level, on the density of such molecules at a given time. This fact of not knowing *a priori* the position of light emission in the sample classes these super-resolution techniques as stochastic, in contrasts with other SR techniques such as STED, SSIM and SAX, which are called *deterministic*.

These last mentioned techniques rely both on a structured illumination and on a non-linear response of the sample by saturation of an optical transition.

Optical saturation Any system with a limited output is subject to saturation. For all input value larger than a given threshold, the output of the system saturates and remains constant. A fluorescent sample that undergoes an optical transition is a limited output system.

As an example, we will treat here the case of fluorescence excitation, but the same reasoning can be applied to any other optical transition. Let us imagine a uniformly fluorescent sample. A finite and constant portion of it is illuminated by a continuous⁹ light source whose wavelength

⁹a more rigorous and detailed discussion, including the case of pulsed excitation is presented in appendix C.

corresponds to the energy gap between the molecule's ground and excited states. In order to simplify the reasoning let us suppose that only these two states exist. This assumption is reasonable if the transition to other states happens with a much slower rate than fluorescence emission.

In the fluorescence mechanism, an FP molecule in the ground state S_0 must absorb one excitation photon to reach the excited state S_1 and be able to emit a fluorescence photon, thereby decaying back.

Two parameters define the dynamic of this system: k_f the fluorescence rate and k_e the excitation rate. The FP populations in the ground and excited states evolves in time according to these rates. While k_f is a constant value typical of the FP, k_e depends on the FP absorption on the density of excitation photons (excitation intensity I_e).

$$k_e = \frac{\sigma_{abs} I_e}{h\nu_e} \quad (1.1.11)$$

where σ is the FP's absorption cross-section, h is the Plank constant and ν_e is the excitation optical frequency. The fact that k_e is proportional to I_s implies that the probability of excitation increases with the excitation intensity I_e . The reciprocal values $\tau_f = k_f^{-1}$ and $\tau_e = k_e^{-1}$ are the system characteristic times. Obviously τ_e decreases with increasing excitation intensity, whereas k_f is constant and lies for most FP in the range 0.5 ns - 5 ns.

As the excitation intensity increases, since fluorescence is not instantaneous, provokes an accumulation of FP in the excited state and a progressive depletion of the ground state. At the same time, since the population of excited FP increases, so does the fluorescence signal. In CW illumination, a given excitation intensity defines a particular steady-state of the system, where the occupation number of the two levels is constant and is determined by the transition rates. Fluorescence emission is proportional to the occupation number for the excited state, which is

$$r_1(I_e) = \frac{k_e}{k_f + k_e} = \frac{I_e/I_s}{1 + I_e/I_s} \quad (1.1.12)$$

and is plotted in figure 1.11. In the last step we have used eq. (1.1.11) and the saturation intensity $I_s = \frac{k_f \nu_e}{\sigma_{abs}}$ has been introduced. It represents the necessary intensity to obtain $k_e = k_f$, which is an equivalence of the probability of emission and absorption. Note that, in this case, the occupation probabilities of the states are also equal: half of the FP are excited, which means that the fluorescence emitted by the sample is half its maximum value.

Equation (1.1.12) states that, with increasing excitation intensity, r_1 increases up to its maximum value 1. When $r_1 = 1$ the sample emits its maximum fluorescence signal. Further increasing I_e doesn't have any effect. In this sense, the optical transition (here excitation) is

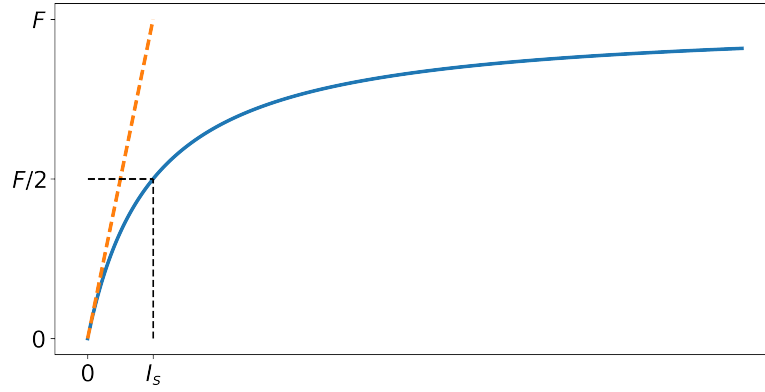


Figure 1.11 – Saturation curve. It represents the Fluorescence response of an ensemble of FP versus the excitation intensity. The FP responds linearly up to a certain excitation intensity, The intensity at which the fluorescence reaches half of its maximum value ($F/2$) is defined as the saturation intensity I_s . Above this value, the FP behaviour is strongly non-linear and the fluorescence signal converges to its maximum value F .

said to be saturated.

When a system saturates, it does not respond linearly to a stimulus, and its output contains higher frequencies than the input; an illustration of this behaviour is proposed in fig. 1.12. In super resolution microscopy, these higher frequencies are exploited to generate sub-diffraction details in the sample [HJC02]. In fact, the image produced by fluorescence microscopy in the linear regime is given by (cf. eq. (1.1.1)) :

$$i = h \otimes I_{em} = h \otimes [\alpha I_e \rho] \quad (1.1.13)$$

where all dependences from the space coordinates have been omitted for the sake of readability. Here I_{em} is the emitted fluorescence intensity, α is the proportionality factor between excitation and fluorescence emission, I_e is the spatial distribution of the exciting light and ρ is the local density of FP in the sample. When excitation is saturated, the previous formula becomes

$$i = h \otimes \hat{I}_{em}(I_e, \rho) \quad (1.1.14)$$

if we assume \hat{I}_{em} to be linear in $\rho(\mathbf{x})$ but non-linear in I_e , we may write

$$\hat{I}_{em}(I_e, \rho) = f(I_e)\rho \quad (1.1.15)$$

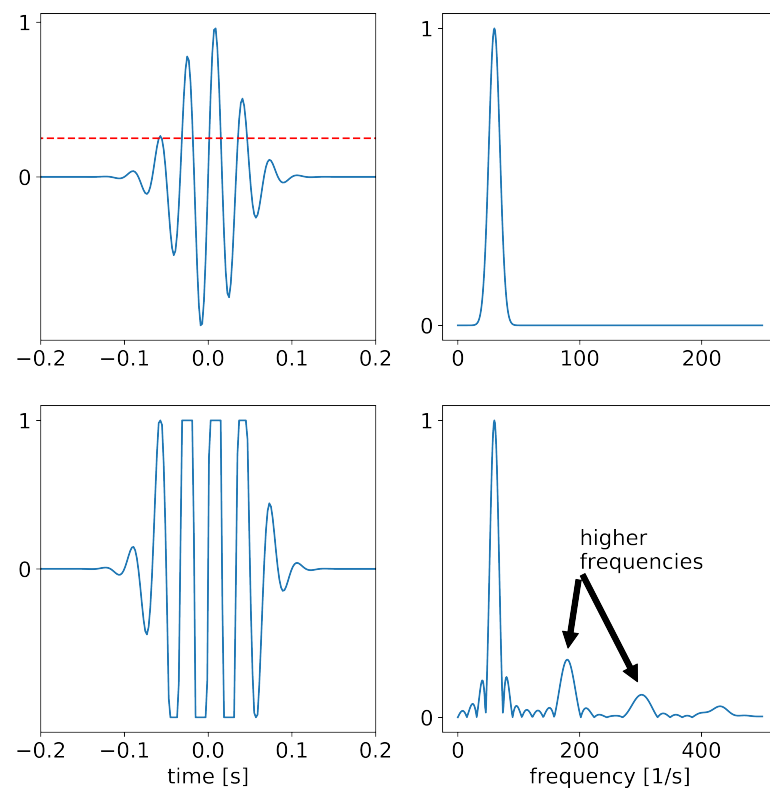


Figure 1.12 – In the first row an input signal (left) and its spectrum (right). The red dashed line represents the saturation input level for an hypothetical limited linear system. The second row shows the saturated-response of this system to the given input, and the corresponding spectrum. Higher frequencies appear as an effect of saturation.

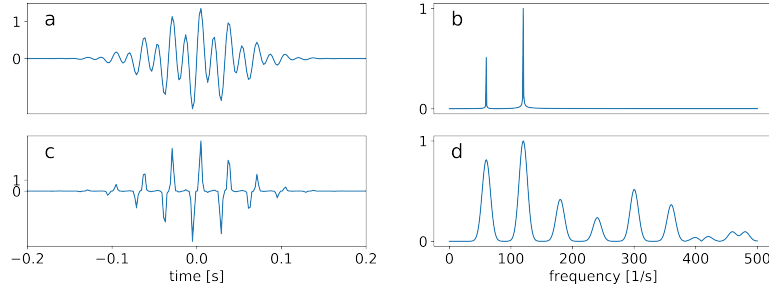


Figure 1.13 – A signal $s(t)$ (a) and its spectrum (b) featuring two strong components. (c) The third power of the signal s^3 and the corresponding spectrum, where higher frequencies appear due to non-linearity. Note that the spectrum of s^3 is $(\tilde{s} \otimes \tilde{s} \otimes \tilde{s})$.

Performing a Taylor expansion in I_e

$$\hat{I}_{em}(I_e, \rho) = \alpha I_e \rho + \sum_{n=2}^{\infty} c_n I_e^n \rho \quad (1.1.16)$$

where the first term corresponds to the linear case (cf. (1.1.13)). The Fourier transform of the emitted intensity is now

$$\widetilde{\hat{I}_{em}} = \widetilde{I_{em}} + \sum_{n=2}^{\infty} c_n [\widetilde{I_e^n \rho}] \quad (1.1.17)$$

In the first term on the right we recognise the FT of the emission intensity in the linear case (cfr. eq. (1.1.13)), which has a bounded support since it is proportional to I_e , whose support is the system's OTF. But the terms of the form $\mathcal{F}[I_e^n]$ in the sum introduce higher frequencies. In fact, the generic term of this sum is equivalent to:

$$[\widetilde{I_e^n \rho}] = [\tilde{I}_e \otimes \tilde{I}_e \otimes \dots \otimes \tilde{I}_e] \otimes \tilde{\rho} \quad (1.1.18)$$

Therefore, the multiple convolutions of \tilde{I}_e introduce higher frequency (as illustrated with an example in figure 1.13), and thus allow to extract more information in the last convolution with $\tilde{\rho}$.

Saturation is a key concept in several super resolution techniques that will be discussed hereafter. To summarize it allows to generate a high frequency response with a low frequency stimulus. In microscopy, this translates into the ability to modify the sample's FP state with a finer detail than what permitted by the diffraction limit.

Super-resolution by saturation. The aforementioned advantages of saturation are exploited in several super-resolution microscopy techniques to retrieve high frequency information on the sample with spatial or temporal modulation of the excitation intensity. In section 1.1.3 we have introduced SIM, which improves the resolution by a factor¹⁰ 2 thanks to structured illumination. With the introduction of saturated excitation, Gustafsson *et al.* have demonstrated a much finer resolution [Gus05] reaching a detail of <50 nm. A similar idea was also implemented in confocal microscopy and gave birth to 2 techniques: Saturated EXcitation (SAX [FKK⁺07]) and Saturated Absorption Competition (SAC [ZKT⁺17]) microscopy. Here, instead of the spatial modulation of light, a temporally modulated excitation is applied.

In theory, the resolution enhancement of all these approaches can be arbitrarily high with appropriated excitation powers, although the real performance is substantially dependent on the brightness and photostability of the fluorophores used. The impact of photostability is even more crucial, since the excitation intensities have to be rather large to reach sufficient saturation. Another issue linked to the high excitation intensities required, is the background signal due to parasitic fluorescence in the sample and optical components.

A slightly different approach is adopted in STimulated Emission Depletion (STED) [HW94b] and with other REversible Saturable (or *switchable*) Optical Linear (Fluorescence) Transition (RESOLFT[KSH07]) techniques. STED, for example, exploits stimulated emission to selectively suppress the spontaneous fluorescence in the sample, thereby confining it in sub-diffraction volumes.

The new super-resolution technique that we present in this work is related to both SSIM and STED. Besides we have applied STED microscopy to obtain some important results reported in chapter 2. Therefore we want spend a few words on the principles of these techniques. Since we have described the former in section 1.1.3, we will now briefly present the latter.

STED microscopy has been shown to reach a resolution down to 2.4 nm [WPS⁺12]. Because STED can obtain nano-scale super-resolution, its approach has been widely used and explored.

A STED microscope is basically a normal fluorescence microscope, where super-resolution is achieved thanks to a second beam which stimulates fluorescence emission in the sample and confines the sample signal in a sub-diffraction sized volume (see fig. 1.14).

The STED beam is produced by adding a spiral phase to a Gaussian beam, thanks to a phase masks (see fig. 1.15). When the beam is focused, the intensity at the focal plane looks like a "doughnut": a bright ring with a dark spot at the focus. Both excitation and de-excitation

¹⁰compared to the resolution limit imposed by diffraction.

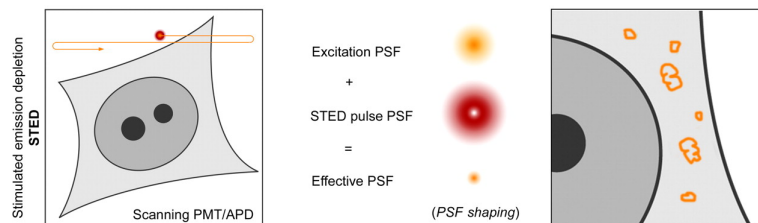


Figure 1.14 – Schematic depiction of the STED microscopy technique. Two beams are used and scanned over the sample: an excitation beam and a doughnut-shaped red-shifted beam that stimulates emission and confines the fluorescence in a sub diffraction volume in the sample.

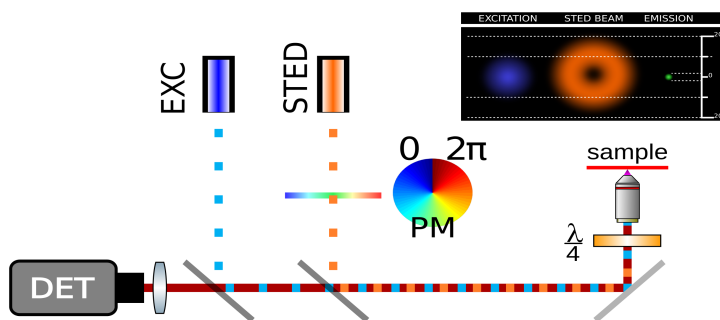


Figure 1.15 – Schematized STED setup. Two pulsed beams are used: one (blue) to excite the FP in the sample and another (orange) to stimulate fluorescence emission. The second beam passes through a spiral phase mask (PM) that gives to it a "doughnut" shape in the sample plane. The optical path difference for the two beams creates a delay between excitation and stimulated emission.

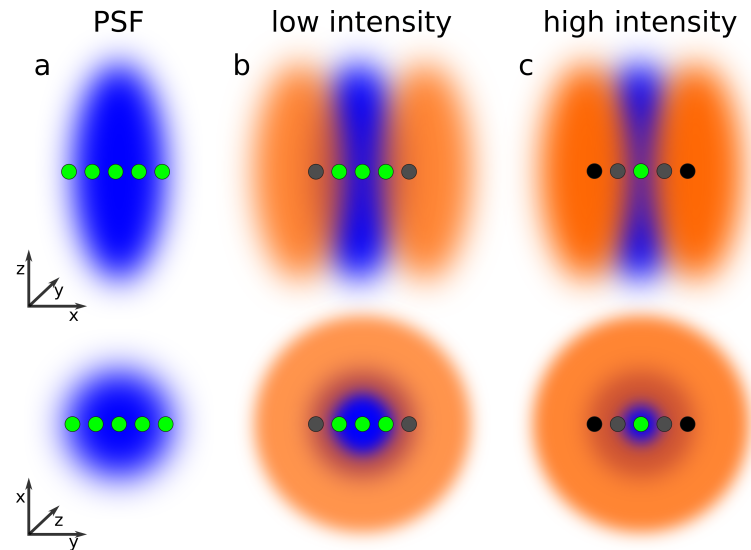


Figure 1.16 – STED doughnut, longitudinal and transversal cut. a) the excitation PSF illuminates a fluorescent sample. b) The doughnut STED beam (orange) de-excites the FP that do not lie in the center. d) with a higher average intensity, fluorescence is confined in a smaller volume.

beams are issued from pulsed laser sources. The "doughnut" beam is red-shifted (to stimulate fluorescence) and it is delayed in comparison to the excitation one. First the sample is excited with a diffraction limited spot by the excitation beam, successively, within a time shorter than the FP mean fluorescence lifetime, the "doughnut beam" impinges on it and stimulates the emission of the excited FP everywhere but at the doughnut centre, where the intensity is zero.

The probability of inducing spontaneous emission from one FP located somewhere in the sample is proportional to the local intensity of the "doughnut" beam, and tends to 1 if this intensity is above the transition's saturation intensity I_s . By increasing the beam's average intensity, it is possible to increase the portion of the STED beam that has an intensity larger than I_s and, with it, the number of excited FP in the sample that undergo spontaneous emission with probability one (depletion). This leads to a contraction of the volume in the sample where FP are still excited after the STED beam impact. The lowest intensity of the "doughnut" beam (see fig. 1.16), is found around its centre, therefore the STED beam confines fluorescence around the doughnut's centre, in a volume whose size decreases with the average intensity of the STED beam.

After depletion, the still excited and confined FP spontaneously emit fluorescence. This signal is collected and measured by a single pixel detector (PMT or APD) and reassigned to a pixel which has the size of the scanning step, which can be arbitrarily small. This process is repeated while scanning the desired field of view in the sample. Ideally the intensity of the STED beam should be high enough to confine the spontaneous fluorescence in a volume which

has a typical size of the scanning step.

As we have seen, the resolution of STED microscopy increases with I_d , the average intensity of the depletion beam. In fact, it depends on the ratio s between I_d and the saturation intensity I_s . This can be modelled by the following relation [HKU⁺08]:

$$d = \frac{\lambda}{2\text{NA}} \frac{1}{\sqrt{1+s}} \quad (1.1.19)$$

where we recognize the classical diffraction limit $\lambda/2\text{NA}$ plus a multiplying factor that decreases with the square root of s for high depletion intensities.

1.1.4 Super-resolution in biological samples

Most of the techniques that we have briefly discussed in the previous sections, are theoretically unlimited in the resolution that they can achieve. In practice, the simple consideration that smaller objects emit lower fluorescence, makes it straightforward that when nanoscale resolution is wanted, each source of noise has to be carefully minimized. Unfortunately, scattering, autofluorescence, sample movement and instability are typical noise sources of complex specimens such as biological objects (cells, tissues...) that limit the practical achievable resolution. So, for example, even if STED has proven to be capable of reaching the nanometer resolution when imaging color centers embedded in a diamond crystal[RWH09] things get rapidly much worse as soon as the sample is less stable.

Perfectly stable samples, on the other hand, can be imaged with other non-optical techniques (electron and atomic force microscopy for example) which are much more adapted. The main advantage of optical microscopy is that it is bio-compatible and allow the observation of living specimens. The ultimate aim of super resolution microscopy is to reach the nano-scale for biological research. Unfortunately the complexity of this kind of sample makes this quest non-obvious.

Biological samples impose many constrains: the dyes must be bio-compatibles and the intensity used must take into account the fragility of the sample to avoid thermal- and photo-damages. All this without considering that tissues absorb and scatter light. Scattering indeed, is an enormous obstacle to super resolution imaging in biological tissues. Due to the randomization of the wave front that occurs there, structured illumination is impossible at a depth of more than typically $100\ \mu\text{m}$ [DTS09, GTL⁺11].

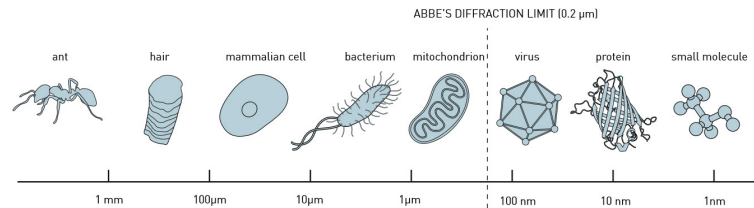


Figure 1.17 – Schematic of the scale of living being and representation of the optical resolution limit.

1.2 Diffusion of light in random media

Our knowledge of life and its mechanism is intimately linked to the technical development of optics. Since the beginning of the XVII century, as the first compound microscope officially came out, scientists have been able to understand the microscopic structure of complex organisms, then, step by step with the understanding of the physics of light propagation, this knowledge has allowed them to penetrate the secrets of the cell, its structure and mechanisms, functions and interactions, and as new and better microscope were built, smaller and smaller object and interaction could be understood. But the wave nature of light puts a limit on the size of the objects that can be imaged. As microscopes reached the subcellular scale, object as small as viruses and proteins still could not be seen with visible light. Light is one of the best means we have to investigate life without damaging it, hence scientists have struggled to overcome the intrinsic limit of resolution of optical microscopy, until recently, when new smart ideas came out to circumvent this limit, as explained in the previous sections. Nevertheless, it has still not yet been possible to image beyond the diffraction limit (i.e. reach super-resolution) in depth in a scattering tissue.

Biological tissues are weak absorbers but strong scatterers¹¹[Ntz10]. The interaction of photons with different cellular structures results in elastic scattering, a process of photon absorption and re-emission without loss of energy but possibly associated with a change in photon direction. For biological structures, the re-emission has a high probability to occur in the forward direction for each scattering event. Despite this, the accumulation of multiple scattering events results in a gradual randomization of the propagation direction[WV11,Ntz10]. This allows to distinguish different scattering regimes which can be identified at different depths in the tissue. A schematic representation of these regimes can be seen in figure 1.18.

The depth limit of conventional microscopy can be derived from a physical parameter called the mean free path (MFP) of a photon. The mean free path (MFP) in tissues is defined as

¹¹scattering in biological tissues is particularly strong in the ultraviolet (< 450 nm), visible (450 nm to 650 nm) and near-infrared (650 nm to 1000 nm) spectral regions owing to photon interaction with cellular structures at these wavelengths.

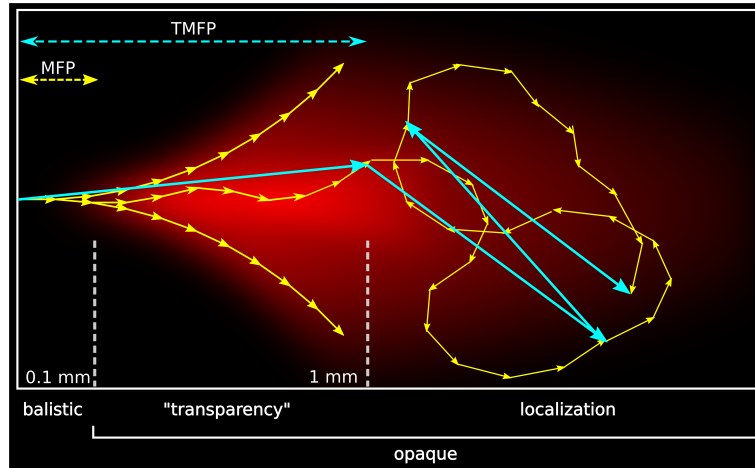


Figure 1.18 – The three different scattering regimes that can be identified in a medium that shows a strong anisotropy. As light penetrates the medium it interacts with it and get scattered. Within a length of one Mean Free Path (MFP) all photons are scattered at least once. For a distance of more than one MFP all ballistic (non-scattered photons), are lost, but due to the medium anisotropy, most of light travels forward, up to a distance of one Transport Mean Free Path. After this depth, the multiple scattering events totally randomize the direction of the light.

$1/\mu$, in which μ is typically expressed as a sum of the tissue's absorption coefficient μ_a and the tissue's scattering coefficient μ_s , that is, $\mu = \mu_a + \mu_s$. As $\mu_s \gg \mu_a$ in most tissues, MFP can be simply written as

$$\text{MFP} = 1/\mu_s.$$

The MFP describes the average distance that a photon travels between two consecutive scattering events. The MFP is of the order of $100 \mu\text{m}$ in tissue, although it varies with tissue type. This means that the bulk of photons propagating through a $100 \mu\text{m}$ tissue slice will experience at least one scattering event, resulting in image blur.

Confocal and multi-photon microscopy have been developed to image specimens at depths where photon scattering occurs (hundreds of micrometers). The penetration limit of these advanced forms of microscopy is governed by a second physical parameter, the transport mean free path (TMFP), which takes into account the MFP and the average angle by which photons are scattered in each scattering event.

When considering a photon undergoing several scattering events, the reduced scattering coefficient can be defined to describe this multiple scattering process as $\mu'_s = \mu_s(1 - g)$, in which g is the scattering *anisotropy*, a measure of the amount of forward direction retained after a single scattering event ¹². For photon scattering in tissue, g is typically 0.8–1. The

¹²if θ is the scattering deflection angle defined in respect to the forward direction before the scattering event, $\cos(\theta)$ is close to one if the deflection is small 0 if perpendicular and negative in case of backward

transport mean free path (TMFP) can then be defined as

$$\text{TMFP} = 1/\mu'_s = \frac{\text{MFP}}{(1-g)} \quad (1.2.1)$$

The higher g , the more forward the scattering and the longer it takes for light to disperse, resulting in higher penetration distances with microscopic techniques. The underlying photon propagation process can be understood if we consider that photons after $(1-g)^{-1}$ scattering events reach a random propagation compared to the direction of the incident beam. Therefore, although the propagation between 0 and 1 MFP is largely ballistic, as the travel distance increases to 1 TMFP, there is increasingly more scattering, eventually leading to photon diffusion. In a few words, TMFP indicates the mean propagation distance that it takes for photons to, on average, lose relation to the propagation direction they had before entering tissue. In many animal and human tissues, TMFP is typically ten times larger than MFP and represents an upper limit of the penetration of microscopic techniques. Confocal or multi-photon microscopy, for example, operate at penetration depths that are smaller than 1 TMFP. Imaging beyond 1 TMFP with optical methods has been traditionally challenging, and sub diffraction resolution still remains unachievable because, with scattering the phase of the field is completely scrambled and spatial information is lost, resulting in an apparently random interference pattern known as speckle (see fig. 1.19).

scattering. g is the expectation value of $\cos(\theta)$

$$g = \overline{\cos(\theta)} = 2\pi \int_0^\pi \rho(\theta) \cos(\theta) \sin(\theta) d\theta$$

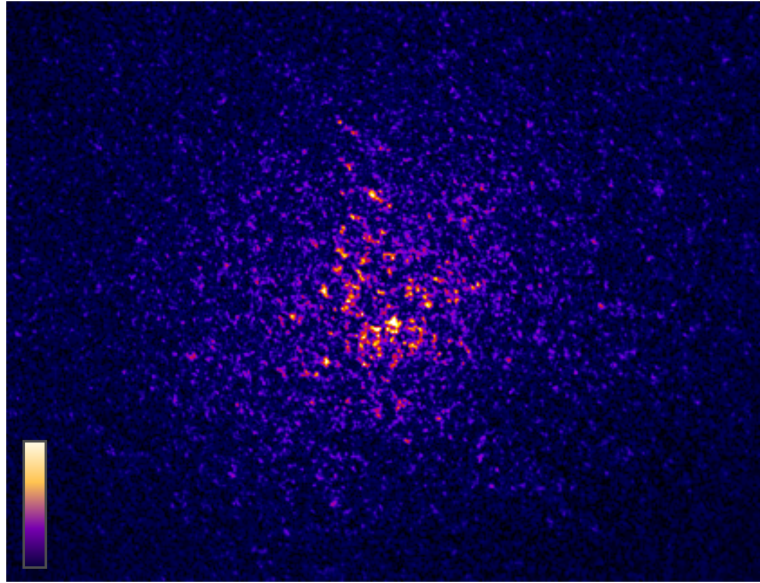


Figure 1.19 – An example of speckle pattern obtained when trying to focus light through a $300\ \mu\text{m}$ thick mouse brain slice. Although most of the energy still remains in a region close to the focal point, the focus is completely lost.

1.3 Imaging with speckles

1.3.1 Exploiting some knowledge of the diffraction process

We have seen in the previous section that diffusion completely scrambles and encrypts spatial information carried by light. Although chaotic, this process is well deterministic and depends on the microscopic structure of the scattering medium that light crosses, which is generally unknown.

Diffusion just encrypts information coming from the sample. Determinism is, of course, not violated and the speckle pattern still carries all information about the source spatial distribution. In fact, an accurate knowledge of the optical properties of the medium, even if difficult to obtain, is sufficient to decrypt the information carried by the speckle pattern and allows imaging through diffusive media[PLC⁺10].

Concerning speckles, a work which is interesting to examine in the context of this thesis has been recently published by E. Edrei *et al.* [ES16]. In their experiments, an object emitting incoherent light was imaged through a scattering medium (1 mm opaque tape). Edrei's approach consists in characterizing the medium's optical properties by taking the speckle image of a point like object through the diffuser. Then a more complex object is imaged through exactly the same diffuser. A simple deconvolution of the object's speckle image with the speckle image of the point object allows an immediate image reconstruction. Measuring the system impulse response is equivalent to know some information on the scattering process. The crucial step

in this technique and other that use a so called "guide star" to gain some knowledge on the diffraction process is that, at a certain point in the imaging process, it is possible to "bypass" the scattering medium and get some extra information (for example the knowledge that the guide star is a point like object).

Unfortunately the process of characterization of the medium's optical properties takes time, it is complicated and not always possible. Nevertheless it has already been shown that, even without this knowledge, imaging can still be performed through scattering layers, as we will see in the following section.

1.3.2 Double blind speckle imaging

The previous examples of speckle-imaging rely on some knowledge of the complex scattering process that takes place in the diffusive media through which the unknown object is imaged. In contrast, a speckle imaging technique is defined *double blind* if this knowledge is not available.

Even if the process of diffusion is completely unknown, some information can be still extracted from the statistical analysis of the speckle pattern that appear as a consequence of complex scattering. This concept was pioneered 1970 by Antoine Labeyrie with "Speckle Interferometry" used to resolve a system of binary stars which appeared as a single object due to diffusion by the atmosphere [Lab70]. Since Labeyrie's work, speckle imaging has evolved and it has been applied to other contexts than astronomy and it is now considered as one of the candidates to the race to in-depth microscopy.

A key concept is that some deterministic transformation can be applied that modify the field in a predictable way, even behind an unknown diffuser. These transformations are obtained by controlling the phase and or polarization of the beam before the diffuser and can be applied cleverly to get precise information about the hidden object.

Probably the most well known way of applying such a deterministic transformation is by exploiting the "**memory effect**"[FKLS88]. This is a peculiar phenomenon observed when light propagates through a scattering medium [FRF88]. Within a certain range of impinging angles (tip-tilt) the speckle patterns observed after the scattering medium are highly correlated and translated over a distance proportional to the impinging angle. From a reciprocal point of view, two incoherent point-objects which are close enough, will result in a superposition of two very similar speckle patterns when imaged through a diffuser. The translation distance within which this effect holds is inversely proportional to diffuser thickness L and directly proportional to the distance s of the diffuser from the screen and can be approximated by the equation $\text{FOV} \approx s\lambda/\pi L$ [Fre90, KSS12]. A consequence of the memory effect is the ability to deterministically exchange critical points of a speckle generated by a diffuser[GRG17].

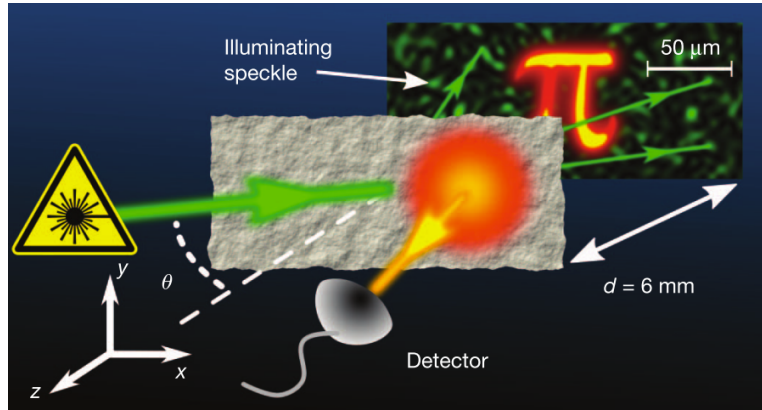


Figure 1.20 – schematic of the apparatus for non-invasive imaging through strongly scattering layers from ref. [BvPB⁺12].

The first image of a complex fluorescent object hidden behind an unknown opaque scattering layer was achieved by Bertolotti *et al.* in 2012 [BvPB⁺12]. This result was possible without any knowledge of the scattering layer, thanks to the "memory effect". The fluorescent object was hidden behind a ground-glass diffuser onto which a laser beam was shone, producing a speckle pattern on the object plane, as shown in figure 1.20. Thanks to the "memory effect" the speckle pattern can be scanned over the sample by incrementally changing the inclination of the laser beam with respect to the diffuser plane. At each angle, the speckle is translated on the sample, by consequence the fluorescence signal emitted from the sample changes. From behind the diffuser, this signal is completely randomized, but the total amount of transmitted fluorescence can be measured and retains the information on the overlap between the object's $O(\mathbf{r})$ and the speckle intensity $S(\mathbf{r})$, where \mathbf{r} is the vector of spatial coordinates.

If the measurements of total fluorescence collected for each tip and tilt angle are assigned to a bi-dimensional matrix, an image can be formed, which corresponds theoretically to the convolution of the speckle pattern with the object:

$$I(\theta) = \int_{-\infty}^{\infty} O(\mathbf{r})S(\mathbf{r} - \boldsymbol{\theta}d)d^2r = [O \otimes S](\boldsymbol{\theta}) \quad (1.3.1)$$

The pixel size of this image depends on the step angle $\boldsymbol{\theta} = (\theta_x, \theta_y)$ used in the scanning process and the object distance d , because the memory effect translates the speckle pattern over a distance $\Delta r \approx \boldsymbol{\theta}d$.

Since the measured image is the result of a convolution between object and speckle pattern, if the latter were known, a simple deconvolution would be sufficient to recover the image. Unfortunately the pattern is not known here, because it is also hidden by the diffuser. Nevertheless, speckles have interesting statistical properties that allow a reconstruction of the object even in this case. In fact, since they are quasi-random structures, their auto-correlation is

almost everywhere small, except in a region around zero. Therefore the autocorrelation of a speckle pattern can be seen as an approximation of a Dirac delta function $[S \star S] \simeq \delta(\mathbf{r})$.

The importance of this feature becomes evident if we write the autocorrelation of the speckle image $I(\theta)$ of equation (1.3.1):

$$[I \star I](\theta) = [O \otimes S] \star [O \otimes S] \quad (1.3.2)$$

$$= [O \star O] \otimes [S \star S] \quad (1.3.3)$$

$$\simeq [O \star O] \otimes \delta(\mathbf{r}) \quad (1.3.4)$$

$$\simeq [O \star O] \quad (1.3.5)$$

The second step makes use of the convolution and correlation theorem ¹³

equation (1.3.5) shows that the autocorrelation of the object O and of the speckle image I are approximately the same. Knowing the autocorrelation of a signal is equivalent to knowing its power spectrum, in fact, thanks to the auto-correlation theorem:

$$|\mathcal{F}[O]|^2 = \mathcal{F}[O \star O] \quad (1.3.6)$$

And by using this in equation (1.3.5) we find

$$|\mathcal{F}[O]|^2 \simeq \mathcal{F}[I \star I] \quad (1.3.7)$$

Hence the speckle image carries the information of the magnitude of the FT of the object O .

At this point a phase retrieval algorithm can be used to recover the missing phase and, consequently, the object itself. [Fie13].

The "memory effect" can not only be used to scan, but also as an important knowledge to recover the information that comes from an incoherent light emitting object hidden behind a diffuser. In fact, light from nearby points on the object is scattered by the diffusive medium

¹³In step 2 in eq. (1.3.5) we have used the convolution and correlation theorems $\mathcal{F}[a \otimes b] = \mathcal{F}[a]\mathcal{F}[b]$, $\mathcal{F}[a \star b] = \mathcal{F}[a]^* \mathcal{F}[b]$ Explicitly:

$$\begin{aligned} [I \star I] &= \mathcal{F}^{-1} \{ \mathcal{F}[I]^* \mathcal{F}[I] \} \\ &= \mathcal{F}^{-1} \{ \mathcal{F}[O]^* \mathcal{F}[S]^* \mathcal{F}[O] \mathcal{F}[S] \} \\ &= \mathcal{F}^{-1} \{ (\mathcal{F}[O]^* \mathcal{F}[O]) (\mathcal{F}[S]^* \mathcal{F}[S]) \} \\ &= \mathcal{F}^{-1} \{ (\mathcal{F}[O \star O]) (\mathcal{F}[S \star S]) \} \\ &= [O \star O] \otimes [S \star S] \end{aligned}$$

to produce highly correlated, but shifted, random speckle patterns [KHFG14]¹⁴. Each point of the object can be thought as a point source that, through the diffuser, generates a speckle pattern. Then, if the distance of any 2 points (i.e. the object size) is in the range of the memory effect, the speckle pattern generated by every point is the same, but shifted. Hence, the scattered image seen after the diffuser is the convolution of the object with the speckle pattern that would be generated by one point source. This means that if the object emits incoherent light, a simple camera acquisition of the light scattered by the diffuser contains enough information to reconstruct the object.

We conclude this section with a note on the "memory effect". This effect applies to thin scattering diffusers at a distance from the target and depends on the fact that, when slightly tilted, the light that enters the diffusers sees approximately the same region of it and is therefore scattered in the same way. This precludes the use of the "memory effect" within thick scattering media, such as fog and biological tissue. But, against all expectations, within thick anisotropically scattering media, strong forward scattering can enhance the memory effect range and thus the possible field-of-view by more than an order of magnitude compared to isotropic scattering. The kind of memory effect that Judkewitz *et al.* [JHV⁺15] describes and that takes place in strongly anisotropic scattering, is not the same as in the case of thin diffusers. In the case of normal "memory effect", a translation is obtained in the far field thanks to a tip-tilt of the input beam, whereas for thick tissue the correlation is shift/shift: shifting the input beam by a small distance over the diffuser displaces the generated speckle pattern without changing it too much, even in depth, at least in the range of one TMFP (cf. sec. 1.2). This remarkable observation has recently been generalized by Osnabrugge *et al.* [OHP⁺17]

This discovery confirms the applicability of "memory effect"-based double-blind speckle imaging to biological tissues, which scatter indeed in a strongly anisotropic way. The only limitation that still remains on the applicability of the "memory effect" lays on its limited extension: in the case of biological tissues the FOV barely spans some microns at a depth of less than one TMFP. Considering that the size of a cell is about 10 μm , such a limited FOV is discouraging, unless the interest is oriented to smaller objects, and becomes even more interesting if the aim is to perform super-resolution.

¹⁴The principle is the same of Labeyrie's *speckle interferometry*, although it involves an additional image recovering step..

1.4 Motivation and outlook of this thesis

In this first chapter we presented the context of super-resolution in optical microscopy, explained the key concepts and illustrated some super-resolution techniques that can achieve a resolution at the scale of the nanometre.

Concerning the application of these techniques, we have seen that in biological samples, where optical super-resolution is the most needed, it is also strongly limited by several factors, among which scattering is probably the most important. Scattering degrades imaging and precludes the possibility of projecting structured light patterns (necessary for super resolution) already at relatively small depths in tissues, where coherent light interferes randomly and give rise to often undesired speckle patterns.

Nevertheless, speckles have been successfully used as an imaging device and it has clearly been shown that it is possible to image through opaque layers thanks to the properties and some peculiar effects that speckle pattern feature, one above all the "memory effect". Even if this effects allows a quite limited FOV, it is still enough from the point of view of super-resolution microscopy.

The idea we want to prove in this work is that super-resolution can indeed be performed with random speckle patterns. According to what has been discussed in this chapter, there are numerous advantages in using this kind of illumination:

- speckle patterns are spontaneously produced by scattering in diffusive media, which, by the way, can introduce higher frequencies than what allowed by the illumination NA[YTW17].
- they are robust to aberrations, in the sense that a scattered speckle patterns remains a speckle pattern[Goo06].
- their power spectrum is flat in average (except at zero frequency), thus allowing efficient probing of the high spatial frequencies of an imaged sample, contrary to regular confocal and epifluorescence microscopy whose optical transfer function vanishes at the spectral domain boundaries.
- Random speckle patterns form a pseudo-orthogonal basis, as explained in section 3.3.1.

Together with this advantages, and even more interestingly, speckle patterns contain dark spots of the same nature than the doughnut shaped STED beam, therefore they are a good illumination scheme to perform super-resolution. This is what will be shown in the next chapter.

Chapter 2

Speckle for super-resolution

Speckle patterns are the result of disordered scattering, but, in spite of the appearance of being completely random, they have some interesting morphological and statistical properties offering high advantages for imaging. In chapter 1 we have seen, indeed, that several imaging methods which use speckles have already been proposed, but none of them aimed to perform super-resolution microscopy by saturation of an optical transition.

The aim of this chapter is to explain why speckle patterns are suited for super-resolution. For that, we will first examine these interesting light structures, from their nature and statistical properties to the optical singularities that they naturally feature.

2.1 Characteristics of speckle patterns

Speckle patterns are disorderly structured interference patterns that appear when coherent light is scattered by a diffuser. This can occur when light bounces on a rough surface or passes through an object which is not optically homogeneous. For example, when a plane wave passes through a ground glass, its wave-front gains a phase shift which depends on the local thickness of the diffuser. Just after the diffuser, the phase difference at two points, for which the distance is larger than the average diffuser's grain size, is statistically decorrelated. The result of this process is that, away from the scattering object, a disordered intensity interference pattern appears, that can be interpreted as the coherent sum of the randomly de-phased waves scattered from each point of the diffuser. Thus a speckle pattern features bright and dark grains, which correspond to constructive and destructive interference of these many uncorrelated waves. The average features of such grains depend solely on the properties of the scattering object and of the imaging system that produces the speckle pattern.

A speckle pattern can be also projected with an optical system such as a lens or an objective positioned after the diffuser. If a coherent polarized beam passes through a thin diffuser and is "focused" with an objective of a given NA, a disk of light containing a speckle pattern appears

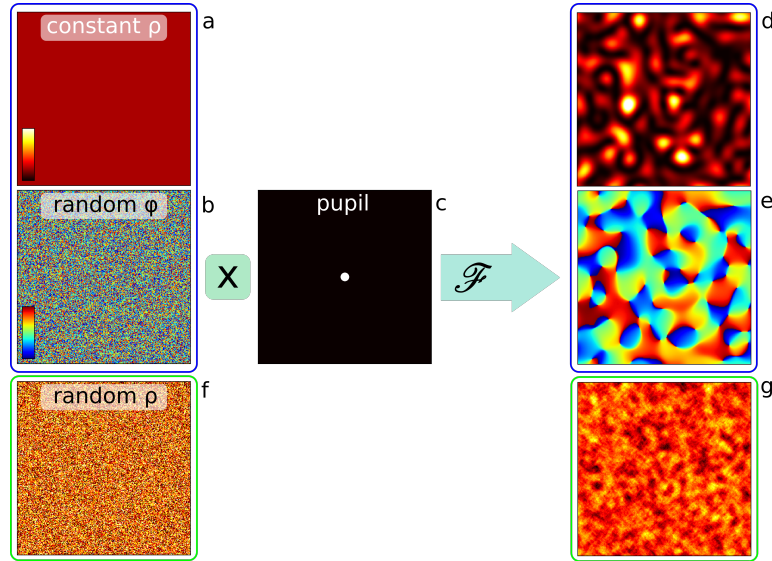


Figure 2.1 – a speckle pattern can be numerically simulated by multiplying a complex image of constant amplitude (a) and randomly distributed phase (b) with a top-up shaped pupil (c) and then calculating the FT of the product (d-e). The pupil operates as a low pass filter in the space of the pattern spatial frequencies, so the average grain size in the pattern is inversely proportional to the pupil diameter. The well contrasted morphology of the speckle pattern is an effect of coherent interference. To compare, we apply the same filter on a real valued random image (f) and show the result (g).

on the focal plane.

Under the hypothesis that the light is polarized and the diffuser grain is much smaller than the resolution of the system on the diffuser plane (or if the diffuser is at infinite), the generation of a speckle pattern can be modelled as a random sum of infinitely many phasors (complex numbers) representing the ensemble of the plane waves (with evenly distributed phases) that interfere in every point of the focal plane. Under this assumption, a speckle is said to be **fully developed** and obeys circular Gaussian statistics [Goo15]. In appendix A we report the formal description of fully developed scalar speckle patterns, here we summarize the most important results and properties.

When a lens can be simply modelled by a Fourier Transform, a polarized speckle field projected by this lens can be thought of as the FT of a field of constant intensity and randomly distributed phase, multiplied by a top-hat shaped pupil, as illustrated in figure 2.1. This makes it quite easy to numerically simulate fully developed speckle patterns. In our work we have taken advantage of this possibility and often used numerical simulations to model our experiments and understand the results.

In the realization of a speckle pattern by an optical system, if the diffuser and the focal plane are Fourier-conjugated, the typical sizes observed on one plane are inversely proportional

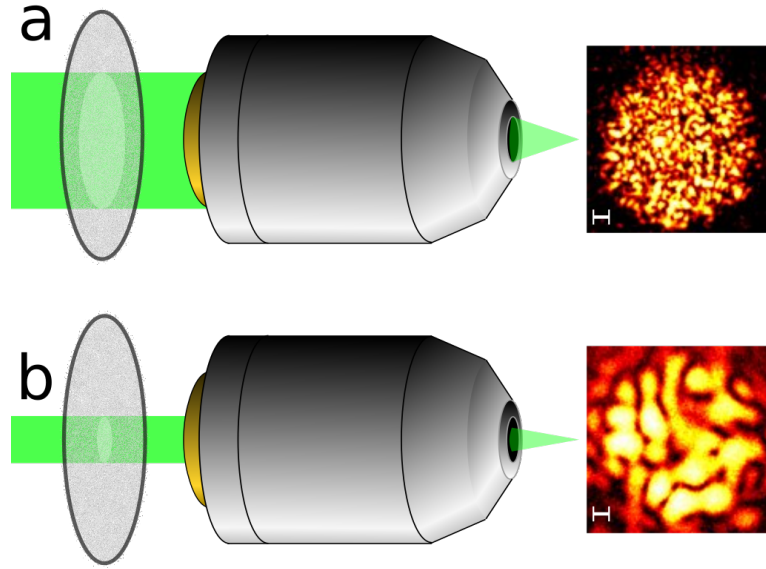


Figure 2.2 – a laser beam passes through a thin diffuser and is focused with an objective. In figure (a) the objective’s pupil is completely filled and the speckle grain average size is limited by the objective resolution, whereas in figure (b) the pupil is under filled, and the average speckle grain size is larger. The image of the speckle patterns are experimental: the wavelength is 532 nm and NA is 1.4 (a) and 0.3 (b). The scalebar is 1 μm .

to those on the other. Indeed, the diameter of the spot in the objective focal plane is inversely proportional to the diffusers grain size. In the same way, the speckle grain average size on the focal plane is inversely proportional to the NA of the objective.

The objective NA poses a limit to the average grain size. In fact, exactly as in the case of a diffraction limited spot, the objective acts as a low-pass filter for the spatial frequencies, therefore the speckle pattern cannot contain frequencies that are higher than the objective resolution. The **average size of a speckle grain** focused with an objective of a given NA is approximately the same size of the objective PSF (for a derivation see A.4):

$$\Delta r \propto \frac{\lambda}{\text{NA}} \quad (2.1.1)$$

$$\Delta z \propto \frac{2n\lambda}{(\text{NA})^2} \quad (2.1.2)$$

but it can be increased by simply under-filling the objective pupil, as it is sketched in figure 2.2.

The **intensity distribution** of a fully developed speckle pattern with mean intensity \bar{I} is exponential:

$$\rho_I(I) = \frac{1}{\bar{I}} \exp \left\{ -\frac{I}{\bar{I}} \right\} \quad (2.1.3)$$

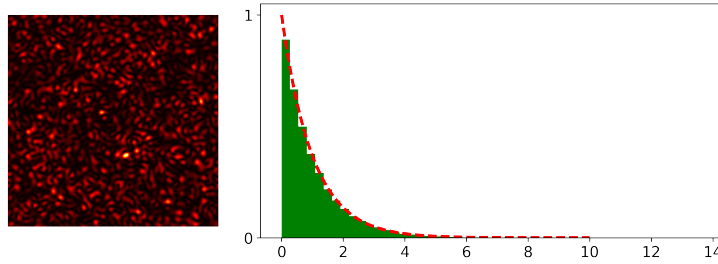


Figure 2.3 – A numerically simulated speckle pattern on the left and its normalized intensity histogram on the right. The red dashed line is an exponential distribution of average 1 (see eq. (2.1.3)).

This distribution is plotted in figure 2.3. Remarkably, small intensities have higher probability to occur and the maximum value is at $I = 0$.

Indeed points of zero intensity are not rare in polarized speckle patterns. In average there are at least as many points of zero intensity as bright spots [Ber78].

The presence of such zeros of intensity is of high importance for this work, because, as it has been said in chapter 1, any illumination pattern, in order to be exploitable for saturation in super-resolution, must be highly contrasted. In other words it must feature tiny zones of very low (ideally zero) intensity, where the selected optical transition is never saturated, whatever the average intensity of the pattern.

2.1.1 Phase singularities in speckle patterns

A point of zero intensity in a speckle pattern is an example of a more general phenomenon which is known under different names: *nodal point*, *phase singularity*, *optical vortex* or *screw dislocation*. Such points are obtained by the interference of at least 3 plane waves, as shown in figure 2.4. The term singularity comes from the fact that, if the complex amplitude of a scalar (e.g. optical) field is represented by a phasor (with modulus ρ and phase χ) as

$$\mathbf{A} = \rho e^{i\chi}$$

in a point where $\mathbf{A} = 0$ the modulus must be zero, but the phase is undefined: it can assume any value from 0 to 2π . Indeed, around such a point, all values of the phase from 0 to 2π occur and, along a path closed around the zero point, there is a net phase difference of an integer multiple of 2π

$$c = \frac{1}{2\pi} \oint d\chi \in [\mathbb{Z} - 0] \quad (2.1.4)$$

The integer c is called **topological charge** of the singularity. It is positive if the phase increases in right-handed sense, negative otherwise. The singularity that spontaneously occur

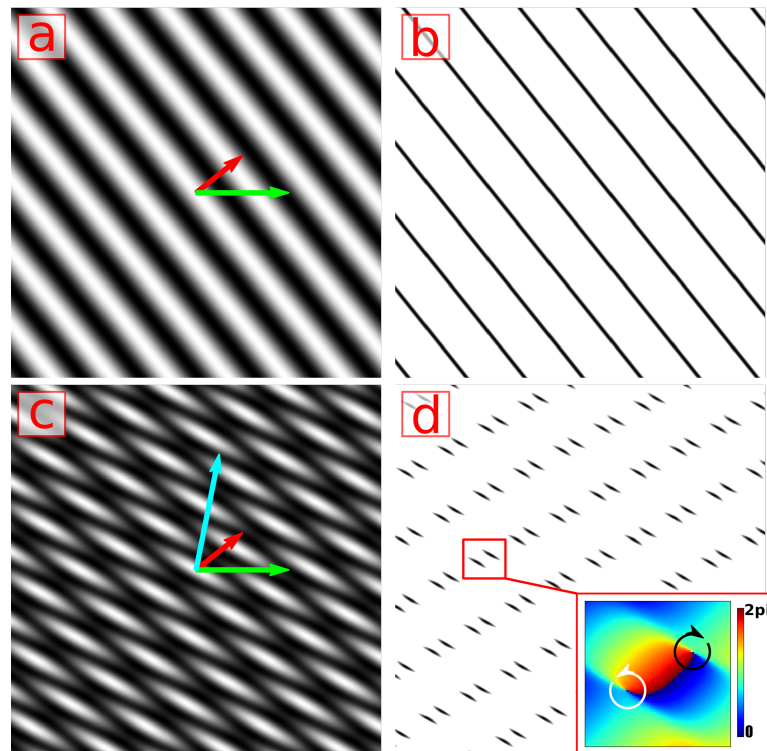


Figure 2.4 – Interference pattern of two (a) and three (c) plane waves. The arrows represent the wave vectors. In images (b) and (d) the black lines and dots represent the zones where the intensity is smaller than 3% of max. Three waves are sufficient to obtain phase singularities. The inset in (d) shows the phase vortices in correspondence of two phase singularities.

in speckle patterns can have a topological charge of +1 or -1. Although singularities of charge c higher than 1 or lower than -1 exist, they are unstable: they split in a number of charge +1 vortices equivalent to their initial charge, as soon as a constant wave is added to them[DOP09]. Therefore such high charge singularities have zero probability to occur in random fields.

This circuitation of the phase is also the reason why these points are also called **optical vortices**: vortices are regions of a fluid where the flow rotates around a central line. The optical current of a polarized scalar field (represented by the Poynting vector) follows the gradient of the phase, hence it rotates around the zero point[Jac01].

$$\mathbf{j} = \rho^2 \nabla \chi \quad (2.1.5)$$

so the optical current has a vortex-like behavior around a phase singularity.

The intensity profile around phase singularities is in general elliptical (see for ex. fig. 2.4) and sectors of equal area sweep out equal intervals of phase, in a Keplerian sense[Den01]. A more rigorous description of the local morphology of the phase singularities is given in appendix A.6.

The condition for an optical singularity to appear is that both the real and imaginary parts of the field must be zero. For a smooth scalar field in a 3-dimensional space, the *loci* of $\mathcal{R} = 0$ and $\mathcal{I} = 0$ are surfaces and their intersection are lines. Along these "nodal" lines (represented in figure A.9) the intensity is zero and the surfaces of constant phase are helicoidal. The trajectory of these nodal has the behavior of random walk[DOP09]. They can be open or appear in couples and collide, forming closed loops.

The density of vortices in a speckle pattern is approximately one per coherence area (see appendix A.4), which means that, in average, there are as many vortices as bright grains in a speckle pattern. Therefore, their number in a finite surface only depends on the grain size, which is inversely proportional to the system's NA. Last, the densities of vortices of charge +1 and -1 is in average the same in a given speckle pattern[DOP09].

Because of the presence of points of zero intensity, speckle patterns are in principle well contrasted, hence exploitable for super-resolution by saturation. Nevertheless, up to now we have considered only scalar fields, whereas the most promising aspects of speckle imaging lie beyond the paraxial approximation, which is not adequate in some conditions: for example, to describe scattering from thick samples or propagation in high NA systems. In this case, the axial component cannot be neglected, especially in the phase singularities. Therefore, its contribution must be considered to study zeros of the vectorial field, in the perspective of performing super-resolution imaging.

Although phase singularities have been already observed and studied in regimes where the scalar approximation could be considered valid, [ZG07, LDCP05] a direct observation of the axial component in the phase singularities of a speckle pattern had never been carried out. Nevertheless the fact that a speckle pattern contains localized points of low intensity is crucial in order to use it as an illumination pattern for super-resolution, because only in this case an optical transition can be confined in sub diffraction volumes. These are the motivations that inspired the following work and corresponding results, as discussed in the next section.

2.2 Speckle/STED analogy

In order to understand how the axial component in the phase singularities of a speckle pattern can be controlled, we propose here a parallel with the doughnut beam used in STED microscopy. As we have seen in chapter 1, the doughnut shaped STED beam is used to confine fluorescence emission in a sub diffraction volume in the sample. This is possible because the beam features a zero of intensity in the centre of the focal plane. Therefore, even at very high average intensities of the beam, a small portion of fluorophores around the centre will not experience an intensity high enough to saturate the stimulated fluorescence emission: the presence of the intensity zero preserves the fluorescence signal.

The point of zero intensity in the focused STED beam is a phase singularity. In fact, the STED beam is a natural laser mode of the Laguerre-Gauss (LG) family¹. This beam is simply generated with a spiral phase mask that applies to the beam a phase from 0 to 2π , proportional to the angle in the transverse plane (fig. 2.5).

In the scalar approximation, the field of the STED beam on the focal plane has a doughnut shaped intensity with a perfect zero at its centre, which happens to be a phase singularity of charge one (the phase spans the interval $0-2\pi$ around the zero point) (fig. 2.6). The sign of the charge depends on the handedness of the spiral phase mask that has generated the beam, which corresponds to the rotation handedness of the phase around the propagation axis.

If the scalar approximation can not be considered valid, as it is the case of the STED beam focused with a high NA objective, the axial component of the field has to be taken into account and possibly annihilated in correspondence of the phase singularity, to maintain a low intensity.

In the case of the STED beam, the axial component can be controlled through polarization[GHV⁺12]. In fact, if the STED beam is circularly polarized, thanks to the central symmetry of the beam, the axial component in the focal point can be totally cancelled. More precisely, if the circular

¹the LG mode set is a complete orthogonal basis where arbitrary light beams can be represented, just like the Hermite-Gaussian or TEM basis.

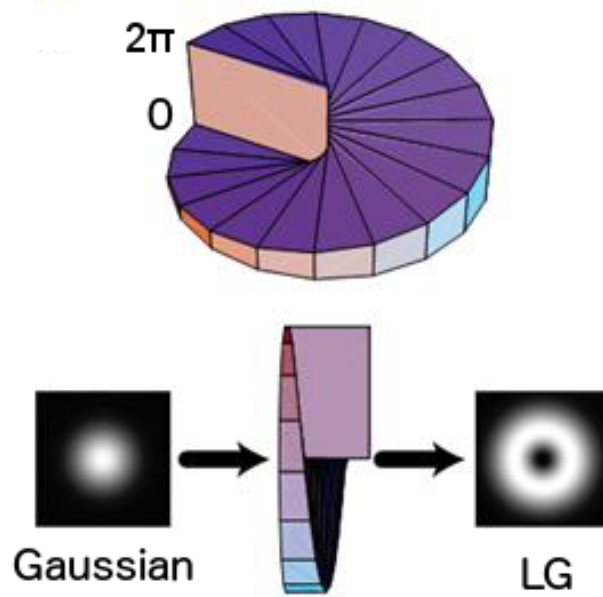


Figure 2.5 – Representation of the spiral phase mask used to produce the STED beam.

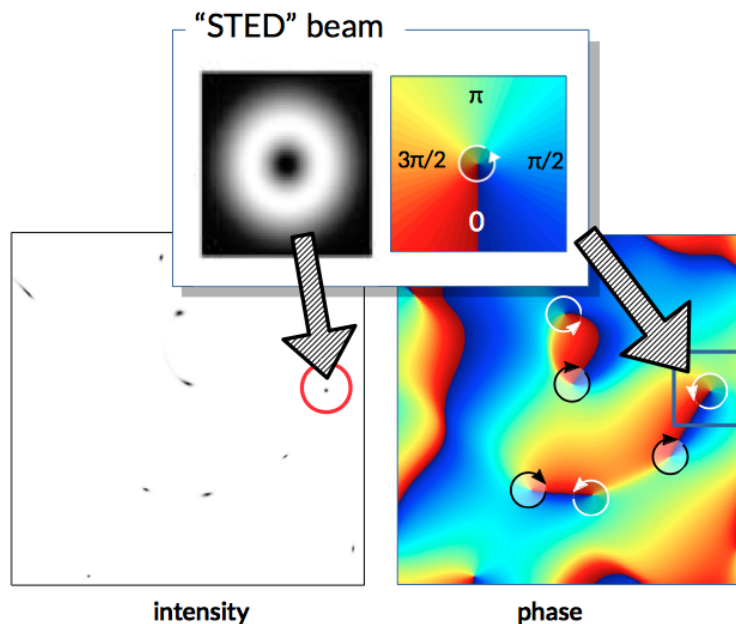


Figure 2.6 – In the first row: the amplitude (left) and phase (right) of the STED beam in the focal plane. The second row shows the amplitude of numerically simulated saturated speckle pattern with its dark spots corresponding to the phase singularities (left) and the phase (right). In correspondence to the phase singularity there is always a clock-wise or counter-clock-wise spiral, highlighted by the black and white arrows.

polarization handedness is chosen with the same handedness of the particular LG mode (i.e. the handedness of the spiral phase mask), the axial component of the field is completely cancelled and the phase singularity in the doughnut centre is a vectorial zero of the field. Conversely, if the wrong polarization handedness is applied, the axial component is maximized and the field amplitude in the doughnut centre is not zero (see fig. 2.7 and 2.8). In the former case, the beam can still be used for saturation and super-resolution, whereas in the latter this is not possible.

Speckle patterns, as we have seen, also contain charge +1 and -1 phase singularities (fig. 2.6), which are randomly distributed in the pattern, so we might expect that circular polarization could be used also with this illumination scheme to control the field's axial component and ensure the quality of the intensity zeros. But, the intensity profile and phase around the phase singularities in a speckle field are not radially symmetric in general (contrarily to the case of the STED beam). Therefore the ability of circular polarization to preserve the contrast of a speckle pattern must be proven (see appendix A.6 for a more rigorous explication).

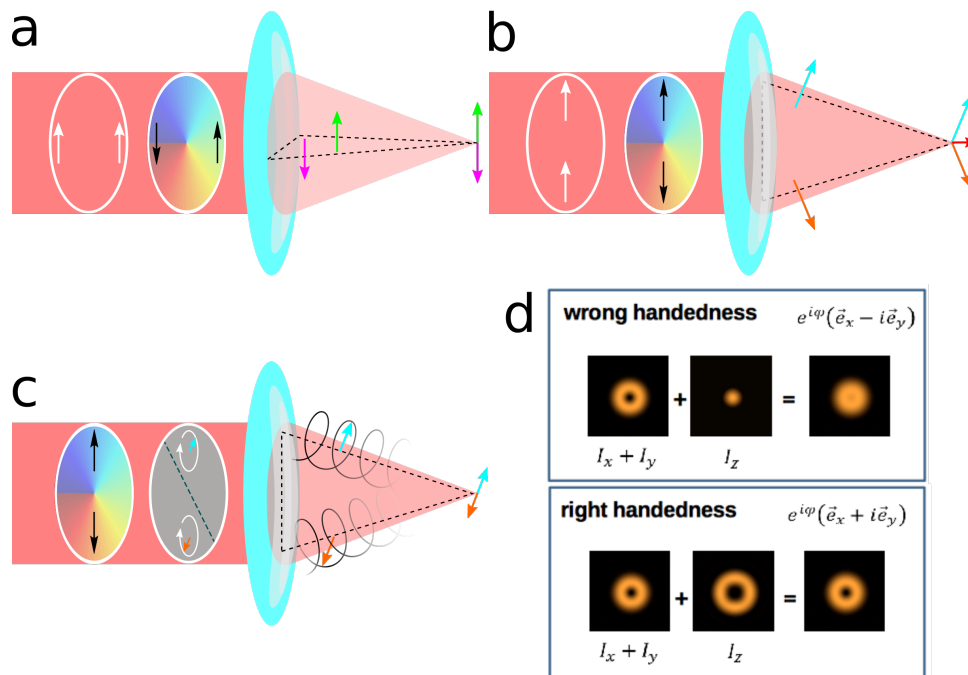


Figure 2.7 – The axial component at focus of the STED beam: in images (a),(b),(c) a vertically linearly polarized beam passes through a spiral phase mask and is focused by a high NA objective. In image (a) and (b), two couples of opposed optical rays are followed. Depending on the choice of the position of the rays, an axial component appears at focus. In image (c) a quarter wave plate is used to switch the polarization to circular. In this case, the axial component of any couple of opposed rays annihilates. The handedness of the circular polarization must correspond to the spiral phase handedness in order to annihilate the axial component: the wrong handedness maximises it (d).

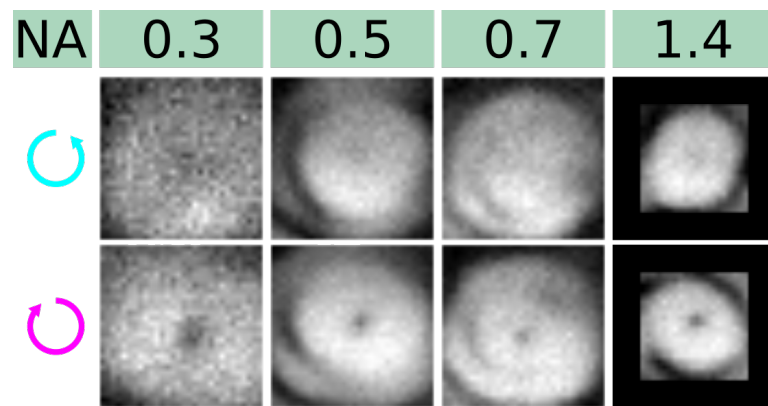


Figure 2.8 – Experimental images of a donut beam generated by a SLM and obtained by scanning a fluorescent nano-bead under saturated excitation conditions. The beam was generated with different NA, as indicated by the columns label. In the first row the polarization is circular right handed, in the second it is left handed. Left handed polarization corresponds to the handedness of the spiral phase mask, therefore it annihilates the axial component in the doughnut centre. Conversely, for right handed polarization, the axial component is maximised and the black spots at the doughnut centre disappears.

2.3 Imaging the phase singularities in a speckle pattern

Speckle phase singularities can already be observed with a simple camera (and have been [LDCP05]), but cameras are not sensitive to the axial component of the field. On the other hand, the axial component in a high NA speckle pattern is what we are interested to observe. The applicability of speckle illumination in super-resolution depends on its contrast, the latter, in turn, depends on the the quality of the dark spots of the pattern.

In order to appreciate the effect of the axial component of the field in a speckle pattern and its effect on the pattern contrast, it would be ideal to observe the saturation of an optical transition on real fluorophores. Unfortunately, the very high intensity needed to saturate fluorescence excitation (see appendix C), as in Saturated Structured Illumination Microscopy, requires a dedicated laser source, which was not yet available in our laboratory.

Photo-bleaching (PB) instead, is a transition that does not require high intensities to take place. Moreover, the probability of bleaching a fluorophore increases with the time. Since this transition is not associated to the emission of a signal, as fluorescence excitation (and successive de-excitation) is, the effect of PB can only be measured indirectly as the absence of fluorescence from the sample.

As a consequence of these considerations, we have designed an experiment to study the contrast of saturated speckle pattern by means of PB. The experiment consists in bleaching an uniformly fluorescent thin sample with a speckle pattern and look for structures of residual fluorescence. If the intensity in the phase singularities of the speckle pattern is dark enough, some fluorophores should be preserved from PB, even after long exposure times. Therefore, by imaging the residual fluorescence, we can image the speckles phase singularities.

In the following sections, we present the experiment and describe a model for the dynamic of the PB process. Then, we propose a theoretical model for the average size of the dark spots in a speckle pattern, based only on the ensemble statistics of fully developed speckle patterns. This model is in agreement with the experimental data and confirms the validity of the previously mentioned analogy between the STED doughnut and the phase singularities in speckle patterns. Finally we briefly discuss the effect of the axial component.

This short introduction is the essential background behind the paper attached at the end of this chapter.

2.3.1 The bleaching/imaging setup

The setup, sketched in figure 2.9, can be divided in two main parts corresponding to bleaching and imaging. The imaging part is a custom built, conventional STED microscope. We used

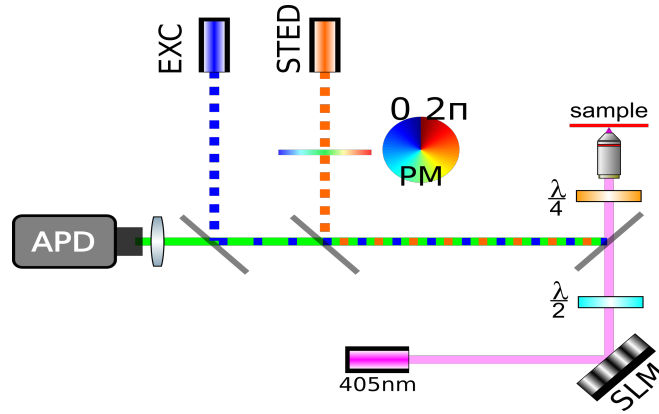


Figure 2.9 – The setup used to study the speckle phase singularities. It consists of a bleaching path, where an SLM is used to produce the bleaching speckle pattern, and a custom build STED microscope, used to image the residual fluorescence.

a STED instead of a simple confocal because we expected a confinement of fluorescence in volumes of sub-diffraction size.

The bleaching part consists of a Spatial Light Modulator (SLM) that we use as a random diffuser, with the advantage of being able to change the speckle spot size, thereby tuning the average intensity of the pattern. The SLM is addressed with a phase pattern which should generate a homogeneous spot of the desired size in the sample plane. The phase pattern is calculated with one iteration of the Gerchberg–Saxton algorithm [GS72]. Since the SLM is just a phase object and does not modulate the field intensity, a fully developed speckle pattern spontaneously appears in the spot. In practice, with an SLM, it is extremely easy to change the diffuser coarseness (grain size).

A quarter wave plate is also used here, to circularly polarize the beam in order to annihilate the axial component in correspondence to positive or negative phase singularities in the speckle pattern.

2.3.2 Photo-bleaching model

When PB occurs, a fluorophore (FP) undergoes structural changes or chemically interacts with its surroundings in an irreversible way that makes it lose permanently its ability to emit fluorescence, therefore the molecule becomes dark (see fig. 2.10). Typically, a FP undergoes several ($\simeq 10^5$) fluorescence cycles before being damaged by PB [PBM99].

When an ensemble of many FP is illuminated with a constant intensity I_e , the PB dynamics is governed by an exponential decay. Under non-saturated excitation (experimental conditions), the number of FP N_f that are still fluorescent after a time t decreases as

$$N_f(t) = N_f(0)e^{-k_b \frac{I_e}{I_s} t} \quad (2.3.1)$$

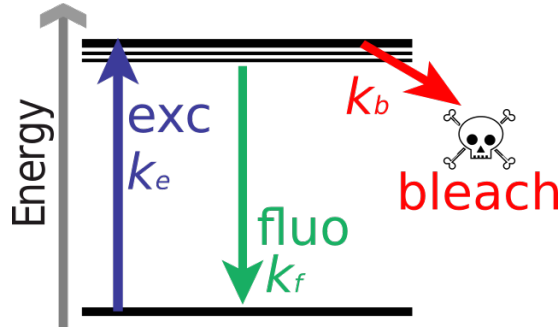


Figure 2.10 – The Jablonsky diagram of the bleaching process in a simplified 2-levels fluorescent system. An excited fluorophore can fall back to the ground state and be available to be re-excited, or fall into the bleaching state, thereby losing its ability to emit fluorescence. This scheme gives just a representation. In reality the bleaching dynamics can be much more complex[ZKKO04].

where k_b is the bleaching rate and I_s is the excitation saturation intensity. The residual fluorescence I_f is proportional to N_f therefore,

$$I_f(t) = I_{f0} e^{-k_b \frac{I_e}{I_s} t} \quad (2.3.2)$$

where t is the duration of the PB exposure and $I_{f0} = I_f(0)$ is the fluorescence that one would measure without the PB process. Since k_b is a constant, the speed at which bleaching occurs is determined by the ratio I_e/I_s : the higher the excitation intensity, the faster the PB. Therefore, if an illumination pattern that shows intensities fluctuations is shone on a fluorescent sample, at a given time, the parts of the sample which were illuminated by a higher intensity will be more bleached than others. After a certain time, all the sample will eventually be bleached, except the parts of it that remained in the dark, in correspondence of intensity zeros, if there were any in the illumination pattern.

Therefore, in order to characterize the intensity minima of a high NA speckle pattern, we illuminated a homogeneous fluorescent thin sample with such a pattern and looked at the remaining fluorescence after a certain time t .

Statistics of the remaining fluorescence

Since the statistics of the intensity distribution in a speckle pattern is known (see eq. (2.1.3)), by making use of eq. (2.3.2) we can write the PDF of the residual fluorescence in the sample after PB. Eq. (2.3.2) is monotonic, therefore we can write $\rho_x(x) = \rho_y(y) \left| \frac{dy}{dx} \right|$. In order to do

so, we first invert the transformation.

$$I_e(I_f) = -\frac{I_s}{qt} \ln \left(\frac{I_f}{I_{f0}} \right) = \ln \left(\frac{I_f}{I_{f0}} \right)^{-\frac{I_s}{qt}} \quad (2.3.3)$$

$$\left| \frac{dI_e}{dI_f} \right| = \frac{I_s}{qt} \frac{1}{I_f} \quad (2.3.4)$$

and we can write the new PDF of I_f as

$$\rho_f(I_f) = \frac{1}{\bar{I}} e^{-\frac{I_f(I_e)}{\bar{I}}} \frac{dI_e}{dI_f} \quad (2.3.5)$$

$$= \frac{\frac{I_s}{qt\bar{I}} \left(\frac{I_f}{I_{f0}} \right)^{\frac{I_s}{qt\bar{I}}}}{I_f} \quad (2.3.6)$$

If we set $I_{f0} = 1$ we get a PDF for the normalized residual fluorescence:

$$\rho_f(I_f) = \frac{\frac{I_s}{qt\bar{I}} (I_f)^{\frac{I_s}{qt\bar{I}}}}{I_f} \quad (2.3.7)$$

$$\rho_f(I_f) = \frac{I_f^{\frac{1}{r}-1}}{r} \quad (2.3.8)$$

by defining the *mean bleaching rate* $r = qt \frac{\bar{I}}{I_s}$.

As expected, the probability of having a certain value of residual fluorescence decreases as time t and the average speckle intensity \bar{I} increase. Therefore, even at a relatively low intensity I_e , long exposition times can annihilate the fluorescence in the sample.

Given that k_b and I_s are characteristic parameters of the fluorophore, the experimental variables that influence the PB dynamics are the exposure time t and the average intensity of the speckle pattern \bar{I} , or more precisely, the fluence $F = \bar{I}t$. Remarkably, when $F = \bar{I}t = I_s/k_b$, the average saturation rate is $r = 1$ and the PDF $\rho_f(I_f)$ becomes constant: all intensities have the same probabilities to occur. This model allows to estimate the saturation level of the photobleaching transition by simply measuring the intensity distribution of a bleached sample (i.e. the intensity histogram of its image) and at the same time, to estimate the saturation intensity of absorption I_s .

A statistical model for the fluorescence confinement

Given a certain average intensity $\bar{I} \neq 0$, the probability of bleaching fluorophores is non-zero. Therefore, if the exposure time is long enough, all fluorophores can be photo-bleached. If we excite the homogeneous sample with a speckle pattern, different parts of it experience different intensities. Since the bleaching "speed" is proportional to the fluence F , at a given time and

intensity, some parts of the sample could be completely bleached and other still fluorescent. As time (or intensity) increases, the non-bleached portions of the sample become smaller and smaller.

Recalling the fact that speckles feature phase singularities and that these object have zero intensity, one expects that, in their location, fluorescence should be preserved from PB. Around the singularities the intensity increases continuously, so that the residual fluorescence can be confined around them in volumes, whose size only depends on F .

The average size of the volumes of residual fluorescence can be estimated considering the speckle statistics: instead of considering the fluence F , let us fix the exposure time to a certain value t_0 , for which all FP that where illuminated by a threshold intensity I_t are bleached so that their fluorescence signal is undistinguishable from noise. Conversely, some residual fluorescence is maintained where the intensity is smaller than I_t . Since we know the intensity PDF of the speckle pattern, we can write the probability of obtaining an intensity smaller than I_t (see A.2):

$$P(I_e \leq I_t) = 1 - \int_{I_t}^{\infty} \rho_I(I_e) dI_e \quad (2.3.9)$$

$$= 1 - \exp\left(-\frac{I_t}{\bar{I}}\right) \quad (2.3.10)$$

Given a certain area of the sample S illuminated by the speckle pattern, the portion which is still fluorescent is

$$S_f = S \left[1 - \exp\left(-\frac{I_t}{\bar{I}}\right) \right] \quad (2.3.11)$$

And since we know that in a speckle pattern there is, in average, a phase singularity per grain and that the grain size is approximately $d = \lambda/2NA$, the number of singularities in S is typically

$$n = S/d^2 = S \left(\frac{2NA}{\lambda} \right)^2 \quad (2.3.12)$$

Therefore, if we divide the surface of residual fluorescence (2.3.11) by the number of singularities that are there², we can estimate the average area of residual fluorescence per singularity:

$$A_f = \frac{S_f}{n} = \left(\frac{\lambda}{2NA} \right)^2 \left[1 - \exp\left(-\frac{I_t}{\bar{I}}\right) \right] \quad (2.3.13)$$

As an estimation of the linear dimension of this residual fluorescence area we take the square

²assuming that vortices are statistically far enough from one-another to allow neglecting overlaps, which means for high enough saturation levels

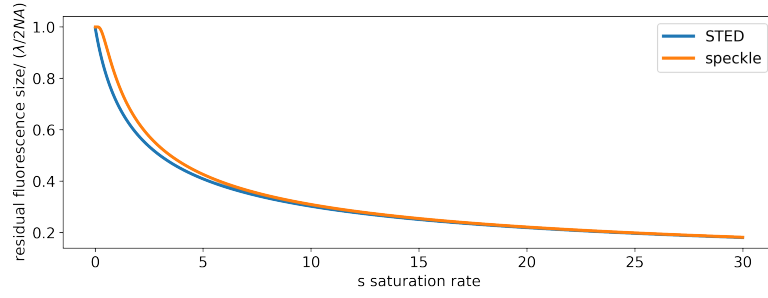


Figure 2.11 – Comparison of the well known model for the resolution of STED microscopy and the average size of the residual fluorescence with saturated speckle illumination proposed here (eq. (2.3.14)).

root:

$$d_f = \left(\frac{\lambda}{2\text{NA}} \right) \sqrt{1 - \exp\left(-\frac{I_t}{\bar{I}}\right)} \simeq \left(\frac{\lambda}{2\text{NA}} \right) \frac{1}{\sqrt{1 + \frac{\bar{I}}{I_t}}} \quad (2.3.14)$$

the last two members are asymptotically convergent³ when $I_t \ll \bar{I}$, as it is shown in figure 2.11. In the RHS of equation (2.3.14), the +1 in the denominator is there to regularize the function so that we can recover the value $d_f = \frac{\lambda}{2\text{NA}}$ when \bar{I} tends towards zero.

We can choose t_0 so that $I_t = I_s$, with I_s the saturation intensity of the fluorescence excitation. In this case we find

$$d_f \simeq \left(\frac{\lambda}{2\text{NA}} \right) \frac{1}{\sqrt{1 + s}} \quad (2.3.15)$$

which is the well known dimension of the residual fluorescence in STED microscopy as a function of the saturation rate $s = \bar{I}/I_s$.

The axial component of the field

The previous result was obtained for a scalar field. We have pointed out that in the case where this approximation is not valid, especially with high NA and under saturated conditions, the axial component of the field becomes important and it has to be taken into account. In this case, circular polarization of handedness corresponding to the charge of the phase singularity has to be used in order to obtain a vectorial zero at focus, hence zero intensity.

In speckle patterns, the dark spots around the phase singularities are similar to the STED one. They are not radially symmetrical, as it is the case for a focused LG beam, neither in amplitude nor in phase (see appendix A.6). They can be considered so, at least in a first

³we study the limit of the ratio of the functions $f(x) = \sqrt{1 - e^{-\frac{1}{x}}}$ and $g(x) = 1/\sqrt{1+x}$ when $x \rightarrow \infty$.

$$\lim_{x \rightarrow \infty} \frac{\sqrt{1 - e^{-\frac{1}{x}}}}{\left(\sqrt{1+x}\right)^{-1}} = \lim_{x \rightarrow 0} \sqrt{\left(\frac{1 - e^{-x}}{x}\right)} (1+x) = 1$$

and in the RHS we can use the known result $\lim_{x \rightarrow 0} \frac{(e^{ax}-1)}{bx} = \frac{a}{b}$.

approximation, in the proximity of the singularity.

Therefore, by using circular polarization in a high NA speckle pattern for the photobleaching experiment, fluorescence should be confined as described in eq. (2.3.15).

Since in a speckle pattern we can find singularities of charge +1 and -1, and since the circular polarization has a specific handedness, the axial component can only be minimized for one class of singularities, whereas it is maximized for the other. This means that the FP that are not bleached lie close to a certain family of phase singularities in a speckle pattern, determined by the handedness of the polarization.

Therefore, by bleaching and imaging two homogeneous samples with the same speckle pattern but different polarization handedness, we can put in evidence the different locations of the phase singularities of charge +1 and -1.

Superresolution Imaging of Optical Vortices in a Speckle Pattern

Marco Pascucci,¹ Gilles Tessier,² Valentina Emiliani,¹ and Marc Guillon^{1,*}

¹*Wavefront Engineering Microscopy Group, Neurophotonics Laboratory, CNRS UMR 8250, Paris Descartes University, Sorbonne Paris Cité, Paris 75006, France*

²*Holographic Microscopy Group, Neurophotonics Laboratory, CNRS UMR 8250, Paris Descartes University, Sorbonne Paris Cité, Paris 75006, France*

(Received 17 September 2015; published 4 March 2016)

We characterize, experimentally, the intensity minima of a polarized high numerical aperture optical speckle pattern and the topological charges of the associated optical vortices. The negative of a speckle pattern is imprinted in a uniform fluorescent sample by photobleaching. The remaining fluorescence is imaged with superresolution stimulated emission depletion microscopy, which reveals subdiffraction fluorescence confinement at the center of optical vortices. The intensity statistics of saturated negative speckle patterns are predicted and measured. The charge of optical vortices is determined by controlling the handedness of circular polarization, and the creation or annihilation of a vortex pair along propagation is shown.

DOI: 10.1103/PhysRevLett.116.093904

Propagation of coherent waves in random scattering media is associated with the generation of speckle patterns. For scalar wave fields; these speckle patterns contain hot spots but, also, true zeros of the field where the phase is singular [1]. These phase singularities—or phase dislocations—exhibit spiral structures with topological charges $+1$ and -1 [2]. The associated zeros of intensity surrounded by light are called optical vortices because of the circular optical current circulating around their dark center [3]. The vortex centers draw lines in space which may loop and knot [2,4] and which can be seen as the wire frame or the “skeleton” onto which the field is built [5]. The information about the circulation handedness of the optical current around these lines lies in the phase of the field.

In any speckle pattern, the density of nodal points is the same as the density of hot spots [6,7]. However, the separation distance between phase singularities can be arbitrarily small, especially when two vortices of opposite charges approach and annihilate, or nucleate and split apart [8]. In addition, the three vector components of an optical field may hang on different nodal skeletons, making the characterization of zeros complicated. For these two reasons, former experimental characterizations of phase singularities in vectorial electromagnetic waves were performed with polarized beams of low numerical aperture (NA) [7,9], or considering a single vector component of the field [10–12] in order to remain within the validity of the scalar approximation.

However, the most promising applications of complex vector fields involve high NA beams and lie beyond the scalar approximation. For instance, phase dislocations are typically used in superresolution microscopy in order to create saturating intensity patterns with perfect zeros [13–16]. Specifically, in stimulated emission depletion

(STED) microscopy [13,17], an optical vortex is commonly used, in combination with a circular polarization, to cancel the axial component of the field at the vortex center [18,19]. In high NA optical speckle fields, the joint characterization of optical vortices and intensity minima remains unexplored, notably due to the subdiffraction spatial scales involved.

In this Letter, we report on the characterization of intensity minima and optical vortices in polarized high NA random speckle patterns using superresolution STED microscopy. To do so, the negative of the speckle pattern is first recorded by photobleaching a uniformly fluorescent sample. Saturated bleaching leaves fluorescent spots at intensity minima, whose size and spacing may decrease below the diffraction limit, thus, requiring superresolution microscopy. First, we experimentally validate an analytical model which quantifies the intensity statistics of the negative. Then, after characterizing the subdiffraction confinement of fluorescence at a vortex of a speckle pattern, we demonstrate that the topological charge of the optical vortices associated with intensity minima can be revealed, experimentally, by controlling the polarization of the random beam. This identification allows visualizing the creation or annihilation of a vortex pair of opposite charges. Finally, we quantify, analytically, the amplitude of the axial component of a circularly polarized random wave field with Gaussian statistics.

The negative of a speckle pattern was first recorded by photobleaching a uniformly fluorescent layer of poly-D-lysine (Sigma-Aldrich) deposited on a coverslip and covalently labeled with the organic dye ATTO 532 (ATTO-TEC) functionalized with an N-Hydroxysuccinimide (NHS) ester group. Photobleaching was performed at 403 nm using a spatial light modulator (SLM) to generate speckle patterns

Chapter 3

Imaging with Saturated Speckle Patterns

In the previous parts of this work, we have seen that speckles are highly contrasted patterns, therefore suited to perform super-resolution (SR) microscopy by saturation of an optical transition. The aim of this chapter is to apply this knowledge and show that it is indeed possible to enhance the optical resolution of a rather simple microscope by making use of this disorderly structured illumination.

We present a new SR technique which could be classified at half-way between STED and SSpIM (see chap. 1). Similarly to this two techniques, we use a patterned illumination, but our patterns are randomly generated. Like in STED, we use a scanning microscope. Differently from STED, the transition that we saturate is fluorescence excitation (like in SSpIM).

name	pattern	transition	detection
STED	doughnut	stim. emission	APD
SSpIM	speckle	excitation	PMT
SSIM	fringes	excitation	camera

The setup that we have developed to perform saturated-speckle illumination microscopy (SSpIM) produces images by scanning a fluorescent sample with a speckle pattern and measuring the total fluorescence coming from the sample at each scanning position.

Super resolution is obtained through saturation of the fluorescence excitation of the sample's Fluorophores (FP) and the object image is reconstructed by means of deconvolution, or phase retrieval algorithms in some simple cases. To characterize the performances of our system, we imaged fluorescent nano-beads and fluorescent-labelled actin filaments. In both cases, the results clearly show a neat improvement in resolution, beyond the classical limit of optical microscopy. A major advantage of our microscope is to be easier to build and align than other SR setups. By adding the appropriate laser source and a simple holographic diffuser, SRIM can immediately be performed on any scanning microscope and, thanks to the fact that we use random illumination, it is not affected by any aberrations caused by the imaging system.

The following sections will present the methods and results concerning the development of SRIM. We will first introduce the optical system, then explain the principle of SSpIM and illustrate our main results. Successively, we will discuss the limits of this technique. In the final section, we suggest a way to take advantage of (saturated) speckle patterns to reconstruct 3D images by simple 2D scanning data.

3.1 The saturated speckle scanning microscope

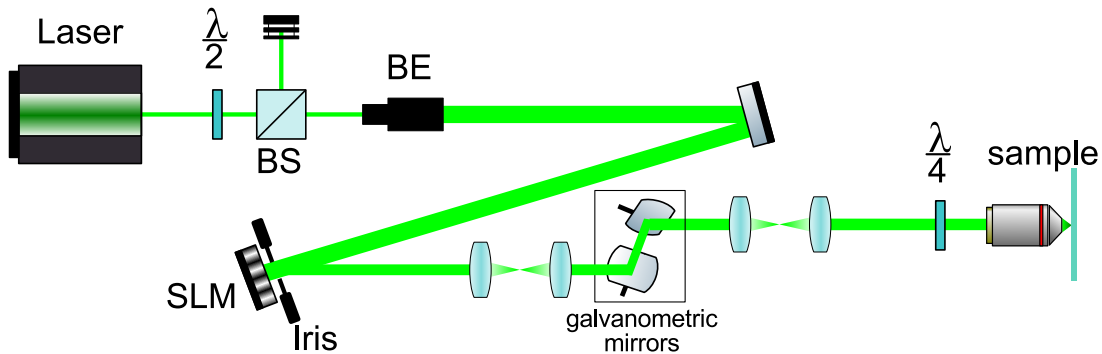


Figure 3.1 – Complete scheme of the speckle scanning microscope. The laser power is modulated using a half-wave plate ($\lambda/2$) and a polarizing beam splitter (BS). The laser beam then passes through a beam-expander (BE) before illuminating the spatial light modulator (SLM) which generates the speckle. The SLM is conjugated to a pair of galvanometric mirrors and to the back focal plane of the microscope objective. A quarter wave-plate ($\lambda/4$) circularly polarizes the impinging beam in order to achieve isotropic transverse super-resolution.

Figure 3.1 shows a scheme of the scanning microscope that we have built to perform saturated speckle imaging.

The laser source is a 532 nm pulsed diode-pumped solid state microchip laser ¹ that outputs high energy pulses ($3.9 \mu\text{J}$) at a frequency of 4 kHz. The pulses have a width shorter than 0.5 ns, which is smaller than the fluorescence lifetime of a typical FP (~ 5 ns).

The excitation probability of the dye typically depends on several parameters such as the fluorescence lifetime of the dye τ_f , its absorption cross-section σ , and the laser-pulse temporal intensity profile (width τ_p , amplitude I_p and shape). Here, we used a sub-nanosecond pulsed laser ($\tau_p \sim 500$ ps), shorter than the fluorescence life-time of the dye to efficiently saturate the optical transition with a minimum amount of average power, and long enough for keeping a low multi-photon absorption probability. The repetition rate of 4 kHz is low enough to ensure

¹Teem Phononics, Meylan, France, STG-03E-120.

efficient dark-state relaxation between excitation pulses. It also minimizes photo-bleaching *via* inter-system crossing [DEH07].

The pulse energy is high enough to saturate the fluorescence excitation of the sample FPs. The peak power of the laser pulses is at least 6 kW. If we deliver such power on a disk of diameter 10 μm onto the fluorescent sample, the intensity is

$$I = \frac{6 \text{ kW}}{\pi 100 \mu\text{m}^2} = 6 \text{ MW/cm}^2 \quad (3.1.1)$$

which is 10 times above the typical value of the excitation saturation intensity (see appendix C). Therefore, each laser pulse carries enough energy to saturate the sample fluorescence excitation on an area of several square microns.

Unfortunately, since the pulse duration is very short, the sample's FP are excited only once per pulse, which makes the fluorescence signal per pulse relatively low. In the saturated regime, the weakness of the signal per pulse is compensated by the fact that all sample's FP are excited and emit fluorescence photons. But if we want to use the same source for non-saturated images, in which case only a small fraction of the FP is excited by a single pulse, the fluorescence signal is so low that it requires averaging over tens of pulses to overcome photon noise. Since, when scanning, we acquire at a maximum frequency of 4 kHz (the laser pulse rate), it means that several minutes are necessary to acquire an image of a 10 $\mu\text{m} \times 10 \mu\text{m}$ area. Although we have been able to take non-saturated images in pulsed mode, such long acquisition times, besides being tedious, also introduce errors due to sample drift, and better images were obtained with a CW laser.

Preferentially, thanks to a flipping mirror, the laser source could then be switched to a low power CW laser diode, which we normally use when we do not want to saturate the excitation, for example to compare the imaging resolution in saturated and non-saturated regimes. Even though the CW laser is way weaker ($\sim 4 \text{ mW}$) than the pulsed one, it excites the sample continuously and FP emits fluorescence all over the illumination time. Therefore, over one integration time of our detector ($\sim 15 \mu\text{s}$) many photons are detected, yielding a good signal to noise ratio.

The number of fluorescent photons detected in the two modes (CW and pulsed) at equal illumination intensity can be written as

$$F_{\text{CW}} = \frac{Nq\phi\Omega}{\tau_f} \Delta t \quad (3.1.2)$$

$$F_{\text{P}} = \frac{Nq\phi\Omega}{\tau_f} t_p \nu \Delta t \quad (3.1.3)$$

where N is the number of the FP in the illuminated area, q is the average excitation of the

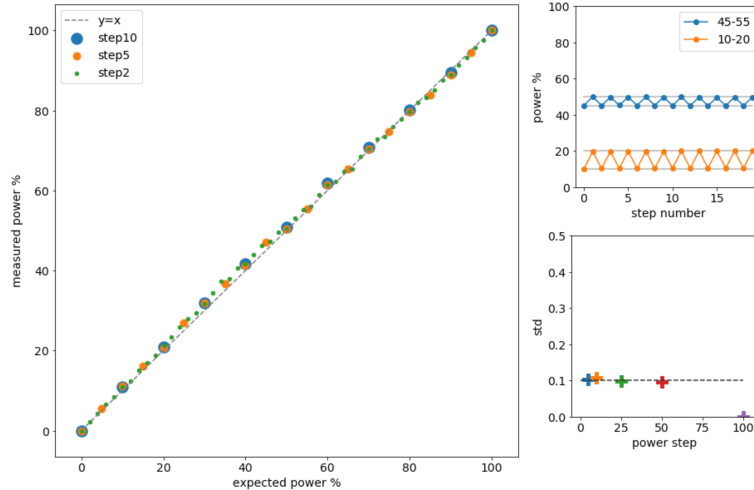


Figure 3.2 – Results of the tests of the power adjustment system. On the left: measured vs expected values for consecutive increasing powers with steps 2%, 5% and 10% of the full range: the mean error is 1.3%. Top-right: repeatedly switching between two fixed power values shows a good reproducibility. The average error on the step width is 0.1% of the full range. We have done this for steps of different width, the error is shown in the bottom-right plot.

sample (fraction of excited FP per time unit), ϕ is the fluorescence quantum yield, Ω (collection efficiency) accounts for the detection angle and the transmission coefficient of the system, τ_f is the fluorescence mean lifetime and, Δt is the detector's integration time, ν is the pulse repetition rate and t_p is the pulse duration. The detection ratio between the two mode is then

$$\frac{F_{CW}}{F_P} = \frac{1}{\nu t_p} \sim 10^6 \quad (3.1.4)$$

which clearly shows the difficulty of obtaining a non-saturated image with our pulsed laser and therefore the need of a careful calibration of the excitation power.

Power adjustment is achieved here with a half-wave plate and a polarizing cube. In addition, as the pulsed laser is very intense, we have often used a set of optical densities, dimming the laser up to 10^{-4} times.

Since the half-wave plate rotation is controlled with a custom 3D printed actuator, driven by an Arduino UNO board, we have tested the reliability of this system. The sensitivity of this control system is high enough for our experiments with an average error of $\sim 1.3\%$ of the full power range. We have also measured the reliability when switching repeatedly between two power values. From jumps ranging between 10% and 5 % of the full power range, the standard deviation is constant, around 0.1%. For smaller steps, it increases slightly, due to mechanical friction in the rotating parts. The results of these measurement are reported in figure 3.2.

Speckle patterns are generated with a Spatial Light Modulator² (SLM), as seen in chapter 2. The linearly polarized laser beam is expanded to cover the SLM window and impinges on it almost perpendicularly. The SLM modulates the wavefront with a random phase pattern that generates speckle illumination in the sample plane. The advantage of using an SLM instead of a static diffuser is that, with an SLM, one can easily control the extension of the speckle pattern in the sample and switch between a speckle scanning mode and a normal confocal one. The SLM also allows adding a special phase mask, as for example spiral, which generate doughnut shaped beams. We used such phase masks in the development stages and to measure the effect of the axial component of the field, as illustrated in chapter 2.

The speckle grain size is controlled through a variable iris positioned just before the SLM, which allows changing the NA of the system, by under-filling the objective pupil with the excitation beam. The SLM and the objective back aperture are conjugated. When the iris is fully open, the beam reflected by the SLM covers completely the objective back aperture while, by closing the iris, we can under-fill the pupil therefore simulate a lower NA system and obtain speckle patterns with different average grain sizes.

Scanning is performed with a pair of galvanometric mirrors which are controlled analogically. Since they are conjugated to the objective back aperture, the tip and tilt that they add to the beam is translated into an horizontal and vertical displacement of the illumination pattern in the focal plane. Thanks to this, we can scan a fixed speckle pattern over the sample.

A quarter-wave plate positioned just before the objective changes the polarization from linear to circular. As we have seen in chapter 2 and better explained in appendix A.6, this particular polarization state allows optimizing the axial component in half of the speckle phase singularities and ensures the high contrast which is needed for saturation and therefore super-resolution. Also it causes an isotropic resolution improvement, as we will see in detail later on.

The objective is a 1.4 NA oil immersion³. We chose a high NA objective so that we can reach the theoretical resolution limit of optical microscopy (~ 200 nm) and prove that our technique allows achieving a finer detail. Besides, the high NA improves the collection efficiency of the emitted fluorescence signal.

Detection. The fluorescence coming from the sample travels back along the same path of excitation, and is filtered by a dichroic mirror and either imaged onto a CCD camera, used for

²Hamamatsu Photonics, LCOS, X10468-01.

³Olympus, Tokyo, Japan, 100 \times , NA 1.40, UPLanSApo, Oil.

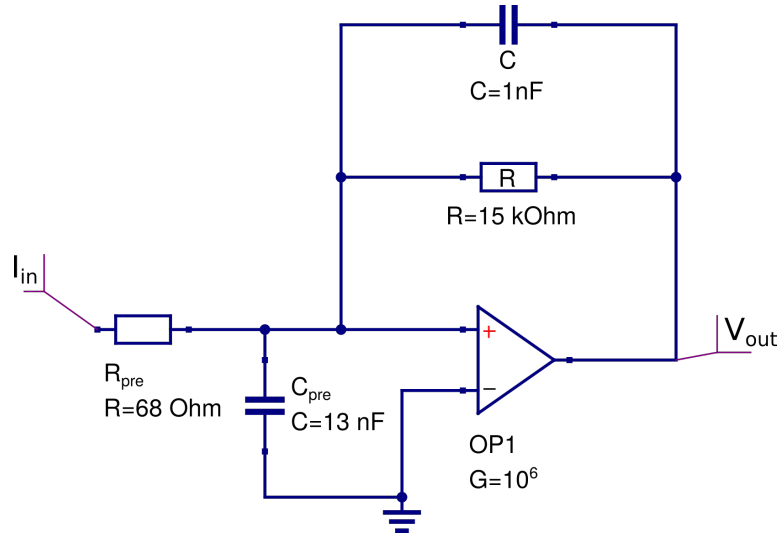


Figure 3.3 – schematic view of the transimpedance amplifier used to filter and amplify the PMT signal. It is composed of a passive pre-filter which has a cut-off frequency of 180 kHz and the active RC filter explained in the text. The gain of the filter is $G=10^6$

the preliminary analysis and adjustments of the sample, or directed to a Photo-Multiplier Tube⁴ (PMT) which is conjugated to the objective back aperture. The PMT converts the incoming light into a voltage difference proportional to the light intensity, that can be read through an acquisition device. The PMT responds extremely fast to the light stimulus, faster than our acquisition device, which is why we designed a RC low-cut filter for the PMT output. The constraints in the implementation of the filter were consisted in the need of a cut-off frequency at about the double of the pulse rate, of a sensitivity to the single photon detection and to stretch the pulses enough to compensate the pulses jitter ($\tau_j = 0.26 \mu\text{s}$). Consequently we have found the appropriate values of R and C. The PMT anode luminous sensitivity ALS_{PMT} is $1.8 \times 10^6 \text{ C J}^{-1}$. One photon of 532 nm carries an energy of $hc/\lambda = 3.6 \times 10^{-19} \text{ J}/\phi$. Therefore the charge produced by the PMT for the detection of one photon is

$$Q_\phi = 6.48 \times 10^{-13} \text{ C}/\phi \quad (3.1.5)$$

The value of the capacity $C=1 \text{ nF}$ that we chose converts this charge to a difference of potential ΔV higher than the acquisition sensitivity.

$$\Delta V = \frac{Q_\phi}{C} = 0.65 \text{ mV} \quad (3.1.6)$$

⁴Hamamatsu Photonics, H10721-20.

The value of $R=15\text{ k}\Omega$ is chosen to obtain a cut-off frequency slightly higher than the double of the laser pulse rate:

$$f_0 = \frac{1}{2\pi RC} \simeq 10\text{ kHz} \quad (3.1.7)$$

The signal that comes out of our low pass filter is the convolution of the PMT signal with the filter's impulsive response, a *sinc* function which is roughly $2/f_0 = 0.2\text{ ms}$ broad, shorter than the pulse repetition rate (0.25 ms) but much larger than the pulse jitter ($\approx 0.26\text{ }\mu\text{s}$).

Pulse emission and acquisition are synchronized with the same digital trigger. The rising front of the signal triggers the laser pulse emission while the falling front trigger the acquisition. The length of digital pulse (between rising and falling) sets the delay of acquisition. It is determined by the optical path length and the properties of the FP and was experimentally measured to be $4.2(3)\text{ }\mu\text{s}$.

Consequently, the filtered signal is easily measurable with our acquisition device.

The samples that we used to test our saturated speckle microscope are either fluorescent nano-spheres or fluorescent-marked actin filaments.

The carboxylate nano-spheres, of diameter 100 nm or 170 nm are marked with a FP which has its absorption and emission peaks at 540 nm and 560 nm . They were spin-coated on carefully cleaned glass cover-slips, in a 2% PVA (Polyvinyl alcohol) solution, then the cover-slip was mounted on a glass plate to fit on the microscope sample holder and avoid discontinuity of the refractive index. To mount the sample we have used Fluoromount⁵, an aqueous based non-fluorescent mounting medium ($n=1.4$) that hardens and chemically helps preserving the beads fluorescence from photo-bleaching. When PVA dries while spin-coating, it forms a polymer network that holds the beads tightly to the coverslip, thereby avoiding their dispersion in the mounting medium bulk.

Samples of actin were prepared on a coverslip functionalized with myosin 1b [YMLTW⁺14, AYT⁺11]. The actin monomer was labelled with a concentration of Alexa Fluor 546 phalloidin (Invitrogen) in excess, then polymerized in a KCl buffer solution [POA⁺13]. Finally, the sample was mounted in Fluoromount, after several washes.

Whatever the sample, we want to stress the importance of careful cleaning to eliminate any possible fluorescent substance other than the sample itself. The high intensity values needed to reach saturation are associated with significant background signal. Indeed, during the development of the experiment, we have been forced several times to optimize the preparation protocol to reduce parasitic fluorescence from the sample. As an example, a very high contribution to the background signal was given by the immersion oil that we used for the microscope objec-

⁵Sigma-Aldrich.

tive⁶. Although it was characterized as "low-fluorescence" oil (and currently used in STED microscopy in our laboratory), the fluorescence signal coming just from it was not negligible in the experiment and we needed to change it for one specifically conceived for low fluorescence applications⁷. Nevertheless, it was not possible to completely eliminate parasitic fluorescence, which we think is due to the optical components themselves (as for example the glue in the objective lenses), but we eventually reached a background level that was acceptable for our experiments.

3.2 Super-resolution speckle imaging

We present in this section the principle of saturated speckle illumination microscopy. We demonstrate the possibility to perform super-resolution microscopy by saturating fluorescence excitation with a polarized speckle pattern. With this technique we achieved a resolution 3.4-fold above the classical diffraction limit.

3.2.1 Principle

The principle of the experiment is sketched in figure 3.4a. The setup that we have described in section 3.1 allows projecting into the fluorescent sample a speckle pattern of the wanted extension and to scan it in x and y. While scanning, at each position the total fluorescence emitted by the sample is measured and recorded as intensity value. The ordered ensemble of all intensities values corresponding to each scanning position is what we call a **speckle image**.

The speckle image of the sample, in non-saturated excitation mode, is the convolution of the speckle intensity distribution at the sample plane and the object. For example figure 3.4c is the speckle image of one fluorescent nano-bead of 100 nm diameter. In this specific case, since the object can be regarded as point-like, the speckle image shows the speckle pattern itself.

If the excitation intensity is low compared to the saturation intensity I_s of the FP, then the fluorescence signal is proportional to it, whereas, if the excitation average intensity is higher than I_s , we obtain a saturated speckle image, as showed in 3.4d.

In order to know if and how much we are saturating fluorescence acquisition, a precise understanding of the saturation mechanism is fundamental. This is the reason for measuring saturation curves like the one traced in figure 3.4b, which represents the fluorescence signal from the sample as a function of the excitation intensity. One way to measure such curves could be to excite one isolated bead with a diffraction limited spot. However this measure is quite difficult due to the sample drift at the scale during the measure process that can take

⁶Cargille Laboratories Type B 1248.

⁷Zeiss Immersol 518 F (n=1518 @ 23 °C).

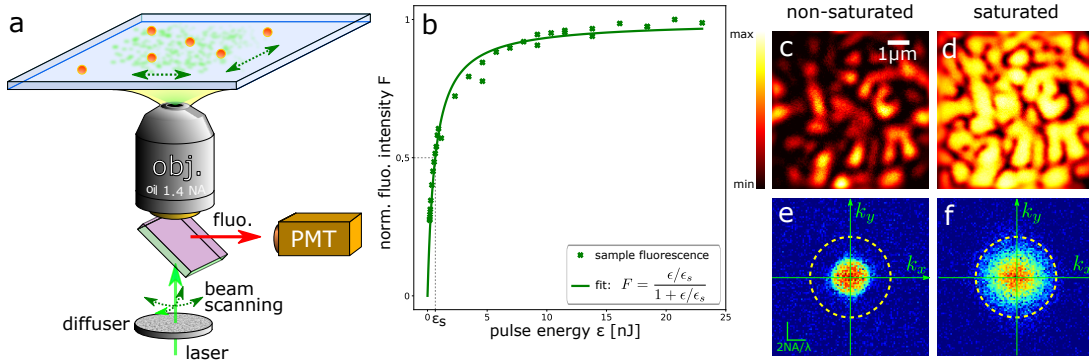


Figure 3.4 – Principle of our speckle scanning microscope: A circularly polarized random wave-field is focused and scanned through an objective lens onto a fluorescent sample (a). The evolution of the fluorescence signal arising from a cluster of beads illuminated with a speckle is plotted in b, as a function of the exciting-pulse energy. The curve is fitted with the function $\langle F \rangle = \langle s \rangle / (1 + \langle s \rangle)$ where we define the average saturation parameter $\langle s \rangle = \langle \epsilon \rangle / \epsilon_s$ with ϵ_s the pulse excitation energy for which fluorescence reaches half the maximum signal (here: $\epsilon_s = 640$ pJ for a $10 \mu\text{m}$ speckle spot). When scanning a single fluorescent nano-bead, we obtain the speckled point spread function (SPSF) for low intensities ($s = 5 \cdot 10^{-3}$) (c) and at high intensity (d) (NA = 0.33). In c, the average saturation parameter is $\langle s \rangle = 3.7$. The saturated speckle exhibits round-shaped dark points at the optical vortices of the speckle pattern. The power spectra of SPSFs in c and d are represented in e and f, respectively, demonstrating the power spectrum enlargement due to saturated excitation, and thus the enlarged support of the optical transfer function of the instrument. In figure (d) phase singularities of the speckle pattern can be seen as small dark spots surrounded by bright fluorescence.

several minutes. Moreover, the exact illumination intensity is difficult to estimate because it depends on the relative position of the bead and the diffraction limited spot. Although we have tried to reduce the system NA in order to produce a PSF much larger than the bead, this approach was unsuccessful.

Instead, the experimental points in figure 3.4b are obtained by illuminating a dense monolayer of nano-beads with speckle illumination and measuring the total fluorescence. In the plot we recognise a characteristic saturation behaviour, but the fitted model does not really correspond to the theoretical fluorescence response to the illumination of our pulsed laser (see appendix C), which would be

$$f = 1 - e^{-s} \quad (3.2.1)$$

because we need to take into account the fact that we are illuminating with a speckle pattern, which has a non-uniform intensity distribution. In fact, if we do consider the speckle intensity distribution as explained in appendix C, a model of the normalized fluorescence signal can be

analytically derived for speckle illumination

$$\langle f \rangle = \frac{\langle s \rangle}{1 + \langle s \rangle} \quad (3.2.2)$$

Here and further, the operator $\langle \cdot \rangle$ stands for spatial mean⁸. The curve plotted in figure 3.4b represents this model. Thanks to saturation curves like this we can measure the average saturation pulse energy ϵ_s for a given spot-size⁹, defined as the pulse energy at half saturation. The FP saturation intensity I_s can be calculated as

$$I_s = \frac{\epsilon_s}{\tau_p \Sigma} \quad (3.2.3)$$

where Σ is the spot surface and τ_p the excitation pulse duration.

When we scan the sample with a speckle pattern using an intensity $I \sim I_s$ or greater, we obtain a **saturated speckle image** as the one shown in figure 3.4d. In an analogy with figure c (linear speckle image), we say that a saturated speckle image is the convolution of the object with the "saturated speckle pattern". Of course, while the term "speckle pattern" refers to the field intensity, a "saturated speckle pattern" does not exist independently, but we can define it by using eq. (3.2.1) as

$$f_{sat}(x, y) = 1 - e^{-\frac{I(x, y)}{I_s}} \quad (3.2.4)$$

where $I(x, y)$ is the distribution of the excitation intensity.

With this interpretation in mind, we could say that the images in figure 3.4c-d represent respectively the speckle-PSF (sPSF) and Saturated-sPSF (SsPSF) of our microscope. Although it is unusual to treat a speckle pattern as a PSF, it is exactly what the term means: the sPSF and SsPSF are the system output obtained when imaging a point-like object.

Finally, the saturation of the fluorescence excitation induces the generation of higher frequencies in the sample than what would have not be allowed by the system in the linear regime. This can be directly observed in figure 3.4e-f which show the Power Spectra¹⁰ of the sPSF

⁸A short clarification on the notation used for mean values in this text. When we use the *overline* notation $\bar{\cdot}$ we refer to the unknown parameter of a distribution. For example, we use this notation when we write the theoretical intensity PDF in fully developed speckle patterns

$$\rho_I(I) = \frac{1}{I} e^{-\frac{I}{I_s}}$$

When we deal with realizations of speckle patterns, we use the bracket notation $\langle \cdot \rangle$ to indicate spatial average. This has to be intended as the average over a certain surface Σ where we measure the quantity of interest. The two notations are equivalent if Σ is infinite

⁹from now on, we use the word *spot* to indicate the disk-shaped speckle pattern projected into the sample. It is important to remark that a small fraction of the energy is also scattered outside the main disk.

¹⁰the definition of Power Spectrum (or Power Spectral Density) refers to the frequency distribution of the energy of a signal s . The signal's energy being defined as $\epsilon = \int |\tilde{s}|^2 d\nu$. The signal's PS is

and SsPSF respectively. The extent of the non-zero region in the power spectrum of an image can be interpreted as a measure of the detail that the image contains. The boundaries of this region represent the cut-off spatial-frequencies of the imaging system. Since the non-zero area of power spectrum of the SsPSF is wider than that of the sPSF, the SsPSF carries more information than the simple sPDF and allows performing super-resolution imaging.

Generalizing, if instead of a point like object we scanned a more complex one, the result would nevertheless be the convolution of the object with the sPSF or the SsPSF, depending on the intensity.

$$I = O \otimes sPSF \quad (3.2.5)$$

$$I_{sat} = O \otimes SsPSF \quad (3.2.6)$$

and the saturated image will have a finer detail than the non-saturated one.

Once we have recognised that saturated speckle images embed more information than linear ones, the successive step is to extract this information. These images, even though they contain super-resolved details, are essentially useless because the object is hidden behind the speckle structure so that they look disordered and meaningless. Therefore the need to reconstruct the object image from the speckle image. In the next section, we will show how this is possible and what are the results.

3.2.2 Super resolution imaging of fluorescent nano beads

The imaging process to produce a super-resolved image with our system consists of 3 steps:

- measurement of the SsPSF (and sPSF)
- acquisition of the speckle image of the sample
- image reconstruction

The sPSF and SsPSF are measured on isolated fluorescent nano beads of 100 nm diameter. The non-saturated sPSF is acquired with the CW laser, whereas we image the SsPSF with the pulsed laser, whose power allows reaching the saturation of excitation. This PSF are measured only once and characterize the system. It is important to notice that the random phase pattern addressed to the SLM corresponds uniquely to a particular realization of the speckle pattern.

$PS[s](\nu) = |\widehat{s}|^2$, or the square modulus of its Fourier Transform.

We remark, for later use, that the PS of a signal is the Fourier transform of its auto-correlation

$$PS[s] = \mathcal{F}[s \star s] = \mathcal{F}[s]\mathcal{F}[s]^* = |\mathcal{F}[s]|^2$$

Therefore, as we change the SLM phase pattern, we need to measure the corresponding sPSF and SsPSF.

Once the sPSF and SsPSF of the system have been acquired, we image the sample with the corresponding speckle pattern and intensity. In order to prove that super resolution is physically achieved thanks to saturation, and not because of the image reconstruction algorithm, we have always taken both the non-saturated and saturated speckle image of our objects.

An example of speckle images of a nano-bead cluster can be found in figure 3.5(e-f). Image (e) is a non-saturated speckle image, while image (f) is saturated with a parameter $\langle s \rangle \simeq 1.4$. Clearly, the speckle images are not intuitive to understand. The image of the corresponding

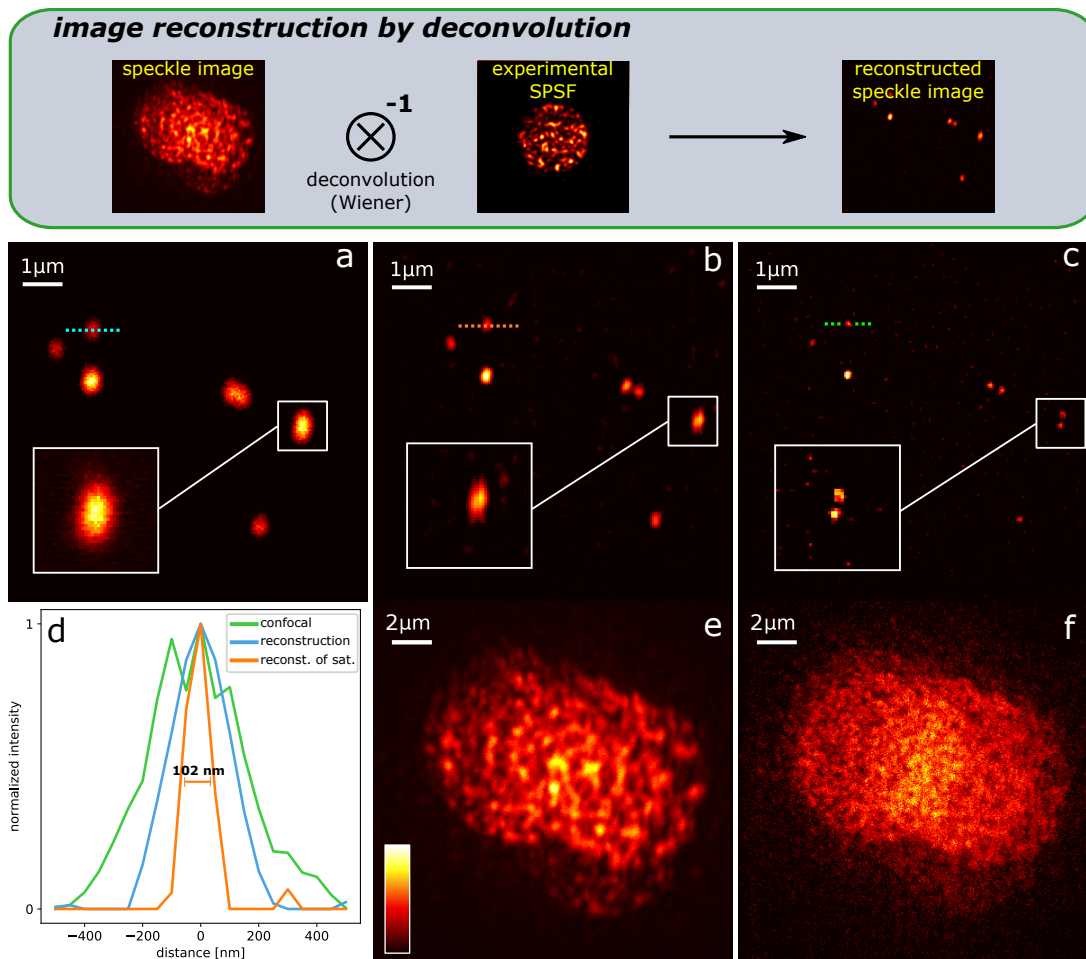


Figure 3.5 – Comparison of an image of 100 nm fluorescent beads taken in confocal mode (a), with images reconstructed from speckle images (by Wiener deconvolution) in the non-saturated (b) and saturated (c) regimes. The comparison of obtained point spread functions in a, b and c, is shown in d. Speckle images corresponding to figures b and c are shown in e and f, respectively. In all images, $NA = 0.77$ and in c, the average saturation parameter is $\langle s \rangle = 1.4$.

object, obtained by scanning with a diffraction limited spot, is shown in sub-figure (a).

In order to reconstruct a useful image of the object from the speckle images, the most immediate tool that we can use is deconvolution, that can be thought of as the inverse operation of eq. (3.2.5), in the sense that we have been explained in section 1.1.2.

Among the many deconvolution algorithms available, we decided to use the simplest one: Wiener deconvolution (see appendix D), because it is also the fastest and does not make any assumptions on the object¹¹.

In figure 3.5(b-c) we show the reconstructions corresponding to the speckle images (e-d). Deconvolution, as it increases the image contrast, can already increase resolution, although the presence of noise limits this effect. However, to be sure that the resolution improvement that we obtain is only due to saturation, we speckle-imaged and reconstructed the object in both linear and saturated regimes.

Indeed the detail of the image is already augmented by deconvolution in linear regime (b), but as one can see from the detail of the two close beads highlighted with a white rectangle, saturation really allows reaching a much finer detail. Namely the two beads are not resolved even after deconvolution in linear regime, while they are clearly separated when deconvolving the saturated speckle image. In sub-figure (d) we show the intensity profile corresponding to the upper-most bead in images (a-c) and we observe the same behaviour: deconvolution improves resolution, but only saturation allows reaching the real bead size: 100 nm. Since the NA used for these images was 0.77, we reach an improvement of 3.4 times the classical limit ($\lambda/2NA = 345$ nm).

3.2.3 Images of actin filaments

In the previous section it has been demonstrated experimentally that super-resolution microscopy can be performed with random illumination patterns, by saturation of fluorescence excitation. It could be argued, though, that the fact of using the same kind of object (nano-beads) for both the speckle PSFs acquisition and object imaging is an excessive simplification and does not correspond to real applications.

To dissolve these doubts, we have imaged a more complex sample of Actin filaments, functionally anchored to a glass substrate with Myosine¹². Figure 3.6 shows the confocal (a) deconvolved- (b) and saturated-deconvolved (c) images of a group of actin filaments, the corresponding speckle images (e-f) and the intensity profiles (d) along the lines traced over

¹¹The Wiener filter it is the maximum likelihood solution under the sole assumption that the noise is additive and independent of the signal.

¹²actin and myosine are a protein couple responsible for motion in most simple and complex living being. Actin spontaneously forms long linear polymers and has specific sites to which myosine has a very high affinity. Therefore myosine anchors spontaneously to actin. In presence of ATP, myosine undergoes a conformational change and pulls the actin filament, originating movement.

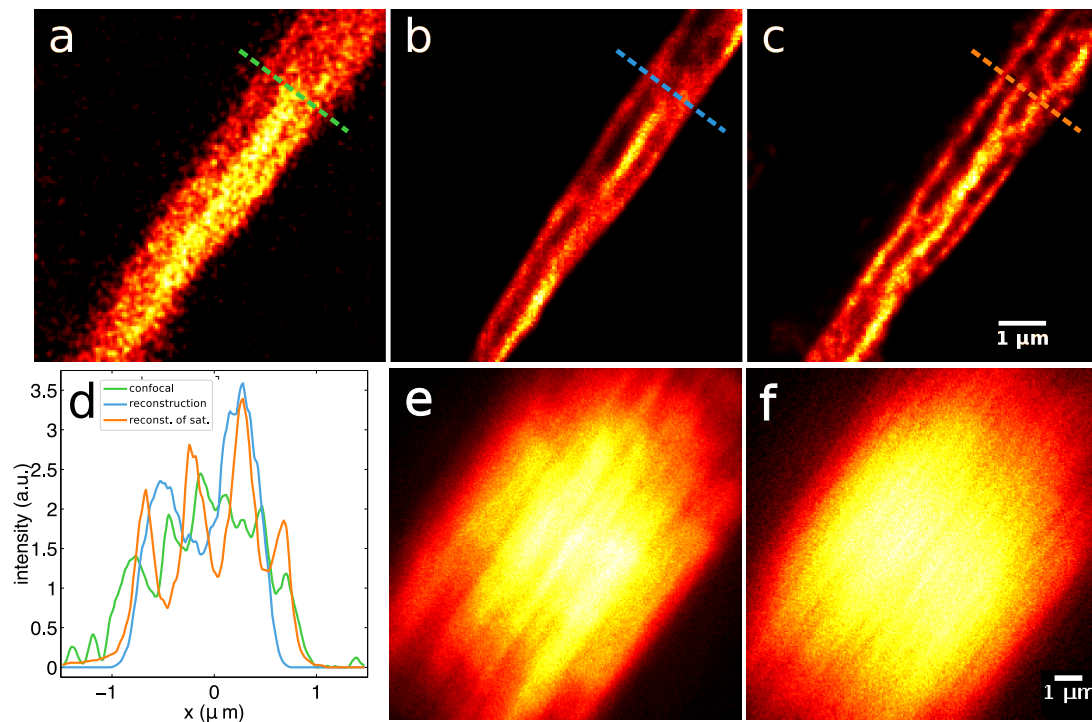


Figure 3.6 – Confocal image of actin filaments deposited on a coverslip (a) and images reconstructed from linear (b) and saturated (c) speckle images (Richardson-Lucy deconvolution). Line profiles corresponding to the dotted lines in Figs. a, b and c are plotted in d. The NA was 0.77 and in image c, the average saturation parameter was estimated to be $\langle s \rangle \simeq 1.4$. Raw speckle images corresponding to images (b) and (c) are shown in figures (e) and (f), respectively.

the images. As expected, although the object has nothing in common with the nano-beads used for the PSF acquisition, saturated-speckle-imaging improves resolution, which confirms the general validity of this technique.

The deconvolution algorithm used in the reconstruction of these images is the well known Richardson-Lucy one¹³. It is an iterative algorithm that assumes a Poisson distribution of the noise in the image. This algorithm performed better in this case probably because the signal to noise ratio was worse than in the nano-beads' case.

A last remark on the preparation of this sample and in general on this imaging technique concerns the need of precise axial positioning. Due to propagation, the speckle pattern evolves and changes dramatically along the propagation axis: two different speckle patterns on the propagation axis which are at a distance larger than $z_{FWHM} = \frac{2n\lambda}{NA^2}$ are completely decorrelated (see appendix A.4). If the speckle image is acquired with a pattern too different from the sPSF, the object cannot be reconstructed by deconvolution. Hence, careful positioning of the sample plane relative to the objective lens is crucial: it must be the same of the one used during the acquisition of the sPSF, with a precision of the order of $z_{FWHM} = \frac{2n\lambda}{NA^2}$. The sensitivity is even higher in the case of the SsPSF, because saturation decreases the correlation distance. Nevertheless, the careful use of a piezoelectric stage allowed to reach the required precision.

¹³the RL algorithm is adapted (i.e. it converges to the MLE solution) for the Poisson statistics. Fluorescence is usually well approximated with a Poisson process, which is one of the reasons why the RL algorithm tends to perform better on fluorescence images. Another reason worth mentioning is that the RL iterations automatically respect positivity; as a result the RL algorithm is less prone to generate spurious Gibbs-like oscillations. See Appendix D.

3.2.4 The finest reachable resolution is NA-independent

Finally, we now discuss and analyse the limit of super-resolution imaging with saturated speckle patterns. At first sight, from the theoretical model (see 2.3.2) and the experimental results of the previous section, one could conclude that with an adequate saturation level $\langle s \rangle$, any arbitrary transverse resolution could be achieved. On the other hand the technique relies on the contrast of the illumination pattern which is granted only if the phase singularities are "dark" enough. In the case of high NA speckle patterns, this constraint becomes important because, at the location of the zeros of the transverse field, the axial component is generally non-zero. Moreover, the mean amplitude of the axial component of the field increases with increasing intensity illumination, thereby reducing the pattern contrast and its ability to confine fluorescence and achieve super-resolution.

The effects of saturation (high values of $\langle s \rangle$) go in two opposite directions: if on the one hand it improves the axial resolution, on the other hand it degrades the contrast in the illumination pattern. Taking into account both effects, we are interested here in finding a theoretical value of $\langle s \rangle$ that allows reaching the best resolution. For this we arbitrarily choose a threshold value of the axial field intensity above which a phase singularity of the pattern is no more contrasted. It is reasonable to fix this threshold at I_s . We assume that a phase singularity of the speckle pattern is well contrasted if there

$$I_z < I_s \quad (3.2.7)$$

In the same way we can say that a speckle pattern is contrasted enough if its mean value of I_z at vortices is smaller than I_s . In this case the fraction of well contrasted vortices according to our criterion can be estimated and is $\simeq 63\%$ in the singularities for which the axial component is optimized and $\simeq 15\%$ in the others.¹⁴

For a speckle pattern of average intensity \bar{I} generated by a top-hat shaped illumination pupil, the average of I_z at the centre of vortices of the transverse field is given by

$$\bar{I}_z = \frac{3}{4} \left(\frac{\text{NA}}{n} \right)^2 \langle I \rangle$$

where n is the refractive index of the immersion medium of the objective. Therefore the

¹⁴In the presented experiments, super-resolution is obtained thanks to the presence of optical vortices, and more precisely, to vortices with large field gradients at their centres. Circular polarization was chosen in order to minimize intensity in the vicinity of isotropic optical vortices of \mathbf{E}_\perp , and of same handedness. However, even in this configuration, the intensity at the centre of the vortices does not perfectly vanish but follows an exponentially decaying probability density function due to the contribution I_z of the axial field. The fractions, indicated in the text, of highly contrasted vortices of the two handedness families that are still well contrasted (according to the criterion $I_z < I_s$) is deduced from eq. 3 in reference [PTEG16].

saturation parameter needed to obtain a speckle pattern with $\bar{I}_z = I_s$ is

$$s_{max} = \frac{4}{3} \left(\frac{\text{NA}}{n} \right)^{-2} \quad (3.2.8)$$

which is the maximum saturation value above which $\bar{I}_z > I_s$. Now, if resolution typically improves as

$$\delta x = \frac{\lambda}{2\text{NA}} \frac{1}{\sqrt{1 + \bar{s}}} \quad (3.2.9)$$

then for $\bar{s} \gg 1$, we get that the utmost achievable resolution is $\delta x \simeq \frac{\lambda}{2n} \sqrt{\frac{3}{4}}$ (which gives $\delta x = 152$ nm in the experimental conditions of fig 3.5). Interestingly, **this limit does not depend on the NA of the imaging lens**. This result suggest that our technique can be used with objectives of low NA, or even simple condensers, and still grant super-resolution. To support this affirmation, we underline that our technique is robust to possible aberrations of the optical system, because it is based on the statistical properties of our illumination scheme (speckle patterns).

In practice, we could get super-resolution slightly beyond the theoretical limit ($\delta_x \simeq 100$ nm actually limited by the bead size), suggesting that the resolution estimated by eq. (3.2.9) is pessimistic. The reason why eq. (3.2.9) under-estimates the super-resolving ability of speckles may be because it involves the average saturation factor \bar{s} while local saturation factors $s(x, y) = I(x, y)/I_s$ in a speckle pattern may be much larger. Local high saturation could thus provide super-resolution information with, apparently, high enough signal.

An illustration of the results we obtained using three different NAs is shown in Fig. 3.7. Resolutions obtained in point-scanning mode as well as after reconstruction from speckle images in the linear and saturated regimes are presented. We observe that both for NA = 0.77 and NA = 1.4, the 100 nm beads are resolved in the saturated regime ($\langle s \rangle = 1.4$ and $\langle s \rangle = 1.6$, respectively). For the 0.33 NA, with a saturation parameter $\langle s \rangle = 2.9$, it was not possible to reach this same resolution because of the too high pulse energy that would have been required: to get a given resolution δx with a given NA, the saturation factor typically scales as: $s \simeq \left(\frac{\lambda}{2\delta x \text{NA}} \right)^2$. For the 0.33 NA images in figure 3.7, average saturation parameter larger than 7 would thus have been required but this was not possible, as we will see in the following section.

The fact that the energy required to achieve a given super-resolution detail increases with decreasing NA can be intuitively understood by taking in consideration the normalized average magnitude of the gradient of the intensity distribution of a fully developed speckle pattern.

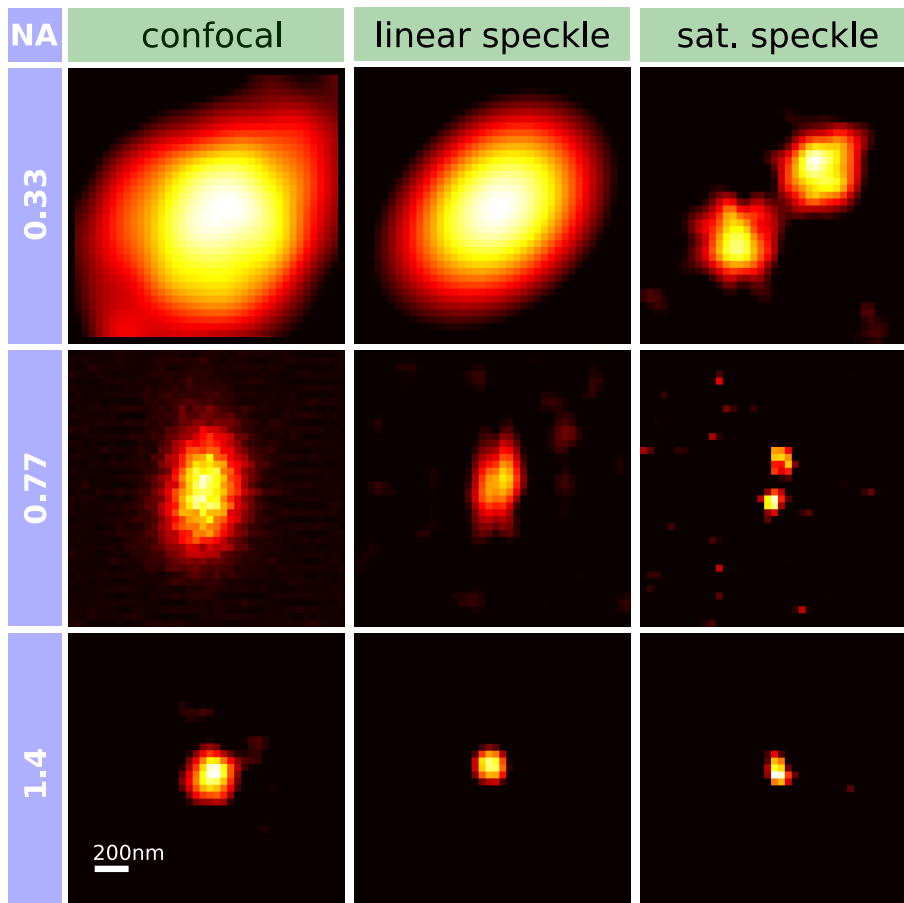


Figure 3.7 – Reconstructed super-resolution speckle images (Wiener deconvolution) of fluorescent beads for different NAs. For $NA = 0.33$, $NA = 0.77$ and $NA = 1.4$, the saturation parameters are $\langle s \rangle = 2.9$, $\langle s \rangle = 1.4$ and $\langle s \rangle = 1.6$, respectively. The scale bar is the same for all images.

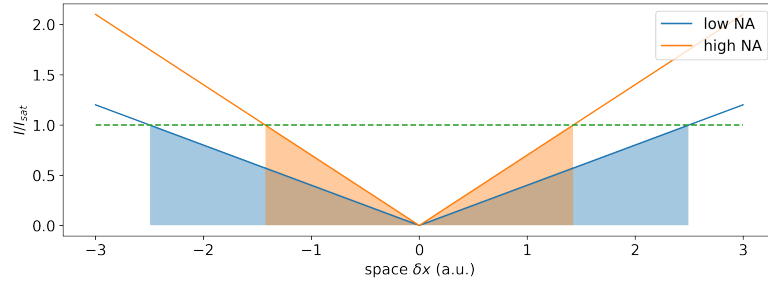


Figure 3.8 – Sketch of the average gradient of the intensity around a phase singularity in a speckle pattern. The two lines correspond to two different NA. The filled areas show the region where the intensity is below a fixed level, here I_{sat} (dashed green line). The extent of this region increases with decreasing NA.

This can be analytically derived from statistical considerations [Goo06] and is

$$\frac{|\Delta I|}{\langle I \rangle} \propto NA \quad (3.2.10)$$

Therefore two speckle patterns with different NA but equal mean intensity have a different behaviour in the vicinity of a generic phase singularity (represented in figure 3.8). The intensity at the centre of the singularity is zero and increases when moving away from it. The average radial distance δx required to reach a given intensity is, in average,

$$\delta x = \frac{I}{|\Delta I|} \propto \frac{1}{NA} \quad (3.2.11)$$

inversely proportional to NA. Therefore, in order to reach the same resolution level δ_x , the low-NA pattern must have a higher average intensity than the high-NA one.

3.2.5 Noise and bleaching

Since at fixed energy the resolution improvement scales as $1/\text{NA}$, high energy are needed in the case of small NAs if a high resolution is wanted. On the other hand, using too high energy pulses has two drawbacks: - First, it increases photo-bleaching (which follows almost linearly the pulse energy as shown in Fig. 3.10) and thus reduces the statistics of the speckle image - Second, it increases the background signal coming from the optics. Both effects degrade the signal to noise ratio (see Fig. 3.9). In our case, the background signal critically degraded intensity minima and its effect was more important than photo-bleaching.

Parasitic background signal was probably the problem we had to cope the most with, during the development and testing of the setup. Eliminating any signal coming from elsewhere but the sample plane (sample bulk, immersion oil, dirt, optics) was a long but necessary task, in order to optimize the acquisition of well contrasted speckle images. To give an example among others, before using an aqueous based PVA solution to dilute the fluorescent nano-beads and spin-coat the sample glass, we used an other polymer, PMMA dissolved in chloroform, much easier to spin-coat. The alcohol, though, also dissolved a very small fraction of the beads dye and some of it remained on the sample after spin-coating. When pouring the mounting medium on the sample, this dye diffused in the solution producing a very intense background which prevented the acquisition of speckle images.

At very high intensity, also the energy that is scattered outside of the speckle spot (the disk projected in the sample) gives an important contribution to the total fluorescence. Therefore we put an iris to stop it, in an intermediate image plane.

Besides parasitic signal, speckle images are deteriorated by photon noise. As it is proportional to the square root of the photon count, its effect can be important, especially in pulsed illumination mode, where the photon count per excitation is relatively low. Obtaining a good signal to noise ratio is fundamental, because upon it depends the efficacy of deconvolution (see appendix D). In appendix B we sketch a simple model of the fluorescence intensity distribution in saturated speckle patterns taking into account photon noise and we compare it to experimental results.

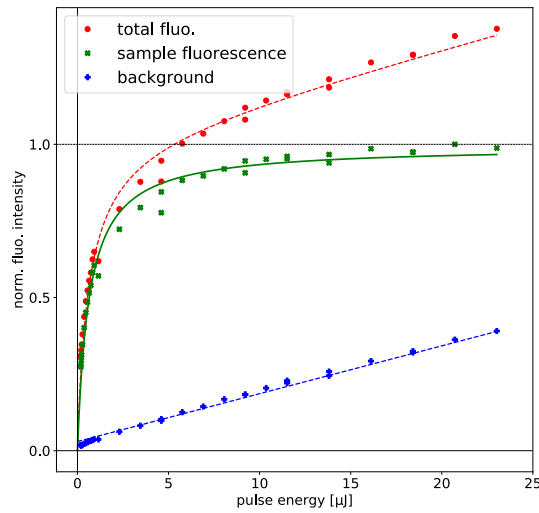


Figure 3.9 – Characterization of the excitation curve of the fluorescent nano-beads. The raw signal (red circles) contains both the contribution of bead fluorescence and the one of the background. The latter may be characterized in the absence of fluorescent bead (blue crosses). Subtracting the background to the raw signal gives the excitation curve of the fluorescent nano-bead (green x-crosses). For this experiment, a cluster of fluorescent beads was illuminated with a speckle pattern and the fitting curve thus takes into account the statistics of the intensity distribution.

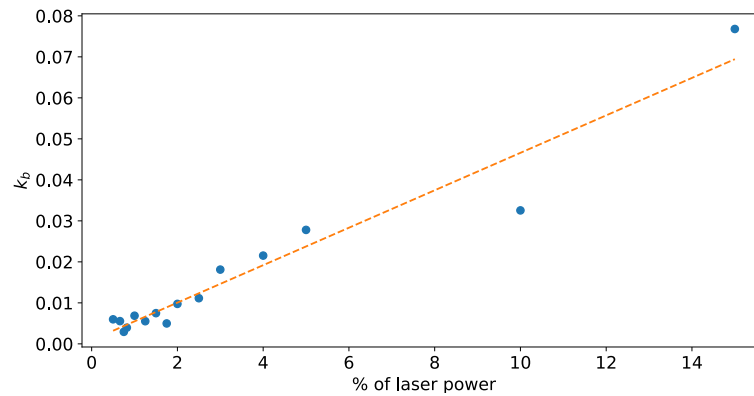


Figure 3.10 – Evolution of photo-bleaching rate with laser power. Here single fluorescent 100 nm nano-beads were photo-bleached under illumination by a focused spot of 0.22 NA. The photo-bleaching rate τ_b is a dynamic parameter of the FP, describing the rate at which the molecules undergo conformational transformations that permanently annihilate their fluorescence capability (see section 2.3.2).

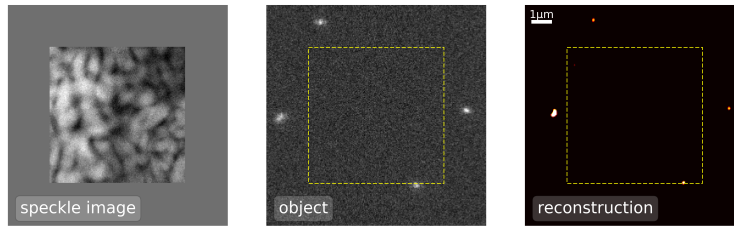


Figure 3.11 – Reconstruction of objects outside of the scanning field of view. On the left a speckle image of an area in the sample which was apparently empty. A fluorescence signal shows the presence of objects outside of the scanning area. Indeed 4 beads are visible when point-scanning a wider area (central image). These beads contribute to the signal recorded in the speckle image. By deconvolution, the 4 beads are recovered (right). The yellow dashed square shows the scanning area of of the speckle image.

Field of view

When scanning a field of view with a large speckle spot, whose size might be comparable with the scanning area, inevitably some object outside of the scanning area can be reached by the pattern and contribute to the sample fluorescence. This signal can be a disturbance for the reconstruction of the image, but surprisingly the object lying out of the scanning field can be recovered. In order to do so, it is sufficient to pad the speckle image before deconvolution, so that it results enlarged. A reconstruction of 4 beads out of the scanning field is shown in figure 3.11. We stress the point that the number of pixels in this image is larger than the effective number of scanning points, because of padding. This means that we are indeed "seeing" a larger field of view than what would be possible with point-wise scanning, in the same conditions.

Even though peripheral objects can be reconstructed, their signal is generally dimmer and often undesired. Because of this, and also in order to limit the background noise, we have restricted the field of view of our microscope with an adjustable iris, placed in an intermediate image plane just before the objective.

3.2.6 Blind reconstruction

In most of the applications where speckle patterns arise spontaneously, often as an undesired effect, their intensity distribution is not known. A typical example is imaging through a turbulent or diffusive medium as we have seen in chapter 1. In the same chapter we saw that, even in this condition, it can be possible to recover a speckle image, for example by exploiting the *memory effect*. Thanks to this effect, the speckle pattern can be scanned over the sample without being deformed. Afterwards the image can be reconstructed, for example by using the speckle image autocorrelation and a phase retrieval algorithm.

Our images are produced by scanning the sample with a constant speckle pattern, which simulates what happens in the application cases of the memory effect. Therefore the same image retrieval procedure should work also in our case. Since we obtain a resolution improvement by saturation, we can expect that this same improvement should be observed also in blind reconstruction.

Before answering this question, it can be instructive to look at the autocorrelation function of a saturated speckle pattern in comparison to the non-saturated case. In fact, the reconstruction algorithm presented in chapter section 1.3.2 exploits the fact that speckle patterns have a very peaked autocorrelation function. The main contribution to the autocorrelation width is given by the grain size, but as the pattern is saturated, the intensity becomes more and more homogeneous and the dark holes corresponding to the phase singularities become dominant. Therefore, the autocorrelation of a saturated speckle pattern is even more peaked than a non-saturated one¹⁵. Besides, it drops faster to a flat plateau, whereas non-saturated speckles show fluctuations as it can be seen in the experimental images of figure 3.12 (this will be explained in detail in the next section).

Experimentally, we have succeeded to perform blind image reconstruction for some very simple objects. The results show that indeed saturation improves resolution also in this case, as illustrated in figure 3.13. Specifically, in sub-figure (a) and (b) we see the speckle image of two very close beads that could not be resolved in diffraction limited scanning. (a) is non-saturated and (b) is saturated. Thanks to saturation, in the latter we see the appearance of small fringes, witnessing the presence of the bead doublet, successfully reconstructed by phase retrieval (d).

¹⁵This is understandable because the saturated speckle pattern has a wider power spectrum, and its FT is the pattern autocorrelation.

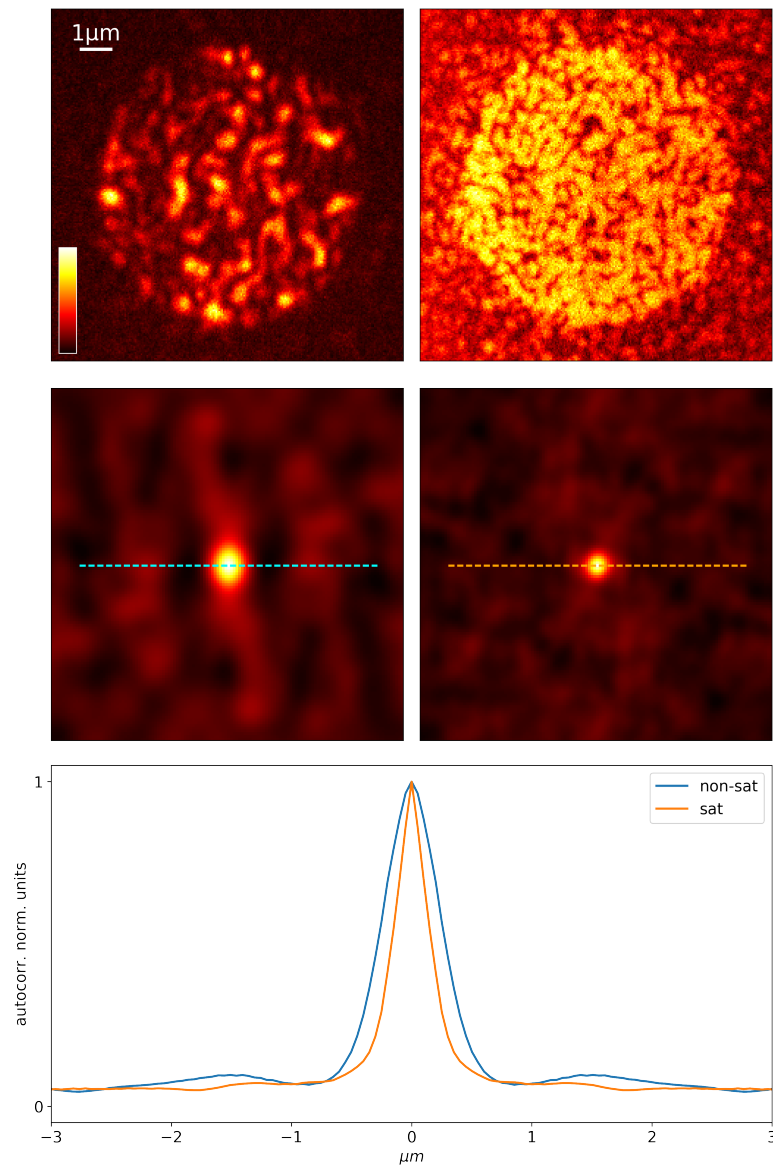


Figure 3.12 – Correlation orthogonality, experimental result with a non-saturated and saturated speckle patterns ($NA = 0.7$). The upper line shows the patterns, the middle line shows the respective auto-correlation whereas the bottom plot shows the radial profiles of the auto-correlations.

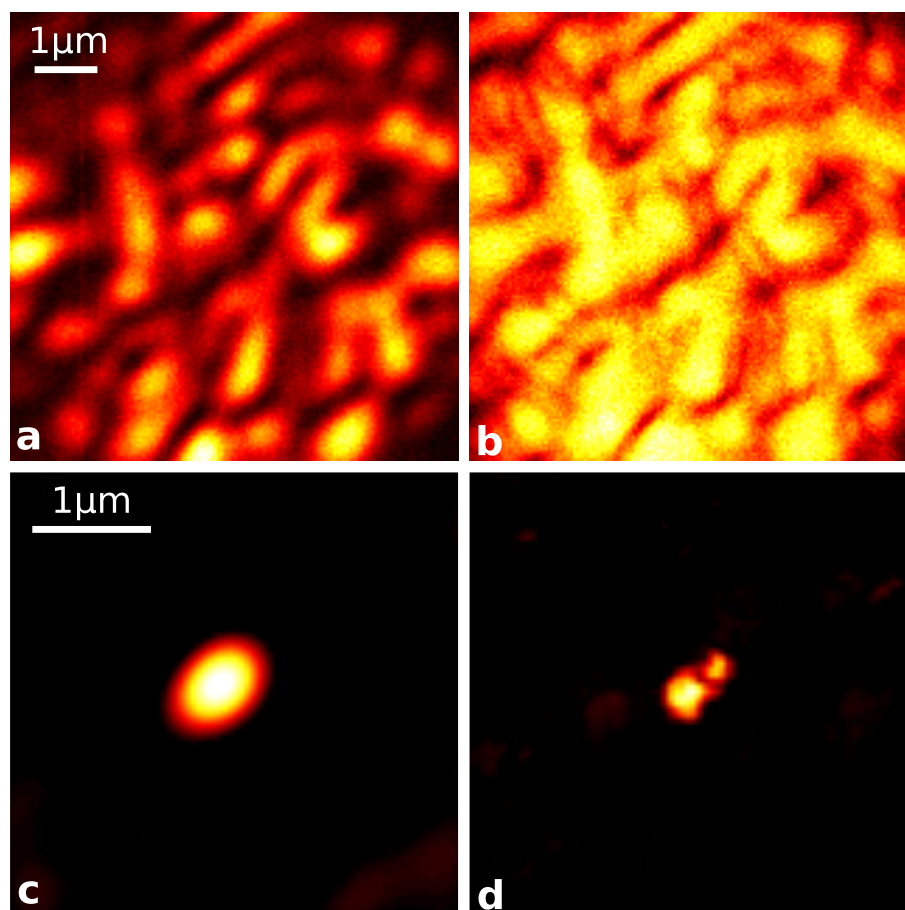


Figure 3.13 – Images of the two nearby fluorescent 200 nm beads obtained with $NA = 0.33$ and shown in Fig. 3.7 (first row). Speckle image in the linear excitation regime (a) and in the saturated regime (b). In the linear regime, the image is reconstructed by Wiener deconvolution (c). Image reconstruction from the saturated speckle image is performed by an iterative phase retrieval algorithm [Fie13] (d). The average saturation parameter in b and d is 2.9 like in Fig. 3.7. The image in d should be compared to Fig. 3.7.

3.2.7 On the axial component in random wave-fields.

As explained in detail in appendix A.6, the polarization state of the speckle field determines the amplitude of the axial field in the phase singularities of the pattern. To summarize briefly, the axial field at the dark spots is generally not zero. This fact can deteriorate the pattern contrast and prevent super-resolution imaging. Luckily, the amplitude of the axial component can be modulated through the field polarization state. Namely circular polarization of a given handedness minimizes the axial component at the phase singularities of the same handedness. The magnitude of the average axial component increases with the objective NA.

Given that we use a high NA objective, the effect of the polarization state should be remarked in our setup. Therefore, we have tried to point it out with two experiments.

The first and simplest consisted in taking two speckle images of an isolated nano-bead, first with right-handed, then left-handed circular polarization and compare them. Since for a given polarization handedness, the axial component is minimized only in the family of phase singularities with the same handedness and maximised in those of opposite handedness, we expect to see a difference in the two images. Moreover, this difference should be more accentuated with increasing saturation, when the only non-saturated signal comes ideally from the optimized singularities.

The experiment requires great stability and precision of the sample, to obtain a good overlap of the speckle images. We recall that, being phase objects, the distance between phase singularities is not limited so that they can be arbitrarily close to each other. Fig.3.14 summarizes the results of this experiment. The same pattern is imaged twice (once per polarization handedness) and then the images are superimposed. For better visualization, the grey values are inverted so that intensity maxima are black, and minima white. The experiment is repeated for 4 increasing saturation values. With increasing saturation, also the average axial component is increased, so if the patterns are almost identical for low \bar{s} , difference can already be seen at $\bar{s} = 1$ and as saturation increases there is almost no overlap of the two images. This points out that our imaging system is indeed sensitive to the axial component, which in turn underlines the importance of using circular polarization to preserve the pattern contrast in the case of high saturation. Even if this experiment is somehow equivalent to the result shown in chapter 2, we have the advantage here to deal with fluorescence excitation instead of photo-bleaching. Excitation, especially with short pulses, is easier to model than photo-bleaching. Moreover the long exposure time during photo-bleaching are a potential problem if the sample drifts

The reason why we have chosen circular polarization is also worth being discussed. As we say in appendix A.6, the probability of finding a singularity with a radially symmetric

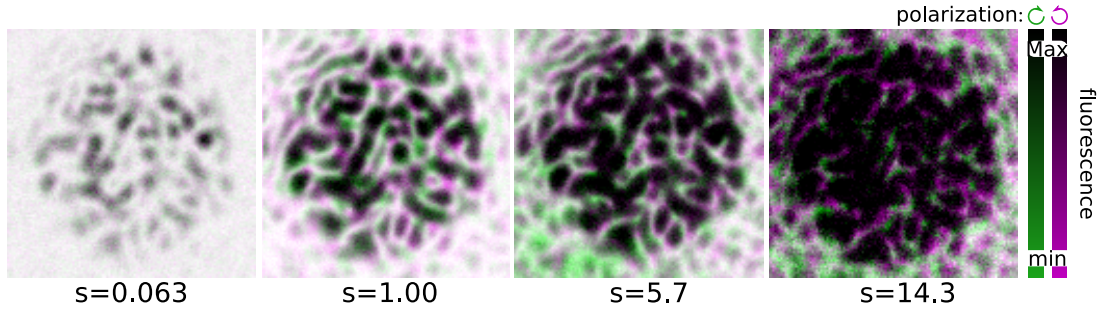


Figure 3.14 – Effect of the axial field on the saturated fluorescence signal. In each image, the green and magenta images are obtained using a single speckle pattern for excitation but using right and left-handed circular polarizations, respectively. Changing the handedness of circular polarization mostly modulates the axial field. Here, the contrast of images have been inverted as compared to usual representation of intensities, in order to better visualize the contribution of the axial field. Bright pixels, thus, represent the dark regions of the speckle which are crucial for super-resolution imaging. From left to right, the saturation parameter s is increased. The significant difference observed between the green and the magenta image observed at large saturation parameters demonstrates the high sensitivity to the axial field. Images taken using a $5 \mu\text{m}$ speckle spot, with $\text{NA} = 0.77$.

intensity profile in a speckle pattern, for which circular polarization would work perfectly, is zero. Nevertheless, this polarization state has the advantage of inducing an anisotropic resolution improvement. Linear polarization, for example, would optimize the axial component of strongly elongated singularity, but only when these are oriented in the same direction of the polarization vector. On the other hand, circular polarization works better for more symmetrical phase singularities and in a way which is not dependent on the orientation of their elliptical profile.

The curiosity to prove if indeed linear polarization could improve resolution on a preferential direction lead us to image and compare the same fluorescent object (a cluster of nanobeads) with a speckle pattern, first circular, then linearly polarized. To compare the resolution improvement we analyse the power spectra of the two images. As expected, only the one corresponding to circular polarization shows an isotropic broadening of the power spectrum, as it can be seen in figure 3.15

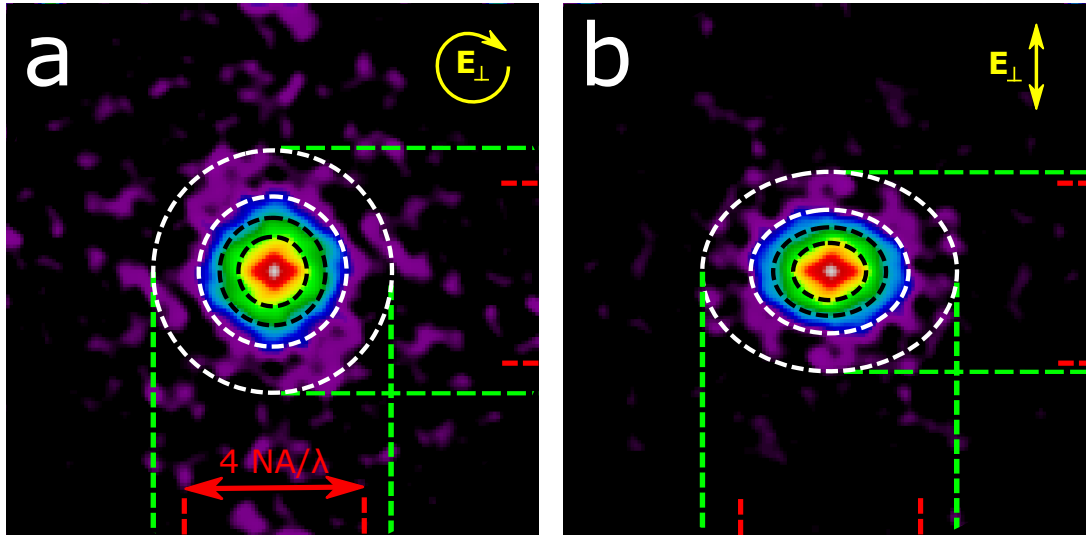


Figure 3.15 – Effect of the polarization state of the speckle pattern on the power spectrum enlargement of the speckle scanning fluorescent image. Circular polarization (a) provides isotropic power-spectrum enlargement while a vertically polarized speckle pattern minimizes the axial field at vortices strongly elongated along the vertical direction, thus enlarging the power spectrum along the horizontal direction (b). Power spectra obtained using $NA = 0.77$ and an average saturation parameter $\langle s \rangle = 1.4$.

3.3 3D reconstruction by 2D scanning

Hitherto, it has been shown that with a rather simple setup it is possible to perform super resolution microscopy thanks to speckle illumination. We will now see that, with the same optical system, we are able to recover full 3D information from a simple 2D speckle image. This is possible thanks to some properties of speckle patterns which we refer to as *orthogonality*.

3.3.1 Speckle orthogonality

Mathematical definition

The concept of *orthogonality* in the ensemble of randomly generated speckle patterns needs to be clarified. The mathematical concept of orthogonality between two elements of a space V requires the definition, on that space, of an operation $p : V^2 \rightarrow \mathbb{R}$ called *inner product*, which associates any two elements of the space with a scalar. Two elements of the space are said to be orthogonal (with respect to that operation) if their inner product is zero.

$$a \perp b \iff p(a, b) = 0 \quad \forall (a, b) \in V$$

Two very common examples are a N -dimensional vector space \mathbb{R}^N , where this operation is the scalar product

$$\mathbf{u} \perp \mathbf{v} \iff \mathbf{u} \cdot \mathbf{v} = 0 \quad (\mathbf{u}, \mathbf{v}) \in \mathbb{R}^N$$

Or the space of L^2 integrable functions on \mathbb{R}^N

$$f \perp g \iff \int_{\mathbb{R}^N} f(\mathbf{x})g(\mathbf{x})d\mathbf{x} = 0 \quad f, g \in L^2$$

Speckle patterns, in a sense that will be clarified later, can be said to be *pseudo-orthogonal* with respect to **cross-correlation**, which is defined as

$$(u \star v)(\mathbf{x}) = \int u^*(\boldsymbol{\xi})v(\boldsymbol{\xi} + \mathbf{x})d\boldsymbol{\xi}$$

or equivalently in the Fourier space as

$$\mathcal{F}[(u \star v)] = \mathcal{F}[u]^* \mathcal{F}[v] \quad (3.3.1)$$

More precisely, since the inner-product should yield a scalar (not a function), we will look at the value of the normalized cross-correlation in $\mathbf{x} = 0$.

$$(u \star v)(0) = \frac{1}{\Sigma} \int_{\Sigma} u^*(\boldsymbol{\xi})v(\boldsymbol{\xi})d\boldsymbol{\xi}$$

Here Σ represents the domain of u and v . If u and v are real signals generated by a random process that follows a given PDF, with finite expected value \bar{u} and variance σ_u^2 , then the cross-correlation in zero yields

$$(u \star v)(0) = \begin{cases} \langle u \rangle^2 & \text{if } u = v \\ \langle u^2 \rangle & \text{if } u \neq v \end{cases}$$

The operator $\langle \cdot \rangle$ represents the mean value over Σ . In the limit of Σ getting infinite, in accordance with the Central Limit Theorem, these values approach the PDF parameters.

$$(u \star v)(0) = \begin{cases} \langle u \rangle^2 \rightarrow \bar{u} & \text{if } u = v \\ \langle u^2 \rangle \rightarrow \overline{u^2} = \sigma_u^2 + \bar{u}^2 & \text{if } u \neq v \end{cases}$$

if the expected value of the random process is 0 and the variance is 1, then this relation becomes

$$(u \star v)(0) = \delta_{u,v} \quad (3.3.2)$$

an orthogonality relation between u and v .

Random speckles

With this in mind, we take the ensemble S of all possible intensity distributions of a speckle pattern extended on the same surface Σ , with the same power spectrum and average intensity \bar{I} . We assume that Σ is large enough to grant ergodicity: the spatial mean and variance of the intensity are close to the ensemble values $|\langle I \rangle - \bar{I}| < \epsilon$.

Any two elements I_i and I_j of S are *pseudo orthogonal* with respect to the operation

$$c(I_i, I_j) = \frac{1}{\Sigma} (I_i \star I_j)(0) = \frac{1}{\Sigma} \int_{\Sigma} I_i^*(\boldsymbol{\xi}) I_j(\boldsymbol{\xi}) d\boldsymbol{\xi} = \langle I_i \cdot I_j \rangle \quad (3.3.3)$$

In the sense that if $i \neq j$, the probability of having an inner product sensibly different from zero is low. It would be exactly zero if Σ were infinitely extended.

The right member of equation (3.3.3) is the spatial mean value of the product of the two patterns. Since the two patterns are randomly and independently generated

$$c(I_i, I_j) = \langle I_i \cdot I_j \rangle \approx \langle I_i \rangle^2$$

Which is also the result obtained when $|\boldsymbol{x}|$ is larger than the correlation length of the pattern (see appendix A.4).

In the case $i = j$ we obtain the auto-correlation of I_i in zero

$$c(I_i, I_j) = \frac{1}{\Sigma} \int_{\Sigma} |I_i(\boldsymbol{\xi})|^2 d\boldsymbol{\xi} = \langle I_i^2 \rangle$$

As Σ increases, the space means tend to the distribution parameters. With the known statistics of fully developed speckle patterns (see appendix A.3) we have

$$c(I_i, I_j) = \begin{cases} \bar{I}^2 & \text{if } i = j \\ \bar{I}^2 = \sigma_I^2 + \bar{I}^2 = 2\bar{I}^2 & \text{if } i \neq j \end{cases}$$

An analogous reasoning considering two saturated speckle patterns f_i and f_j ($f = 1 - e^{-s}$) leads to similar results:

$$c(f_i, f_j) = \begin{cases} \bar{f}^2 & \text{if } i = j \\ \bar{f}^2 & \text{if } i \neq j \end{cases}$$

The values that we have calculated for \bar{f} and \bar{f}^2 can be found in appendix A.5.

These results are far from the wanted orthogonality relation (eq. (3.3.2)). This happens

because, since we deal with quantities that are non-negative (intensity), we can never obtain zero as mean value: a zero-mean (saturated) speckle pattern does not exist.

Nevertheless, speckle images are just numerical representations of the corresponding speckle patterns, where the intensity values are arbitrarily mapped. In our experiment, for example, the intensities are mapped by the PMT in positive voltage values proportional to the signal intensity. According to the previous considerations, though, it is convenient to operate a transformation that changes these values, in order to obtain zero mean and unitary variance. Such a transformation¹⁶ is

$$I' = \frac{\bar{I}}{\sqrt{\sigma^2(I)}} \left(\frac{I}{\bar{I}} - 1 \right) \quad (3.3.4)$$

which, for fully developed speckle is simply (see appendix A.3)

$$I' = \left(\frac{I}{\bar{I}} - 1 \right)$$

whereas, for saturated speckle patterns (with $s = I/I_s$)

$$f' = \sqrt{2s+1} \left(\frac{f}{\bar{f}} - 1 \right)$$

where we have used the results that we have calculated and reported in appendix A.5.

This transformation can be applied to experimental images using space averages as estimators for the mean value and the variance.

Finally, for the renormalized speckle images, we obtain the wanted orthogonality relations

$$c(I_i, I_j) \approx \delta(i, j) \quad (3.3.5)$$

$$c(f_i, f_j) \approx \delta(i, j) \quad (3.3.6)$$

where the approximation becomes an equality when $\Sigma \rightarrow \infty$.

The whole 2D auto-correlation function of a speckle pattern normalized with eq. (3.3.4), is a function $d(\mathbf{x})$ peaked in $\mathbf{x} = 0$, which falls to zero as soon as \mathbf{x} increases more than a correlation length. With saturation, the autocorrelation becomes even more peaked, because the pattern has an enlarged spectrum. In figure 3.16 we plot a numerical simulation to show this behaviour.

It is interesting to notice that saturation also eliminates the off-peak noise in the auto-correlations. Empirically, this happens because, in a saturated pattern, the dominant contri-

¹⁶for simplicity, we use now the symbol I and f for the speckle images of the corresponding intensity patterns.

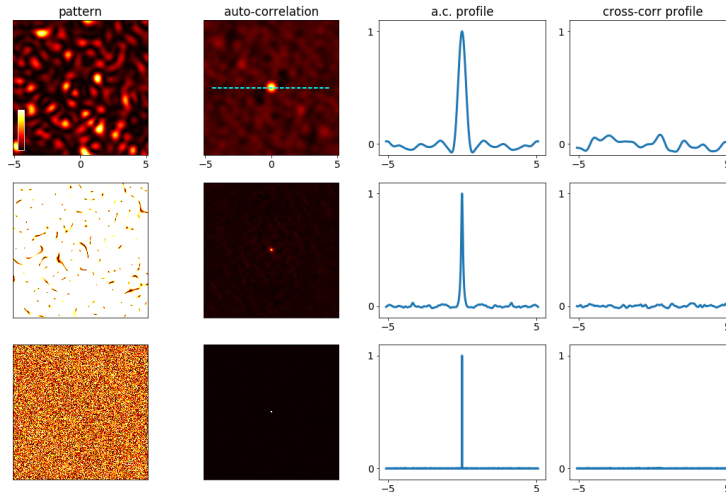


Figure 3.16 – In the first column a speckle pattern (NA=0.5), the saturated version of the same pattern ($\bar{s} = 50$), and some white noise. The second column shows the autocorrelation of the patterns, in the third column we plot the profile of the auto-correlation along the middle line. The last column shows the profile of the cross-correlation of two random patterns. The patterns are normalized and have zero mean and unitary variance. Units are in μm .

tribution to the autocorrelation is given by the dark spots instead of the grains, and the dark spots decrease in size with increasing saturation. In the same figure (last column) we also plot the profile of the cross-correlation of two different patterns. In this case we can not observe any strong correlation: the central peak disappears. Even more interestingly a very similar kind of relation holds for Wiener deconvolution, and is illustrated in the numerical simulation in figure 3.17. The reason can be understood if one looks at the Wiener filter in the Fourier domain (see appendix D)

$$G = \frac{H^*}{|H|^2 + \epsilon}$$

The FT of the restored image \hat{X} is obtained by multiplying G and the FT of the raw image Y .

$$\hat{X} = GY = \frac{H^*Y}{|H|^2 + \epsilon}$$

which, apart from the spectra weighting at denominator, is the cross-correlation between H and Y (cf. eq. (3.3.1)).

$$\mathcal{F}^{-1}[H^*Y] = h \star y$$

Therefore we can affirm that random speckle patterns are *pseudo-orthogonal with respect to Wiener deconvolution*.

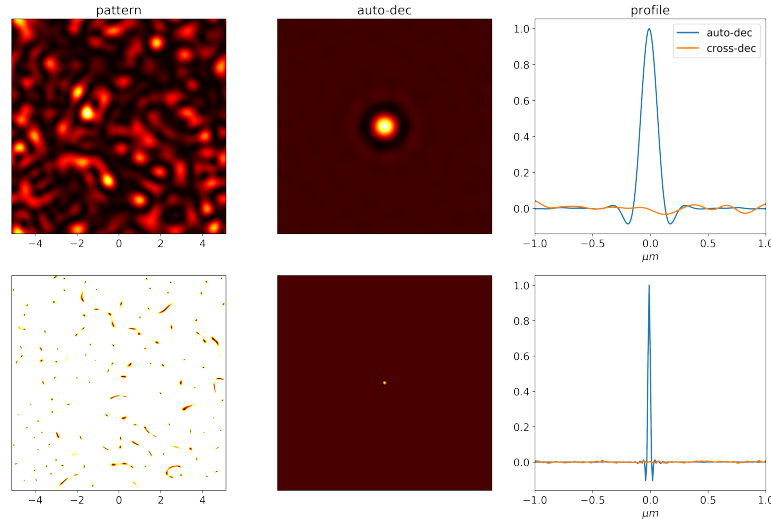


Figure 3.17 – In the first column a speckle pattern ($NA=0.5$) and the saturated version of the same pattern ($\langle s \rangle = 100$). The second column shows a Wiener deconvolution of the pattern with itself. The last column is a plot of the profile of the deconvolution in the middle line (blue) and an analogous profile of the deconvolution of two random speckle patterns of the same kind.

3.3.2 Exploiting speckle orthogonality for 3D imaging

This knowledge is fundamental because it allows performing 3D reconstructions of 2D speckle images. In fact, along the propagation axis, the speckle pattern evolves and totally randomizes after a typical length of $\Delta z \simeq \frac{2n\lambda}{NA^2}$. Because of the orthogonality of random speckle patterns described in the previous section, at this distance the speckles patterns appearing on two planes are decorrelated. This means that if two objects are found in the sample in two different planes at a distance larger than Δz , while imaging, they would contribute to the image with two different and deconvolution-wise orthogonal speckle patterns. Therefore, if we apply deconvolution to the image twice with the sPSFs corresponding to the two distinct planes, we can recover first one plane, then the other.

Extending this reasoning, we could think of imaging a 3D object with a simple 2D scan and deconvolve it with a 3D sPSF of the speckle pattern. In this way we should obtain a 3D reconstruction of the object from its simple 2D scan. Indeed, we have tested this hypothesis and imaged a sample of nano-beads dispersed in volume. The results are shown in figure 3.18.

Of course, the acquisition of the 3D sPSF is time consuming and requires a good precision in the axial positioning and a good stability of the system. Also, in the case of the saturated sPSF (SsPSF) the bead used to acquire it must resist to photo-bleaching (which increases with increasing of the mean saturation parameter), for the duration of acquisition of the whole stack of images. On the other hand, this acquisition needs to be done only once. Once the 3D sPSF is known, 3D images can be reconstructed with a simple 2D scan of the sample, thereby

optimizing acquisition time and photo-bleaching damage.

Some consideration can be done about the limits of this technique: A speckle pattern focused with a microscope objective in the sample has its smallest extension in the microscope focal plane. Since the number of modes (random plane waves) that form it, as well as the average power, are the same along propagation, at increasing axial distance from the focal plane, the average intensity and grain size increase, therefore the saturation level decreases.

Moreover the contrast of the sum of N independent speckle patterns goes as $1/\sqrt{N}$. If N is large, the intensity has a Gaussian distribution as explained in appendix A.2. Therefore the image signal, when speckles from many different planes contribute, has a much smaller dynamic range than a single pattern. More information is then compressed in a smaller range, which could be a limiting factor for reconstruction, hence for the axial field of view.

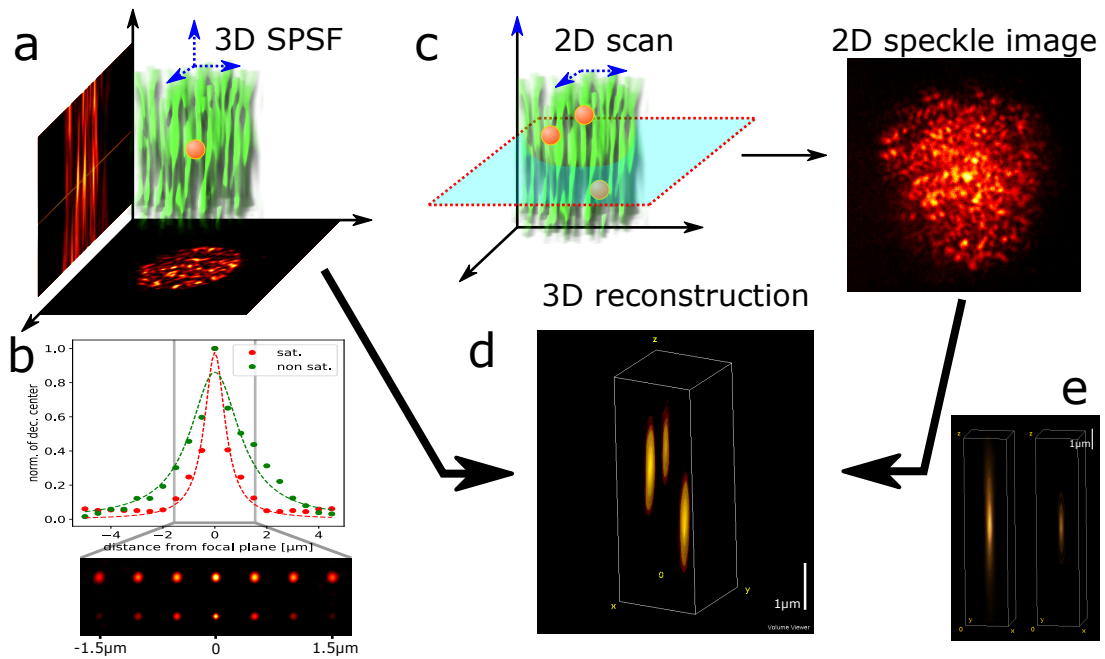


Figure 3.18 – For three-dimensional (3D) super-resolution speckle imaging, the 3D-SPSFs (saturated and non-saturated) are recorded with isolated fluorescent beads (a). The orthogonality of speckle patterns ensures axial resolution after (Wiener) deconvolution. The axial resolution in the saturation regime is improved by a factor $\simeq 2$ as compared to the non-saturated case (b). Once the 3D-SPSF is characterized, a single two-dimensional scan of a three-dimensional sample (c) allows the 3D reconstruction of the object (d). In (e) we show the 3D reconstruction-PSF in non-saturated and saturated mode. Images taken with $NA = 0.77$ and $\langle s \rangle = 1.4$.

Chapter 4

Conclusions

In this work we demonstrated the proof of principle of a new technique for super-resolution optical microscopy, based on saturated speckle illumination. First, we made a short introduction to the concepts of resolution and diffraction limit. Scattering was also introduced as a main issue for super-resolution in diffusive media, such as biological tissues, because in heavy scattering condition it is difficult to shape light and speckle patterns of "random" interference appear spontaneously. Nevertheless we have seen that speckles encode some information and we discussed how they have been used to perform imaging through diffusive media. With this PhD work, we wanted to demonstrate that they can also be exploited to perform super-resolution imaging.

The super-resolution techniques that are based on the saturation of an optical transition require highly contrasted illumination patterns. Speckles, at least in regimes where the paraxial approximation is valid, are contrasted because they feature isolated zeros of intensity (phase singularities). Instead, it had not yet been proven experimentally that, for speckles produced with high NA systems, this contrast is maintained. In fact, in this case, the non-negligible axial component of the field degrades the quality of the intensity zeros in the pattern. In chapter 2 we have reported the experimental proof that circularly polarized light can preserve the contrast in high NA speckle patterns.

Moreover, we have shown that this high contrast can confine an optical transition, a necessary property for super-resolution. According to statistical considerations, we formulated a model describing the average size of confinement. This model is in agreement with the typical resolution improvement of STED/RESOLFT techniques. Since the handedness of circular polarization maximises the axial component only in the phase singularities of the same handedness, we were able to selectively image one family of vortices or the other and even follow the creation/annihilation of two nodal lines in a speckle field.

Once understood that speckles can be used for super-resolution, we have implemented a system to perform super-resolution imaging based on the saturation of fluorescence excitation.

We have straightforwardly observed that images obtained with saturated speckle illumination feature a broader spatial spectrum than those obtained in the linear regime. The raw images acquired in our technique need to be reconstructed and this was already possible by Wiener deconvolution. Clearly the reconstructed saturated speckle images feature finer details than linear ones, hence a higher resolution.

By working on simple fluorescent objects (nano-beads) and more complex ones (actin filaments), we reached a clear resolution improvement which, in some cases, attained almost a factor 4 beyond the theoretical diffraction limit. Moreover, with some simple objects, we have been able to perform double-blind super-resolution image retrieval.

Obtaining these results was not obvious, because of the high levels of noise associated with the high intensities needed for to saturate fluorescence excitation. A careful study and modelling of the phenomena taking place in our experiment, a long optimization and an accurate development of the acquisition system and analysis software was necessary in order to reach satisfactory results. In this phase both experiments and numerical simulations have been determinant to develop a fully functional system.

This optimization process led us to a better understanding of the limitations of our technique and to the discovery of several interesting properties. We observed that, with saturated speckle imaging, the maximum resolution reachable does not depend on the objective's NA, nor on the aberrations of the system. Moreover, our technique does not require expensive optics: a diffuser and a relatively inexpensive diode-pumped solid state pulsed laser are enough to implement it on a scanning microscope.

Eventually, by exploiting the orthogonality of random speckle patterns, we demonstrated the possibility of producing 3D super-resolution imaging with a simple bi-dimensional scan.

To conclude, we can affirm that we have succeeded in our purpose of proving the principle and applicability of saturated speckle super-resolution microscopy.

Future applications in imaging are possible, and need to be investigated. The perspective of using speckle patterns naturally emerging in depth in biological tissue presents some main concerns: In our proof of principle, we have used perfectly stable and known speckle patterns, but, in order to perform in-depth super-resolution imaging, a "memory effect"-like approach should rather be considered. Then, dedicated algorithms of image retrieval could be developed.

On the one hand, since this technique aims towards super-resolution, the relatively small field of view of this effect in biological tissue could be enough to be exploitable. On the other

hand, in our experiment we dealt with fully developed speckle patterns which were produced by a SLM before the objective. A proof is needed to show that the speckles appearing in diffusive media are contrasted enough. This also concerns the conservation of polarization in anisotropic scattering. The literature offers some encouraging results in this sense[GKR98, GGP⁺03,dAGB15].

Finally, the high intensity level needed for fluorescence excitation saturation induce the need to take in consideration any possible source of parasitic fluorescence: biological object show some degree of autofluorescence that we observed in cultured neurons and is reported in the literature[SSP11].

Therefore, it is worth studying the possibility of saturating with speckle patterns an optical transition other than fluorescence excitation, for example depletion, like in STED microscopy. In this case, one could confine fluorescence in the pattern's phase singularity and collect signal only from there, obtaining a much higher signal-to-noise ratio than in the case of excitation.

Applications of 3D speckle-imaging based on speckle orthogonality could also possible and interesting (speckle are a general phenomena due to interference, not limited to light). Further investigation is necessary, and at present we are directing our efforts towards a better understanding of this subject.

Appendices

Appendix A

Speckles

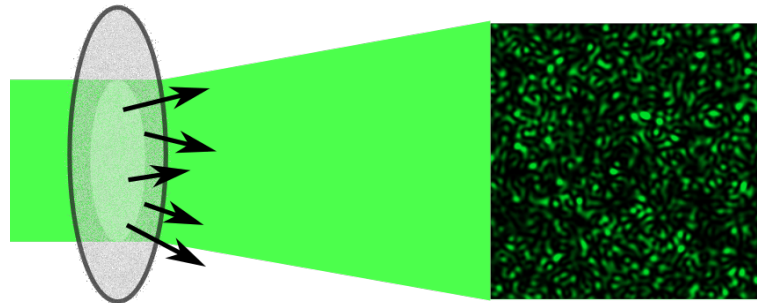


Figure A.1 – generation of a speckle pattern. A plane wave passes through a thin diffuser (e.g. ground glass) and is scattered in a disordered way. Far from the scatterer, a disordered interference pattern appears.

As a coherent plane wave travels through a diffusive medium or bounces on a rough surface, speckle patterns are observed (see fig. A.1). They appear as a spotty structure of bright and dark points, which are randomly distributed. These patterns emerge as a consequence of the uncorrelated and disordered phase shifts generated by the local fluctuations of the diffraction index in the diffusive medium (or the asperities on the rough surface). If each point of the scattering medium is considered as a point-source with random intensity and phase, then, the observed intensity fluctuations in a speckle pattern can be understood as a random interference of many plane waves, where dark points correspond to negative and bright points to positive interference.

A.1 Model of a speckle pattern

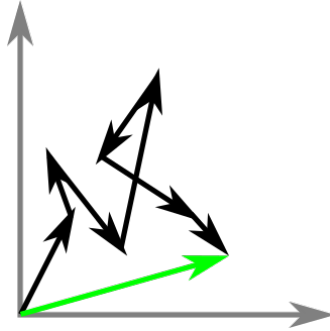


Figure A.2 – random walk seen as the sum of many random vectors in 2D. In the case of speckles, the random 2-dimensional objects that are summed are phasors, representing random plane waves.

On a screen away from the diffuser, each point has an intensity given by the interference of many uncorrelated plane waves which can be represented, in the complex plane, as a sum of random *phasors*, each of them with a randomly distributed length and angle. The result of such sum of random vectors can be seen in the complex plane as "random walk" (fig A.2) and can be written as:

$$\mathbf{A} = A e^{i\theta} = \frac{1}{\sqrt{N}} \sum_{n=1}^N a_n e^{i\theta_n} \quad (\text{A.1.1})$$

where N is the number of plane waves interfering together in the same point and $a_n e^{i\theta_n}$ represents the single, uncorrelated contribution. The factor $\sqrt{1/N}$ has been introduced for preserving a finite norm even when the number of contributions goes to infinity.

Since \mathbf{A} is the sum of N independent and equally distributed random variables, as the number of single contributions N goes to infinity, according to the Central Limit Theorem, the distribution of $\mathbf{A} = \mathcal{R}[\mathbf{A}] + \mathcal{I}[\mathbf{A}]$ converges to a Gaussian distribution in \mathcal{R} and \mathcal{I} which represent the real and imaginary parts respectively.

$$\rho_{\mathcal{R},\mathcal{I}}(\mathcal{R},\mathcal{I}) = \frac{1}{2\pi\sigma^2} \exp\left\{-\frac{\mathcal{R}^2 + \mathcal{I}^2}{2\sigma^2}\right\} \quad (\text{A.1.2})$$

where the variance $\sigma^2 = \text{E}[\mathcal{R}^2] = \text{E}[\mathcal{I}^2]$ depends on the average value of a_n . A speckle that has this distribution, generated by $N \rightarrow \infty$ components, is called a **fully developed** speckle.

From this formalism, many results on the statistical distribution in a speckle pattern can be derived. We will show here the results that are most relevant to this work. A wider and rigorous description of speckle phenomena can be found in ref [Goo06].

A.2 Amplitude distribution

Looking at a particular point in a speckle pattern, the amplitude and phase of the field are given by the random sum of many plane waves as described in the previous section. Given the Gaussian statistic of a fully developed speckle pattern (eq. (A.1.2)), the probability density function (PDF) of the amplitude A and phase θ can be obtained with a simple transformation:

$$\begin{cases} A = \sqrt{\mathcal{R} + \mathcal{I}} \\ \theta = \arctan \left\{ \frac{\mathcal{I}}{\mathcal{R}} \right\} \end{cases} \quad (\text{A.2.1})$$

and is

$$\rho_{A,\theta}(A, \theta) = \frac{A}{2\pi\sigma^2} \exp \left\{ -\frac{A^2}{2\sigma^2} \right\} \quad (\text{A.2.2})$$

With a partial integration on the phase θ , the marginal PDF of the amplitude A is

$$\rho_A(A) = \frac{A}{\sigma^2} \exp \left\{ -\frac{A^2}{2\sigma^2} \right\} \quad (\text{A.2.3})$$

With this PDF, we can calculate the *moments* of the amplitude $\overline{A^p} = \int_0^\infty A^p \rho_A(A) dA$. The integrand is a Gaussian function multiplied by A^{p+1} , which is analytically integrable¹. For example the first two moments are

$$\overline{A} = \sqrt{\frac{\pi}{2}} \sigma \quad (\text{A.2.4})$$

$$\overline{A^2} = 2\sigma^2 \quad (\text{A.2.5})$$

using the last result, the variance σ can be eliminated from eq. (A.2.3):

$$\rho_A(A) = \frac{2A}{\overline{A^2}} \exp \left\{ -\frac{A^2}{\overline{A^2}} \right\} \quad (\text{A.2.6})$$

A.3 Intensity distribution

In optics, the observable which is commonly measured is the intensity I , defined as the modulus of the time averaged Poynting vector [Jac01].

$$I \propto \mathbf{E} \cdot \mathbf{E}^* = |E_x|^2 + |E_y|^2 + |E_z|^2 \quad (\text{A.3.1})$$

¹in term of the Euler's Γ function, the result of the integration is $2^{p/2} \sigma^q \Gamma(1 + \frac{p}{2})$

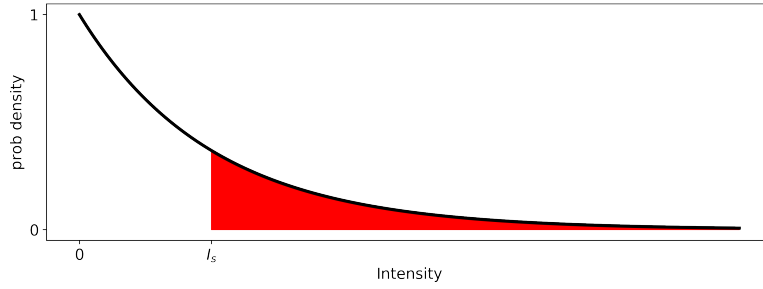


Figure A.3 – The exponential PDF of the intensity in a fully developed speckle pattern. The probability of having an intensity higher than a certain value I_s is represented as the red area below the intensity PDF.

In the paraxial approximation the axial component is small and can be neglected:

$$I = |E_x|^2 + |E_y|^2 \quad (\text{A.3.2})$$

and in the case of a linearly polarized field, if the coordinate versor $\hat{\mathbf{x}}$ is chosen to lie on the polarization direction, the intensity is just

$$I = |E_x|^2 \quad (\text{A.3.3})$$

In the latter equation, $|E_x|$ is the field amplitude, corresponding to A in eq. (A.2.6). Therefore, since the variable transformation $I = A^2$ is monotonic, one can write the intensity distribution in a fully developed polarized speckle pattern:

$$\rho_I(I) = \frac{1}{\bar{I}} \exp\left\{-\frac{I}{\bar{I}}\right\} \quad (\text{A.3.4})$$

which is an exponential distribution (see figure A.3). As we see, lower values of the intensity have higher probability to occur. Also, the exponential distribution has equal mean and standard deviation:

$$\sigma_I = \bar{I} \quad (\text{A.3.5})$$

therefore, as the mean intensity, the *contrast* defined as $C = \sigma_I/\bar{I}$ remains constant.

Another interesting quantity that we can deduce from the intensity PDF, which is used in the text when we speak about saturation, is the probability to find an intensity I higher than a certain value I_s . We obtain it with a definite integration of the PDF (see fig A.3):

$$P(I \geq I_s) = \int_{I_s}^{\infty} \rho_I(I) dI = e^{-\frac{I_s}{\bar{I}}} \quad (\text{A.3.6})$$

Intensity distribution of the sum of uncorrelated speckle patterns

Here we want to study the intensity distribution of the superposition of N uncorrelated speckle patterns.

$$I_{\Sigma} = \sum_{n=1}^N I_n \quad (\text{A.3.7})$$

For fully developed speckle the term independent and uncorrelated can be used interchangeably, due to the statistical model which we have used to describe them. The PDF of the sum of two independent random variables is the convolution of their single PDFs, or, thanks to the convolution theorem, can be obtained as the product of the respective characteristic functions². The characteristic function of an exponential distribution is

$$\phi_I(\omega) = \tilde{\rho}_I = \frac{1}{1 - i\omega\bar{I}} \quad (\text{A.3.10})$$

therefore the characteristic function corresponding to the intensity sum (eq. (A.3.7)) is given by the product

$$\Phi_{I_{\Sigma}} = \prod_{n=1}^N \phi_{I,n}(\omega) \quad (\text{A.3.11})$$

the corresponding PDF is its inverse FT and, in the interesting case of all \bar{I}_n being equal it is

$$\rho_{I_{\Sigma}}(I_{\Sigma}; \bar{I}) = \frac{N^N I_{\Sigma}^{N-1}}{\Gamma(N) \bar{I}^N} \exp\left(-N \frac{I_{\Sigma}}{\bar{I}}\right) \quad (\text{A.3.12})$$

This is a Gamma density function of order N . The mean value and variance are

$$\bar{I}_{\Sigma} = \sum_{n=1}^N \bar{I} = N\bar{I} \quad (\text{A.3.13})$$

$$\sigma_{I_{\Sigma}}^2 = \sum_{n=1}^N \bar{I}^2 = N\bar{I}^2 \quad (\text{A.3.14})$$

so the contrast of the superposition of N speckle pattern scales as $1/\sqrt{N}$:

$$C = \frac{\sigma_{I_{\Sigma}}}{\bar{I}_{\Sigma}} = \frac{1}{\sqrt{N}} \quad (\text{A.3.15})$$

²The characteristic function corresponding to the PDF of a random variable X is defined as the expected value of e^{itX} :

$$\phi_X(\omega) = \mathbb{E}[e^{i\omega X}] = \int_{\Omega} e^{i\omega x} \rho_X(x) dx \quad (\text{A.3.8})$$

and, is the PDF's Fourier Transform. Together with being useful in analysis of linear combinations of independent random variables, the characteristic function has a remarkable property that allows direct calculation of the moments for X :

$$\mathbb{E}[X^k] = \partial^{(k)} \phi_X(0) \quad (\text{A.3.9})$$

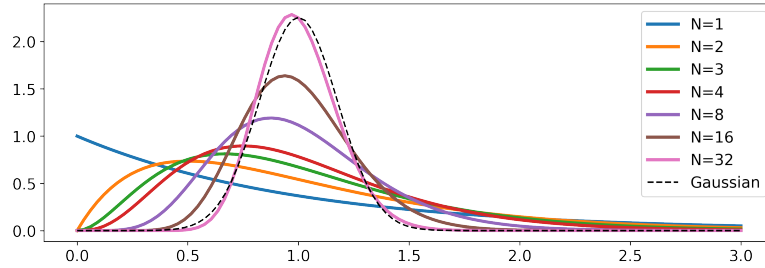


Figure A.4 – Intensity PDF for the sum of several independent speckle patterns. Already when two patterns are summed, the PDF value at $I=0$ drops to zero. As N increases, the distribution converges to a Normal distribution.

The probability of finding an intensity higher than \bar{I}_Σ is obtained by integration of $\rho_{I_\Sigma}(I_\Sigma; \bar{I})$ between \bar{I} . We find

$$P(I_\Sigma > \bar{I}_\Sigma) = (-1)^{N-1} \left(\frac{\partial}{\partial \beta} \right)^{(N-1)} \left[-\frac{e^{-\beta N^2}}{\beta} \right]_{\beta=1} \quad (\text{A.3.16})$$

Which approaches 0.5 as N increases.

An interesting case is for $N = 2$. This is the case of the two components of an un-polarized beam in eq. (A.3.2). The PDF of $I_\Sigma = I_1 + I_2$ derived from eq. (A.3.12) is

$$\rho_{I_\Sigma}(I_\Sigma) = \frac{I_\Sigma}{\bar{I}^2} \exp\left(-\frac{I_\Sigma}{\bar{I}}\right) \quad (\text{A.3.17})$$

interestingly, the probability of having very low intensities drops to zero. We plot this PDF in fig. A.4. Finally we calculate equation (A.3.16) in this case:

$$P(I_1 + I_2 > 2\bar{I}) = \frac{3}{e^2} \approx 0.4$$

Another remarkable fact is that the Gamma distribution converges in probability to a Gaussian distribution $N(\bar{I}, \bar{I}/\sqrt{N})$ for $N \rightarrow \infty$, as it can be seen in fig .A.4. This is a consequence of the Central Limit Theorem, because we are summing many identically distributed uncorrelated variables.

A.4 Grain size

Till now we have described the statistical properties of the intensity in a speckle pattern, but we are also interested in the spatial distribution of the intensities and phases. An important result for the rest of this work is the correlation area of a speckle pattern (which is linked to the average grain size). We will outline here how it is estimated in [Goo06]: we first find a joint PDF for 2 points in the speckle pattern, then use it for the estimations of correlations and expected values.

Joint probability density function

Following the same reasoning that lead us to eq. (A.2.5), we can write the multivariate probability density function of the speckle field \mathbf{A} at two generic points: $\mathbf{A}_1 = \mathbf{A}(\mathbf{x}_1)$ and $\mathbf{A}_2 = \mathbf{A}(\mathbf{x}_2)$. Since \mathbf{A}_1 and \mathbf{A}_2 are complex numbers, the joint PDF $\rho_2(\mathcal{R}_1, \mathcal{I}_1, \mathcal{R}_2, \mathcal{I}_2)$ (analogous of eq. (A.1.2)) depends on four parameters, which are the corresponding real and imaginary parts. Even though the real and imaginary parts of either \mathbf{A}_1 or \mathbf{A}_2 are still independent, \mathbf{A}_1 and \mathbf{A}_2 are not mutually independent *a priori*. With the assumption we have made on the distribution of the random phasors, we have:

$$\overline{\mathcal{R}_i \mathcal{I}_i} = \overline{\mathcal{R}_j \mathcal{I}_j} = 0 \quad (\text{A.4.1})$$

$$\overline{\mathcal{R}_i \mathcal{R}_j} = \overline{\mathcal{I}_i \mathcal{I}_j} = \rho_c \neq 0 \quad (\text{A.4.2})$$

$$\overline{\mathcal{R}_i \mathcal{I}_j} = -\overline{\mathcal{R}_j \mathcal{I}_i} = \rho_s \neq 0 \quad (\text{A.4.3})$$

for $i \neq j$. The joint PDF cannot be written as a simple product of Gaussian distributions for the single 4 variables. Nevertheless an analytical form can be derived³ and a transformation analogous to (A.2.1) allows writing the corresponding PDF of phases θ_1 and θ_2 and amplitudes A_1 and A_2 :

$$\rho_2(A_1, A_2, \theta_1, \theta_2) = \frac{A_1 A_2}{4\pi^2 \sigma^4 (1 - \mu^2)} \exp \left[-\frac{A_1^2 + A_2^2 - 2A_1 A_2 \mu \cos(\phi + \theta_1 - \theta_2)}{2\sigma^2 (1 - \mu^2)} \right] \quad (\text{A.4.5})$$

where $\mu = \mu e^{i\phi}$ is the *complex correlation coefficient* between the speckle field in \mathbf{A}_1 and \mathbf{A}_2 :

$$\mu = \mu(\mathbf{A}_1, \mathbf{A}_1) = \frac{\overline{\mathbf{A}_1 \mathbf{A}_2^*}}{\sqrt{|\mathbf{A}_1|^2 |\mathbf{A}_2|^2}} = \rho_c + i\rho_s = \mu \cos \phi + i\mu \sin \phi \quad (\text{A.4.6})$$

3

$$\rho_2(\mathcal{R}_1, \mathcal{I}_1, \mathcal{R}_2, \mathcal{I}_2) = \frac{\exp \left[\frac{\mathcal{R}_1^2 + \mathcal{R}_2^2 + \mathcal{I}_1^2 + \mathcal{I}_2^2 + 2\rho_s(\mathcal{R}_1 \mathcal{I}_2 - \mathcal{I}_1 \mathcal{R}_2) - 2\rho_c(\mathcal{R}_1 \mathcal{R}_2 - \mathcal{I}_1 \mathcal{I}_2)}{2\pi^2 \sigma^4 (1 - \rho_c^2 - \rho_s^2)} \right]}{4\pi^2 \sigma^4 (1 - \rho_c^2 - \rho_s^2)} \quad (\text{A.4.4})$$

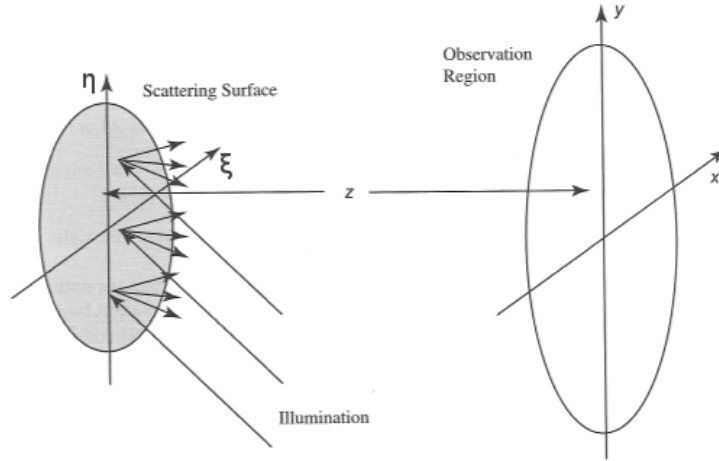


Figure A.5 – Free space geometry. (image source [Goo06]).

The PDF $\rho_2(A_1, A_2, \theta_1, \theta_2)$ can then be used to calculate correlations and expected values.

Intensity correlation in a speckle pattern

With the joint PDF of eq. (A.4.7) it is possible to calculate the correlation of the intensity in a speckle pattern. We report here for clarity the formal derivation of [Goo06], but the only result that will be used in the following section is equation (A.4.15).

A partial integration on the phases θ_1 and θ_2 gives the marginal joint PDF of the amplitudes:

$$\rho_2(A_1, A_2) = \frac{A_1 A_2}{\sigma^4(1 - \mu^2)} e^{\left[-\frac{A_1^2 + A_2^2}{2\sigma^2(1 - \mu^2)}\right]} I_0 \left[-\frac{\mu A_1 A_2}{\sigma^2(1 - \mu^2)} \right] \quad (\text{A.4.7})$$

Where I_0 is a modified Bessel function of the first kind, order zero. Then the monotonic transformation $I = A^2$ allows finding $\rho(I_1, I_2)$ and calculate the expected value of $I_1 I_2$:

$$\Gamma_I = \overline{I_1 I_2} = \overline{I^2}(1 + \mu^2) \quad (\text{A.4.8})$$

which links the intensity correlations to the correlations of the complex field \mathbf{A} through the complex correlation coefficient μ .

The speckle field \mathbf{A} depends on the characteristic of the scattering aperture that generates it (represented as a gray disk in figure A.5). Therefore, also the intensity correlation Γ_I must depend on it. In the following reasoning, we will write the intensity correlation function Γ_I as a function of the field on the scattering aperture $a(\xi, \eta)$.

We first start writing the field correlation on the observation plane $\Gamma_A(\mathbf{x}_1, \mathbf{x}_2) = \overline{A(\mathbf{x}_1)A^*(\mathbf{x}_2)}$. In the paraxial approximation, the field $\mathbf{A}(x, y)$ at the observer plane depends on the field in

the scattering plane $\mathbf{a}(\xi, \eta)$ through the Fresnel diffraction integral [Goo06].

$$\mathbf{A}(x, y) = \frac{e^{ikz}}{i\lambda z} e^{i\frac{k}{2z}(x^2+y^2)} \iint_{-\infty}^{\infty} \mathbf{a}(\xi, \eta) e^{i\frac{k}{2z}(\xi^2+\eta^2)} e^{-i\frac{k}{2z}(x\xi+y\eta)} d\xi d\eta \quad (\text{A.4.9})$$

With this, the field correlation on the observation plane Γ_A can be written as a function of the field correlation at the scattering aperture plane $\Gamma_a(\boldsymbol{\xi}_1, \boldsymbol{\xi}_2) = \overline{a(\boldsymbol{\xi}_1)a^*(\boldsymbol{\xi}_2)}$.

$$\Gamma_A(\mathbf{x}_1, \mathbf{x}_2) = \frac{1}{\lambda z^2} e^{i\frac{k}{2z}(\mathbf{x}_1^2 - \mathbf{x}_2^2)} \iint_{-\infty}^{\infty} \iint_{-\infty}^{\infty} \Gamma_a(\boldsymbol{\xi}_1, \boldsymbol{\xi}_2) e^{i\frac{k}{2z}(\boldsymbol{\xi}_1^2 - \boldsymbol{\xi}_2^2)} e^{-i\frac{2\pi}{\lambda z}(\mathbf{x}_1 \cdot \boldsymbol{\xi}_1 - \mathbf{x}_2 \cdot \boldsymbol{\xi}_2)} d\boldsymbol{\xi}_1 d\boldsymbol{\xi}_2 \quad (\text{A.4.10})$$

We can assume the correlation at the scattering aperture to be sufficiently small that it can be adequately represented by a delta function

$$\Gamma_a(\boldsymbol{\xi}_1, \boldsymbol{\xi}_2) = \kappa I(\boldsymbol{\xi}_1) \delta(\boldsymbol{\xi}_1 - \boldsymbol{\xi}_2) \quad (\text{A.4.11})$$

where κ is a constant that preserves dimensionality and $I(\boldsymbol{\xi}_1) = \frac{\overline{a(\boldsymbol{\xi}_1)a^*(\boldsymbol{\xi}_1)}}{\kappa}$ is the intensity at the scattering aperture. In this case (A.4.10) becomes

$$\Gamma_A(\mathbf{x}_1, \mathbf{x}_2) = \Gamma_A(\Delta \mathbf{x}) = \frac{1}{\lambda z^2} \iint_{-\infty}^{\infty} I(\boldsymbol{\xi}) e^{-i\frac{2\pi}{\lambda z}[\Delta \mathbf{x} \cdot \boldsymbol{\xi}]} d\boldsymbol{\xi} \quad (\text{A.4.12})$$

Where $\Delta \mathbf{x} = \mathbf{x}_1 - \mathbf{x}_2$ and the quadratic phase exponential has been removed for seek of simplicity, since we are interested in the modulus of Γ_A .

The complex correlation coefficient $\boldsymbol{\mu}$ of the field intensity (eq. (A.4.6)) can be rewritten in terms of Γ_A :

$$\boldsymbol{\mu}(\mathbf{A}_1, \mathbf{A}_2) = \boldsymbol{\mu}(\mathbf{A}(\mathbf{x}_1), \mathbf{A}(\mathbf{x}_2)) = \frac{\Gamma_A(\Delta \mathbf{x})}{\Gamma_A(0, 0)} \quad (\text{A.4.13})$$

$$= \frac{\iint_{-\infty}^{\infty} I(\boldsymbol{\xi}) e^{-i\frac{2\pi}{\lambda z}[\Delta \mathbf{x} \cdot \boldsymbol{\xi}]} d\boldsymbol{\xi}}{\iint_{-\infty}^{\infty} I(\boldsymbol{\xi}) d\boldsymbol{\xi}} = \frac{1}{W} \tilde{I}(\Delta \mathbf{x}) \quad (\text{A.4.14})$$

At this point the calculation of the intensity correlation in a speckle pattern is straightforward, since we know that it is related to $\boldsymbol{\mu}$ by eq. (A.4.8).

$$\boldsymbol{\Gamma}_I(\Delta \mathbf{x}) = \overline{I_1 I_2} = \overline{I}^2 (1 + \mu^2) = \overline{I}^2 \left[1 + \frac{1}{W^2} |\tilde{I}(\mathbf{x})|^2 \right] \quad (\text{A.4.15})$$

Which states that expected value of the autocorrelation function $\boldsymbol{\Gamma}_I(\Delta \mathbf{x})$ of a fully developed

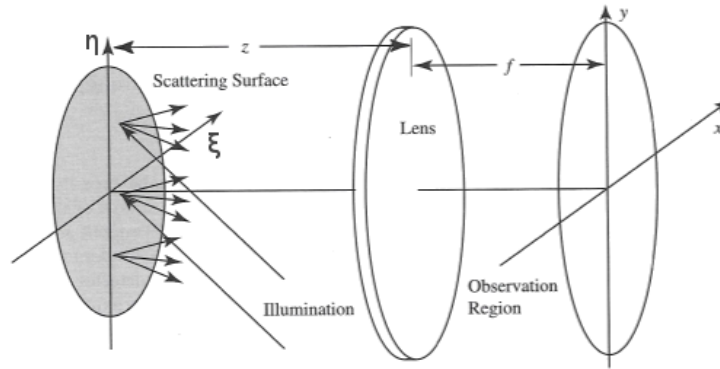


Figure A.6 – Imaging geometry. (image source [Goo06]).

speckle pattern is given by the modulus of the Fourier Transform of the pattern $\tilde{I}(\mathbf{x})$: its power spectral density.

Application to the microscope

The previous discussion was general, valid for free-space propagation and we did not mention any particular optical system. Nevertheless, under certain assumption which are fulfilled in this work (cf. ref [Goo06] page), it can be generalized to any optical system composed of one or more lenses (see schematic in fig. A.6), by considering the last lens as the effective scattering object. Therefore, the intensity correlation of the speckle in the image plane is entirely determined by the FT of the intensity distribution across the system's pupil (eq. (A.4.15)).

With this result, we can calculate the expected "grain size" of a speckle pattern focused by the lens of a microscope, as a function of the objective NA. Since the grains in a speckle pattern are randomly distributed, we expect the correlation function do have a maximum value in zero and drop as soon as $\Delta\mathbf{x}$ reaches the grain size. In order to estimate the expected grain size, we describe the intensity distribution at the objective pupil as

$$I(\boldsymbol{\xi}) = I_0 \text{circ}\left(\frac{2\rho}{D}\right) \quad (\text{A.4.16})$$

with

$$\text{circ}(r) = \begin{cases} 1 & \text{if } r \leq 1 \\ 0 & \text{if } r > 1 \end{cases} \quad (\text{A.4.17})$$

Since the FT of eq. (A.4.16) is

$$\tilde{I}(\Delta\mathbf{x}) = AI_0 2d J_1\left(\pi \frac{r}{d}\right) \quad (\text{A.4.18})$$

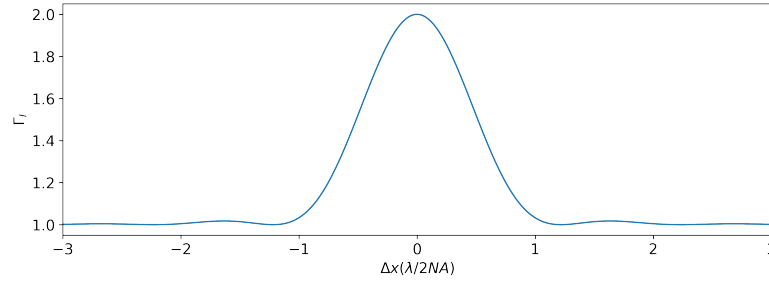


Figure A.7 – correlation function of a fully developed polarized speckle pattern, focused by an objective of a given NA.

with $A = \pi(D/2)^2$ the aperture surface, $r = \sqrt{(\Delta x)^2}$ and $d = \frac{\lambda z}{D} = \frac{\lambda}{2NA}$. Then, we can calculate the intensity correlation in the image plane with eq. (A.4.15).

$$\Gamma_I(r) = \bar{I}^2 \left[1 + \left| 2d J_1 \left(\pi \frac{r}{d} \right) \right|^2 \right] \quad (\text{A.4.19})$$

plotted in figure A.7. The correlation drops at a distance approximately equal to the system resolution defined as $d = \frac{\lambda}{2NA}$. Hence, $d = \frac{\lambda}{2NA}$ is also an estimate of the expected value of the grain size in a fully developed polarized speckle pattern focused with an objective numerical aperture NA.

The speckle average grain size in the axial direction can be calculated in an analogous way. The result found in this case is proportional to $1/NA^2$. To resume this section we give the estimate of the Full Width at Half Maximum (FWHM) of the intensity correlation function in the transverse and axial cases, which are an estimate of the average speckle grain size:

$$r_{\text{FWHM}} = \frac{1.4\lambda}{NA} \quad (\text{A.4.20})$$

$$z_{\text{FWHM}} = \frac{6.7\lambda}{NA^2} \quad (\text{A.4.21})$$

A.5 Distribution of fluorescence in saturated speckle patterns

In this section we report our derivation of the PDF for the intensity of fluorescence in a saturated speckle pattern. We start from the PDF of the intensity in a fully developed polarized speckle pattern (eq (A.3.4)), which we re-write here for convenience, as a function of the saturation parameter $s = I/I_s$

$$\rho_s(s) = \frac{1}{s} \exp \left\{ -\frac{s}{s} \right\}$$

To obtain the statistics of fluorescence intensity of a saturated speckle pattern, we use the model of fluorescence intensity in pulsed excitation mode (eq. (C.0.7)).

$$f = 1 - e^{-s}$$

and obtain

$$\rho_f(f) = \rho_s(s) \left| \frac{ds}{df} \right| = \frac{1}{\bar{s}} (1-f)^{\frac{1}{\bar{s}}-1}$$

With this we can calculate the expected value \bar{f} , but it is easier to calculate $\overline{1-f} = 1 - \bar{f}$

$$\overline{1-f} = \int_0^1 \frac{1}{\bar{s}} (1-f)^{\frac{1}{\bar{s}}} df = \frac{1}{1+\bar{s}}$$

then

$$\bar{f} = \frac{\bar{s}}{1+\bar{s}} \quad (\text{A.5.1})$$

In the text we also use the mean values of I^2 and f^2 , which we calculated by integration of the respective PDFs.

$$\overline{I^2} = 2\bar{I}^2 \quad (\text{A.5.2})$$

and

$$\overline{f^2} = \frac{2}{\left(\frac{1}{\bar{s}}+1\right)\left(\frac{1}{\bar{s}}+2\right)} \quad (\text{A.5.3})$$

With the latter, we calculate the variance of f

$$\sigma^2(f) = \overline{(f-\bar{f})^2} = \overline{f^2} - \bar{f}^2 = \frac{\bar{f}^2}{(2\bar{s}+1)}$$

for low values of \bar{s} we recover $\sigma^2(f) = \bar{f}^2$, because the fluorescence is directly proportional to the excitation intensity, which in turn follows an exponential distribution ($\sigma^2(I) = \bar{I}^2$). Whereas for high values of \bar{s} , the normalized fluorescence is almost everywhere 1 therefore the variance goes to zero.

Autocorrelation in zero

In section 3.3.1 of the text, we calculate the autocorrelation in zero $c(I_i, I_j)$ of appropriately normalized speckle patterns and we find the pseudo-orthogonality relation

$$c(I_i, I_j) = (I_i \star I_j)(0) = \delta_{i,j}$$

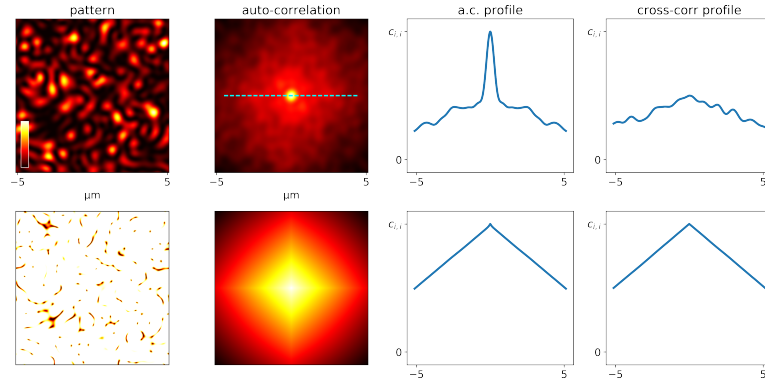


Figure A.8 – auto- and cross-correlation of simulated speckle patterns ($NA=0.5$). The pattern on the second line is saturated with $\bar{s} = 50$. The last column shows the profile of the cross correlation of two randomly different speckle patterns.

Which is only true for patterns with zero mean and variance equal to one. Since intensities are positive quantities, $\langle I \rangle$ cannot be zero unless an appropriate transformation is applied.

In an image of a speckle pattern, the effect of the non-zero mean is to add a triangle-like background, which is the correlation of a constant image with the same mean value.

It is interesting to evaluate the peak to base ratio, to understand how this effect deteriorates the peaked shape of the auto-correlation function. For speckle patterns of mean $\langle I \rangle$

$$\frac{c(I_i, I_i)}{c(I_i, I_j)} \approx \frac{2\bar{I}^2}{\bar{I}^2} = 2$$

where the approximation of the mean value to the expected value is valid under the hypothesis that space mean $\langle \cdot \rangle$ is evaluated over a surface much larger than the speckle coherence area.

If we take two different saturated speckle patterns, with average saturation parameter $\langle s \rangle$, with the results found just before we find a ratio

$$\frac{c(f_i, f_i)}{c(f_i, f_j)} \approx \frac{2\bar{s} + 1}{2\bar{s}}$$

which tends to 1 as \bar{s} becomes large, meaning that the peak tends to disappear with increasing saturation. Figure A.8 illustrates this on numerically simulated speckle patterns.

In the text we are interested in defining an orthogonality relation for random speckle patterns based on cross-correlation, for which $c(I_i, I_i)$ and $c(f_i, f_i)$ vanish if $i \neq j$. This imposes the necessity of manipulating zero-mean quantities, as explained in section 3.3.1.

A.6 Eccentricity of the phase singularities

This work is mainly concerned in the quality of the dark spots of speckle pattern. At the locations of phase singularities, the transverse field is zero, so the axial component plays a crucial role. Its amplitude can be modulated by the field polarization state. To explain how, we describe in this section the morphology of phase singularities and the role of polarization.

The phase singularities in a polarized speckle pattern, in general, are not radially symmetric in intensity nor in phase. With some simple considerations it is possible to point out that they have an elliptic shape and, within the same model illustrated in appendix A.1 it is possible to calculate the statistical distribution of the ellipse eccentricity, as shown in references [Ber78, SS96, FF97, Den04].

Phase singularities occur in a field at points where amplitude is zero. If in a volume V we take a speckle field $\psi(\mathbf{r})$ (omitting time dependence) and we write it as the sum of its real and imaginary parts

$$\psi(\mathbf{r}) = \xi(\mathbf{r}) + i\eta(\mathbf{r}) \quad (\text{A.6.1})$$

the phase singularities are the intersection lines of the two surfaces identified by

$$\begin{cases} \xi(\mathbf{r}) = 0 \\ \eta(\mathbf{r}) = 0 \end{cases} \quad (\text{A.6.2})$$

These nodal lines, (illustrated in figure A.9) are randomly oriented and therefore are not specifically aligned with the propagation axis. Given a field in a volume, lines can cross it or appear and collapse in loops. Their trajectory in space has the characteristics of a random walk [DOP09]. Any arbitrarily plane in the volume V is pierced by these lines in several points, which represent the 2D phase singularities, or the dark spots of a speckle pattern.

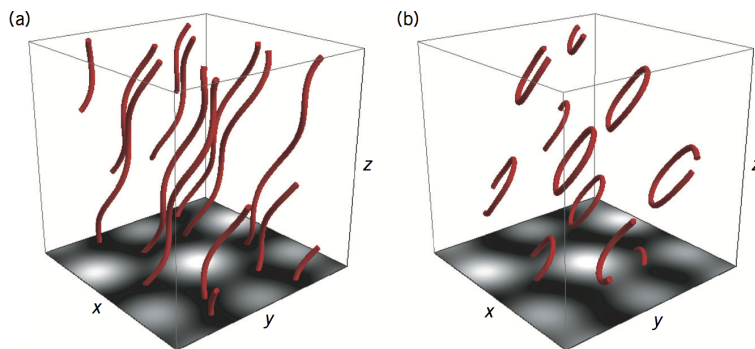


Figure A.9 – Illustration of phase singularities lines in a 3D speckle pattern. The lines can cross the volume (a) or form closed loops (b) (image source [DOP09]).

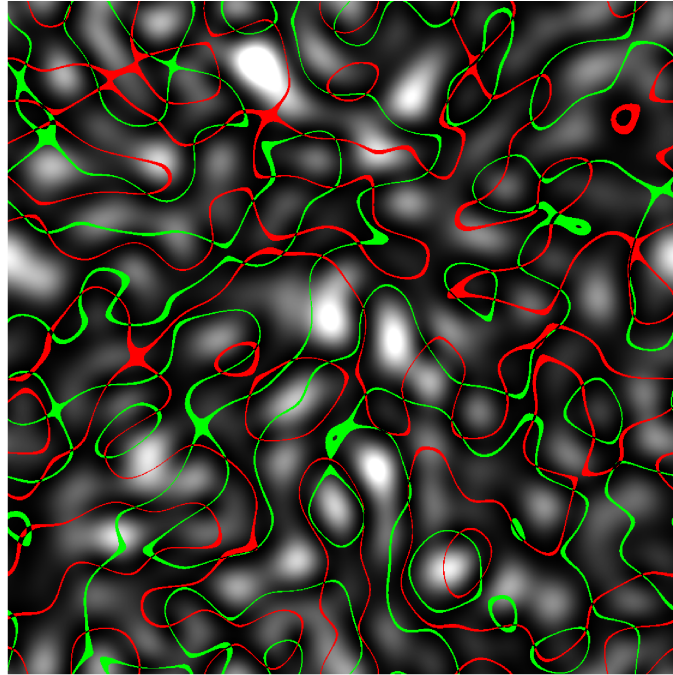


Figure A.10 – a speckle pattern and the lines representing the equations $\mathcal{R} = 0$ (red) and $\mathcal{I} = 0$ (green), where \mathcal{R} and \mathcal{I} are the real and imaginary part of the field. Phase singularities corresponds to intensity zeros, which occur when the lines cross each other.

Where the intensity is exactly zero, the field can be approximated with a Taylor expansion to the first order. If we choose the axis origin to be centred on the singularity with $\hat{\mathbf{e}}_x$ and $\hat{\mathbf{e}}_y$ lying on the plane, the approximated field rewrites as

$$\psi(\mathbf{r}) = \mathbf{r} \cdot \nabla \xi(0) + i\mathbf{r} \cdot \nabla \eta(0) \quad (\text{A.6.3})$$

Locally the amplitude of the field $\rho^2(\mathbf{r}) = \xi(\mathbf{r})^2 + \eta(\mathbf{r})^2$ can then be expressed as

$$\rho^2(\mathbf{r}) = (\mathbf{r} \cdot \nabla \xi(0))^2 + (\mathbf{r} \cdot \nabla \eta(0))^2 \quad (\text{A.6.4})$$

The quadratic form of $\rho^2(\mathbf{r})$ implies that the local curves of constant intensities are ellipses. To help visualizing this, we have plotted in the first column of A.11 the magnitude and phase of some singularity with different ellipticity. On the intersection plane, defined by $r_z = 0$ for example

$$\rho^2(\mathbf{r}) = C^2 \quad (\text{A.6.5})$$

$$(\mathbf{r} \cdot \nabla \xi(0))^2 + (\mathbf{r} \cdot \nabla \eta(0))^2 = C^2 \quad (\text{A.6.6})$$

$$(\xi_x x + \xi_y y)^2 + (\eta_x x + \eta_y y)^2 = C^2 \quad (\text{A.6.7})$$

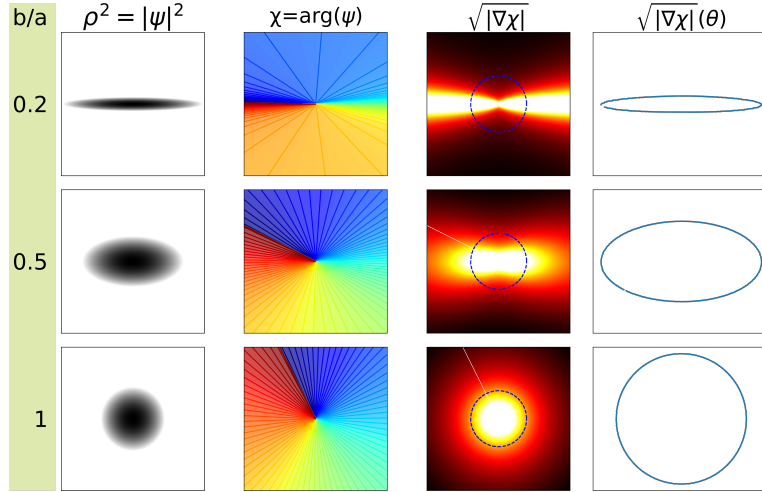


Figure A.11 – This figure illustrates the ellipses described by the intensity and phase around a singularity. Three singularities are plotted with equation (A.6.3), each one has a different ratio of the semi-axes a/b , which is indicated in the left-most label column. The first column shows the square modulus ρ^2 of the field for the three singularities, the images are saturated to put in evidence the elliptical profile. The phase χ of the field is plotted in the second column and the third represents the quantity $\sqrt{|\nabla\chi|^2}$. The fourth column shows the polar plot of $\sqrt{|\nabla\chi|^2}$ traced as a function of the angle when following the blue dotted circle plotted in column three. Finally we find in the ellipses of the fourth column, the same eccentricity of the ellipses in the first column.

and by choosing a rotation of the x and y axis where the mixed products cancels out $\xi_x\xi_y = -\eta_x\eta_y$ we obtain the canonical form of an ellipse,

$$x^2(\xi_x^2 + \eta_x^2) + y^2(\eta_y^2 + \xi_y^2) = C^2 \quad (\text{A.6.8})$$

$$\left(\frac{x}{a}\right)^2 + \left(\frac{y}{b}\right)^2 = C^2 \quad (\text{A.6.9})$$

with the semi-axes $a^2 = (\xi_x^2 + \eta_x^2)^{-1}$ and $b^2 = (\xi_y^2 + \eta_y^2)^{-1}$

The eccentricity of an ellipse is defined as $0 < \epsilon = \sqrt{1 - b^2/a^2} < 1$, an ellipse with $\epsilon = 0$ is a circle and the limit $\epsilon = 1$ corresponds to a parabola. The eccentricity distribution in a polarized speckle pattern is [BD00]

$$\rho_\epsilon(\epsilon) = \frac{8\epsilon^3}{(2 - \epsilon^2)^3} \quad (\text{A.6.10})$$

with mean value $E[\epsilon] = 0.869$ and variance $\sigma^2 = 0.772$. Reported in terms of the semi-axes ratio, the expected value of $q = b/a$ is $\simeq 0.49$, which means that the most probable ellipse has a ratio $\simeq 2 : 1$.

For the sake of a more immediate visualization, we rewrite this probability density in terms

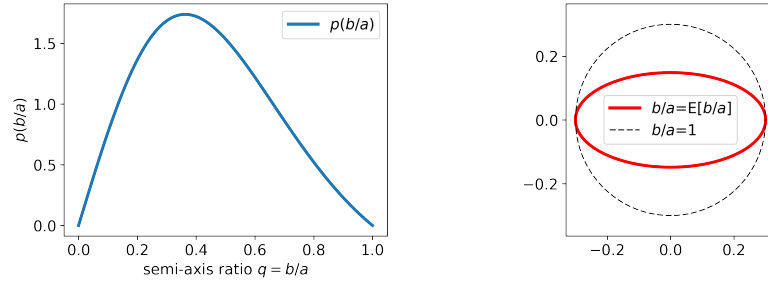


Figure A.12 – PDF of the ratio b/a of the intensity (and phase gradient) profile around phase singularities profiles in a polarized speckle pattern (left). Representation of an ellipse with $b/a = 0.5$ (right).

of the ratio of the ellipse semi-axis $q = b/a$, with the implicit assumption that $b < a$. We obtain

$$\rho_q(q) = \frac{8q(1 - q^2)}{(1 + q^2)^3} \quad (\text{A.6.11})$$

This probability density function is plotted in figure A.12. The expected value of the ratio a/b is 0.5. Interestingly, the probability of finding circular profiles ($b/a \approx 1$) or very elongated ones ($b/a \approx 0$) are the smallest.

It is interesting to look also at the phase around the singularity. Let us now write the same field as $\psi(\rho, \chi) = \rho e^{i\chi}$. The optical current associated to this field is

$$\mathbf{J} = \text{Im}(\psi^* \nabla \psi) = \rho^2 \nabla \chi$$

which has the direction of the phase gradient. Another quantity that we need is the *vorticity* vector defined as

$$\boldsymbol{\Omega} = \frac{1}{2} \nabla \times \mathbf{J} = \frac{1}{2} \text{Im}(\nabla \psi^* \times \nabla \psi) = \nabla \xi \times \nabla \eta$$

whose sign determines the circulation of \mathbf{J} around the phase singularity.

In the linear approximation of the field around a phase singularity, the current can be approximated by

$$\mathbf{J} \approx \boldsymbol{\Omega}(\mathbf{0}) \times \mathbf{r}$$

$\boldsymbol{\Omega}(\mathbf{0})$ is a constant vector, so the curves where $|\mathbf{J}|$ is constant are concentric circles around the singularities and \mathbf{J} (the current) circulates around it exactly as it happens in a vortex in fluids.

The last approximation allows writing the phase as

$$\nabla \chi(\mathbf{r}) = \frac{\mathbf{J}}{\rho^2} \approx \frac{\boldsymbol{\Omega}(\mathbf{0})}{(\mathbf{r} \cdot \nabla \xi(0))^2 + (\mathbf{r} \cdot \nabla \eta(0))^2} \times \mathbf{r}$$

demonstrating that along a circle coaxial with the singularity line, $\nabla \chi$ describes an ellipses of

the same eccentricity as ρ^2 . We have plotted the profile and phase of some configurations in figure A.11, that have different eccentricity values.

Axial field

In polarized speckle patterns focused with high NA objectives, the axial field amplitude at the centre of vortices depends on their topological characteristics and on the polarization state of the beam (a detailed explanation was given in the previous section).

Without loss of generality, let us choose Cartesian coordinates centred on a given optical vortex and aligned with the main axes of its characteristic ellipse. At first order expansion, the transverse field may then be written:

$$\mathbf{E}_\perp = \left(\frac{x}{a} + i\sigma \frac{y}{b} \right) (\cos \theta \mathbf{e}_x + e^{i\varphi} \sin \theta \mathbf{e}_y) \quad (\text{A.6.12})$$

where $\sigma = \pm 1$ is the topological charge of the vortex, θ the angle of the polarization ellipse with respect to the x -axis and φ the relative phase between the x and y components of the transverse field. Using the Maxwell-Gauss equation ($\nabla \cdot \mathbf{E} = 0$), we obtain the axial field in the paraxial approximation:

$$E_z = \frac{1}{ik} \left(\frac{\cos \theta}{a} + i\sigma e^{i\varphi} \frac{\sin \theta}{b} \right) \quad (\text{A.6.13})$$

where k is the wavenumber. **The axial field is thus canceled at the vortex center of \mathbf{E}_\perp if the beam is elliptically polarized with the same handedness ($e^{i\varphi} = i\sigma$), the same ellipticity ($\tan \theta = b/a$) and the same orientation as the vortex.** Since vortices in random waves contain a broad statistical distribution of ellipticities, intensity cannot be canceled at all vortices at once. Typically, a linearly x -polarized beam minimizes intensity at vortices strongly elongated along the x dimension, and circular polarization minimizes intensity at vortices of same handedness [PTEG16]. For imaging application, optimization of isotropic vortices is preferable in order to obtain isotropic super-resolution in the transverse plane.

Appendix B

Noise model in saturated speckle patterns

We can model the distribution of intensity of a saturated speckle pattern recorded by scanning a fluorescent point-like object. The speckle intensity distribution is

$$\rho_I(I) = \frac{1}{\langle I \rangle} e^{-\frac{I}{\langle I \rangle}} \quad (\text{B.0.1})$$

Whereas the fluorescence collected in pulsed mode is

$$I_F = F_0(1 - e^{-\frac{I}{I_s}} + C/F_0) \quad (\text{B.0.2})$$

where F_0 is the maximum fluorescence intensity (obtained at saturation), I_s is the FP saturation intensity, I is the illumination intensity and C is a constant background noise. We can calculate the intensity distribution of I_F with the transformation $\rho_F(I_F) = \rho_I(I_F) \frac{dI}{dI_F}$ and we obtain

$$\rho_F(I_F) = -\frac{1}{s} \left(1 + \frac{C}{F_0} + \frac{I_F}{F_0} \right)^{\frac{1}{s}-1} \quad (\text{B.0.3})$$

with $s = \frac{I_s}{\langle I \rangle}$.

The PFD of finding a value of intensity I in a saturated speckle pattern, considering also Poissonian photon noise is

$$P(I) = \sum_{I_F=0}^{F_0} P_\phi(I, I_F) \rho_F(I_F) \quad (\text{B.0.4})$$

where $P_\phi(I, I_F)$ represents the Poissonian probability of the photon count corresponding to the intensity I , knowing that the measured intensity is I_F . In figure B.1 we plot a numerical simulation and experimental results.

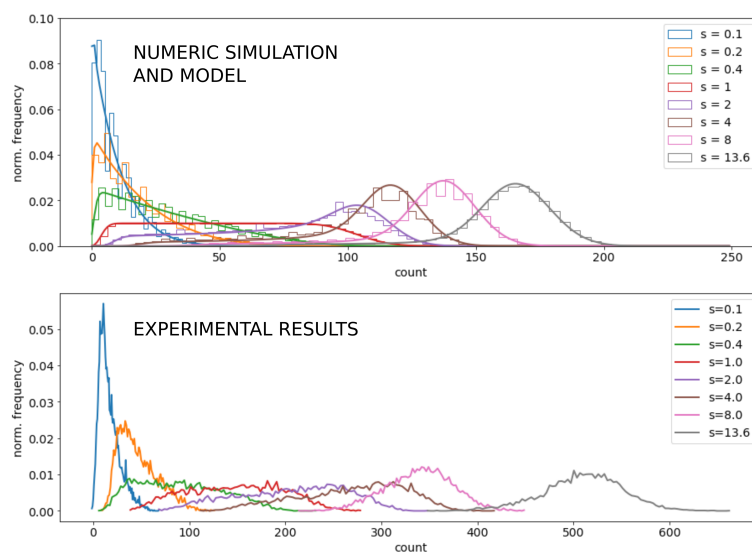


Figure B.1 – The upper plot shows the result of a numerical simulation of the intensity distribution in saturated speckle patterns with increasing saturation parameter. On top of the histograms, our model prediction is plotted with continuous lines. The lower plot shows the intensity distribution as experimentally measured on saturated speckle patterns. A strong shift of the histogram can be seen in the experimental data which is probably due to linear parasite background fluorescence, which increases with excitation intensity and is not accounted for in our simple model.

Appendix C

Fluorescence model under pulsed illumination

In chapter 1 we have mentioned the fluorescence model for a simple 2-levels system. This model is described by the following system of differential equations:

$$\begin{cases} \frac{d}{dt}r_0 = -k_e r_0 + k_f r_1 \\ \frac{d}{dt}r_1 = k_e r_0 - k_f r_1 \\ r_0(t) + r_1(t) = 1 \quad \forall t \end{cases} \quad (\text{C.0.1})$$

Where r_0 and r_1 are the occupation rates of the ground and excited levels respectively. The fluorescence signal at a given time is proportional to the occupation of the excited state, hence to $r_1 k_f$.

The excitation intensity I appears in the excitation rate $k_e = \frac{\sigma I}{h\nu}$ together with the fluorophore's absorption cross-section σ and the excitation photon energy $h\nu$. k_e is the excitation rate, represents the probability of a fluorophore to be excited and increases linearly with I .

A solution of (C.0.1) can be found by elimination of r_0 in the second equation with the third. The problem becomes

$$\frac{d}{dt}r_1 + r_1(k_e + k_f) = k_e$$

Which is a linear differential equation with constant coefficients. The solution corresponding to the initial condition $r_1(0) = 0$ is

$$r_1(t) = \frac{s}{s+1} \left[e^{-(s+1)k_f t} - 1 \right] \quad (\text{C.0.2})$$

with the saturation parameter $s = I/I_s = k_e/k_f$.

In case of CW excitation, the system evolves to a steady state that can be found imposing

the time derivatives of the system equations to be zero.

$$r_1 = \frac{k_e}{k_f + k_e} = \frac{s}{1 + s} \quad (\text{C.0.3})$$

where $I_s = \frac{h\nu k_f}{\sigma}$. If $I_s = I$ the steady state is a perfect balanced equilibrium between the two fluorophore populations:

$$r_1 = r_0 = 1/2 \quad (\text{C.0.4})$$

By looking at the plot (fig 1.11) of the steady state level vs. the excitation intensity, it is clear why I_s is called saturation intensity. Before this particular value of I, the ratio of excited fluorophores follows linearly the excitation intensity. After the system saturates and the excited population reaches a plateau.

In the case of a pulsed excitation with a pulse duration τ_p much shorter than the fluorescence mean life-time $\tau_p \ll \tau_f = 1/k_f$, and with an intensity for which $k_e \gg k_f$ some simplifications to the model can be done. We can for example say that the system, during the pulse excitation, does not de-excite at all, because it doesn't have the time to. In this case the system of equation becomes trivial

$$\begin{cases} \frac{d}{dt} r_0 = -k_e r_0 \\ \frac{d}{dt} r_1 = k_e r_0 \\ r_0(t) + r_1(t) = 1 \quad \forall t \end{cases} \quad (\text{C.0.5})$$

And the solution of the problem with $r_1(0) = 0$ is:

$$r_1(t) = 1 - e^{-k_e \tau_p} \quad (\text{C.0.6})$$

Which is also the normalized fluorescence intensity (per pulse) as a function of the saturation parameter s

$$f = 1 - e^{-k_e \tau_p} = 1 - e^{-s} \quad (\text{C.0.7})$$

Order of magnitude of I_s In order to give an example of the saturation intensity for fluorescence excitation, we take the example of the dye ATTO-532 which has

- absorption cross section $\sigma = 19 \times 10^{-16} \text{ cm}^2$
- wavelength of peak emission $\lambda_e = 532 \text{ nm}$

- mean fluorescence life-time $\tau_f = 3.8$ ns

Which gives a saturation intensity of

$$I_s = \frac{he}{\sigma\tau_f} = \frac{hc}{\sigma\tau_f\lambda_e} = 517 \text{ kW/cm}^{-2}$$

with the light speed in vacuum $c = 299\,792\,458 \text{ m s}^{-1}$ and the Plank constant $h = 6.626 \times 10^{-34} \text{ J s}$.

Appendix D

Wiener and RL deconvolution

In the reconstruction of saturated speckle images we make mostly use of the Wiener algorithm and sometimes the Richardson-Lucy one. Here we will see in detail the former and underline the differences with the second.

In a system where the image y is convolved with a PSF h and disturbed by a noise n

$$y = (x \otimes h) + n$$

the goal of the deconvolution filter is to find a function g so that \hat{x} can be recovered as

$$\hat{x} = (g \otimes y)$$

where x and \hat{x} are as similar as possible. The Wiener version of g is obtained through the minimization of the mean square error between X and \hat{X} , where, with capital letter, we denote the Fourier Transform. Therefore one imposes the cost function:

$$rms = E [|\hat{X} - X|^2] = E [(GH - 1)X - GN|^2] \quad (D.0.1)$$

to be minimum. With the hypothesis of statistical independence between noise and signal, this minimization leads to [Bur01]

$$G = \frac{H^* E[|X|^2]}{|H|^2 E[|X|^2] + E[|N|^2]} \quad (D.0.2)$$

or dividing by $S = E[|X|^2]$

$$G = \frac{H^*}{|H|^2 + \epsilon} \quad (D.0.3)$$

In the two last equations, $E[|X|^2]$ and $E[|N|^2]$ are the expected value of the power spectra of the signal and noise respectively, so that $\epsilon = \frac{E[|N|^2]}{E[|X|^2]}$ represents how strong is the average noise

compared to the signal. In practice, ϵ is the only parameter that the algorithm requires for the image restoration and in most cases it is empirically estimated. Although Wiener filtering demands very little resources, because it reduces to the calculation of some Fourier Transforms and some algebraic operations, it does not take advantage of any other constraints applicable to the the image x or the noise n as other algorithms do.

One of the most largely employed deconvolution algorithm is the Richardson-Lucy one [Luc74, Ric72]. It is s a maximum-likelihood approach, like Wiener's filter. The difference is that RL assumes that the noise follows a Poisson distribution, which leads to the minimization of the cost function

$$r(x) = hx - y \log(hx) \quad (\text{D.0.4})$$

which is done iteratively over an arbitrarily chosen number of iterations.

Since Wiener filtering has a more intuitive derivation, does the least assumptions and is extremely fast, we have preferred it to RL in general. As can be seen in figure D.1, the RL algorithm yields reconstructions with a better S/N ratio, but this difference is more aesthetic than functional. Therefore all deconvolution shown in this work use Wiener filtering, if not explicitly said. Only in the case of speckle images with very low signal to noise ratio, the RL algorithm has shown to perform better than Wiener.

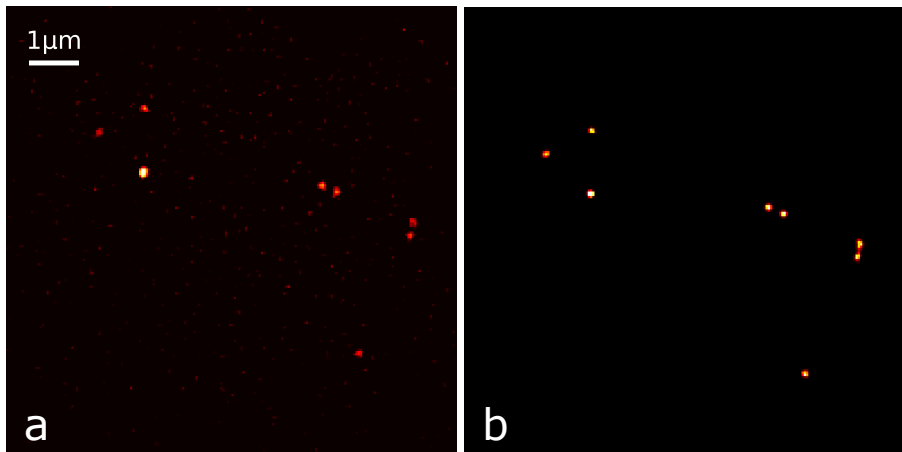


Figure D.1 – Comparison of reconstructed images shown in Fig. 3.5 using Wiener deconvolution (a) and Richardson-Lucy deconvolution (b). Richardson-Lucy deconvolution improves the signal to noise ratio.

Appendix E

Acronyms

- **BE** : Beam Expander
- **BS** : Beam Splitter
- **FOV** : Field Of View
- **FP** : FluoroPhore
- **MFP** : Mean Free Path
- **NA** : Numerical Aperture
- **OTF** : Optical Transfer function (see eq. 1.1.2)
- **PALM** : Photo-activated Localization Microscopy
- **PDF** : Probability Density Function
- **PMT** : Photo-Multiplier Tube
- **PR** : Phase Retrieval
- **PSF** : Point Spread Function (see eq.1.1.1)
- **SIM** : Structured Illumination Microscopy
- **SLM** : Spacial Light Modulator
- **SR** : Super-Resolution
- **STORM** : Stochastic Optical Reconstruction Microscopy
- **SsPSF** : Saturated speckle Point Spread Function
- **sPSF** : speckle Point Spread Function

Bibliography

- [Abb81] E. Abbe, *On the Estimation of Aperture in the Microscope.*, Journal of the Royal Microscopical Society **1** (1881jun), no. 3, 388–423.
- [Aga84] D A Agard, *Optical Sectioning Microscopy: Cellular Architecture in Three Dimensions*, Annual Review of Biophysics and Bioengineering **13** (1984jun), no. 1, 191–219.
- [AYT⁺11] Claudia G Almeida, Ayako Yamada, Daniele Tenza, Daniel Louvard, Graca Raposo, and Evelyne Coudrier, *Myosin 1b promotes the formation of post-Golgi carriers by regulating actin assembly and membrane remodelling at the trans-Golgi network*, Nature Cell Biology **13** (2011jul), no. 7, 779–U424.
- [BD00] M V Berry and M R Dennis, *Phase singularities in isotropic random waves*, Proc. R. Soc. A-Mat **456** (2000sep), no. 2001, 2059–2079.
- [Ber78] M V Berry, *Disruption of wavefronts: statistics of dislocations in incoherent Gaussian random waves*, J. Phys. A: Math. Gen. **11** (1978), no. 1, 27.
- [BPS⁺06] Eric Betzig, George H Patterson, Rachid Sougrat, O Wolf Lindwasser, Scott Olenych, Juan S Bonifacino, Michael W Davidson, Jennifer Lippincott-Schwartz, and Harald F Hess, *Imaging Intracellular Fluorescent Proteins at Nanometer Resolution*, Science **313** (2006), no. 5793, 1642–1645.
- [Bur01] Gilles Burel, *Introduction au traitement d’images: Simulation sous Matlab* (Lavoisier, ed.), 2001.
- [BvPB⁺12] Jacopo Bertolotti, Elbert G van Putten, Christian Blum, Ad Lagendijk, Willem L Vos, and Allard P Mosk, *Non-invasive imaging through opaque scattering layers.*, Nature **491** (2012), no. 7423, 232–4, available at [ArXiv:1403.3316](https://arxiv.org/abs/1403.3316).
- [dAGB15] Hilton B de Aguiar, Sylvain Gigan, and Sophie Brasselet, *Polarization-resolved microscopy through scattering media via wavefront shaping*, arXiv preprint arXiv:1511.02347 (2015).
- [DEH07] Gerald Donnert, Christian Eggeling, and Stefan W Hell, *Major signal increase in fluorescence microscopy through dark-state relaxation*, Nat. Methods **4** (2007), no. 1, 81–86.
- [Den01] Mark Dennis, *Local properties and statistics of phase singularities in generic wavefields*, International society for optical engineering, 2001.

- [Den04] M R Dennis, *Local phase structure of wave dislocation lines: twist and twirl*, Journal of optics A - Pure and applied optics **6** (2004may), no. 5, S202–S208.
- [DOP09] Mark R Dennis, Kevin O’Holleran, and Miles J Padgett, *Chapter 5 Singular Optics: Optical Vortices and Polarization Singularities*, 2009, pp. 293–363.
- [DTS09] Jun B. Ding, Kevin T. Takasaki, and Bernardo L. Sabatini, *Superesolution Imaging in Brain Slices using Stimulated-Emission Depletion Two-Photon Laser Scanning Microscopy*, Neuron **63** (2009aug), no. 4, 429–437.
- [EH14] Ulrike Endesfelder and Mike Heilemann, *Direct stochastic optical reconstruction microscopy (Dstorm)*, Methods in Molecular Biology **1251** (2014), 263–276.
- [ES16] Eitan Edrei and Giuliano Scarcelli, *Memory-effect based deconvolution microscopy for super-resolution imaging through scattering media*, Nature Publishing Group **6** (2016dec), no. September, 1–8.
- [FF97] I Freund and V Freilikher, *Parameterization of anisotropic vortices*, Journal of the optical society of america A-optics of the image science and vision **14** (1997aug), no. 8, 1902–1910.
- [Fie13] James R Fienup, *Phase retrieval algorithms: a personal tour*, Appl. Opt. **52** (2013jan), no. 1, 45–56.
- [FKK⁺07] Katsumasa Fujita, Minoru Kobayashi, Shogo Kawano, Masahito Yamanaka, and Satoshi Kawata, *High-resolution confocal microscopy by saturated excitation of fluorescence*, Physical Review Letters **99** (2007nov), no. 22, 1–4.
- [FKLS88] S C Feng, C Kane, P A Lee, and A D Stone, *Correlation and fluctuations of coherent wave transmission through disordered media*, Phys. Rev. Lett. **61** (1988), no. 7, 834–837.
- [F.R79] Lord Rayleigh F.R.S., *XXXI. Investigations in optics, with special reference to the spectroscope*, Philosophical Magazine **8** (1879), no. 49, 261–274.
- [Fre90] Isaac Freund, *Looking through walls and around corners*, Physica A: Statistical Mechanics and its Applications **168** (1990), no. 1, 49–65, available at [arXiv:1011.1669v3](https://arxiv.org/abs/1011.1669v3).
- [FRF88] Isaac Freund, Michael Rosenbluh, and Shechao Feng, *Memory effects in propagation of optical waves through disordered media*, Physical Review Letters **61** (1988), no. 20, 2328–2331.
- [GGP⁺03] N. Ghosh, P. K. Gupta, H. S. Patel, B. Jain, and B. N. Singh, *Depolarization of light in tissue phantoms - Effect of collection geometry*, Optics Communications **222** (2003), no. 1-6, 93–100.
- [GHV⁺12] Silvia Galiani, Benjamin Harke, Giuseppe Vicidomini, Gabriele Lignani, Fabio Benfenati, Alberto Diaspro, and Paolo Bianchini, *Strategies to maximize the performance of a STED microscope*, Opt. Express **20** (2012mar), no. 7, 7362–7374.

- [GKR98] E. E. Gorodnichev, a. I. Kuzovlev, and D. B. Rogozkin, *Diffusion of circularly polarized light in a disordered medium with large-scale inhomogeneities*, Journal of Experimental and Theoretical Physics Letters **68** (1998), no. 1, 22–28.
- [Goo06] J W Goodman, *Speckle Phenomena in Optics*, Roberts and Cie, 2006.
- [Goo15] Joseph W Goodman, *Statistical optics*, John Wiley & Sons, 2015.
- [GRG17] Jérôme Gateau, Hervé Rigneault, and Marc Guillon, *Complementary Speckle Patterns: Deterministic Interchange of Intrinsic Vortices and Maxima through Scattering Media*, Physical Review Letters **118** (2017), no. 4, available at [ArXiv:1607.06722](https://arxiv.org/abs/1607.06722).
- [GS72] R W Gerchberg and W Owen Saxton, *A practical algorithm for the determination of the phase from image and diffraction plane pictures*, Optik **35** (1972), 237–246.
- [GTL⁺11] Tim Grotjohann, Ilaria Testa, Marcel Leutenegger, Hannes Bock, Nicolai T Urban, Flavie Lavoie-Cardinal, Katrin I Willig, Christian Eggeling, Stefan Jakobs, and Stefan W Hell, *Diffraction-unlimited all-optical imaging and writing with a photochromic GFP*, Nature **478** (2011), no. 7368, 204–208.
- [Gus00] M. G. L. Gustafsson, *Surpassing the lateral resolution limit by a factor of two using structured illumination microscopy*, Journal of microscopy - Oxford **198** (2000may), no. 2, 82–87.
- [Gus05] Mats G L Gustafsson, *Nonlinear structured-illumination microscopy: Wide-field fluorescence imaging with theoretically unlimited resolution*, Proc. Natl. Acad. Sci. USA **102** (2005sep), no. 37, 13081–13086.
- [HBE⁺09] Jana Humpolickova, Aleš Ales Benda, Joerg Jörg Enderlein, Jana Humpolíčková, Aleš Ales Benda, and Joerg Jörg Enderlein, *Optical saturation as a versatile tool to enhance resolution in confocal microscopy*, Biophysical Journal **97** (2009nov), no. 9, 2623–2629.
- [Hei03] R Heintzmann, *Saturated patterned excitation microscopy with two-dimensional excitation patterns*, MICRON **34** (2003), no. 6-7, 283–291.
- [HJC02] Rainer Heintzmann, T M Jovin, and C Cremer, *Saturated patterned excitation microscopy - a concept for optical resolution improvement*, Journal of the optical society of america A-optics of the image science and vision **19** (2002aug), no. 8, 1599–1609.
- [HKU⁺08] Benjamin Harke, Jan Keller, Chaitanya K. Ullal, Volker Westphal, Andreas Schoenle, Stefan W. Hell, Andreas Schönle, and Stefan W. Hell, *Resolution scaling in STED microscopy*, Opt. Express **16** (2008mar), no. 6, 4154–4162.
- [HW94a] S W Hell and J Wichmann, *Breaking the diffraction resolution limit by stimulated-emission-depletion fluorescence microscopy*, Opt. Lett. **19** (1994), no. 11, 780–782.
- [HW94b] Stefan W Hell and Jan Wichmann, *Stimulated-Emission-Depletion Fluorescence Microscopy*, Optics Letters **19** (1994), no. 11, 780–782.

- [Jac01] J D Jackson, *Electrodynamique classique*, Dunod, 2001.
- [JHV⁺15] Benjamin Judkewitz, Roarke Horstmeyer, Ivo M. Vellekoop, Ioannis N. Papadopoulos, and Changhui Yang, *Translation correlations in anisotropically scattering media*, Nature Physics **11** (2015jun), no. June, 1–6, available at [ArXiv:1411.7157](https://arxiv.org/abs/1411.7157).
- [KHFG14] Ori Katz, Pierre Heidmann, Mathias Fink, and Sylvain Gigan, *Non-invasive real-time imaging through scattering layers and around corners via speckle correlations*, Nature Photonics **8** (2014mar), no. 10, 784–790, available at [ArXiv:1403.3316](https://arxiv.org/abs/1403.3316).
- [KSH07] Jan Keller, Andreas Schönle, and Stefan W Hell, *Efficient fluorescence inhibition patterns for RESOLFT microscopy*, Opt. Express **15** (2007mar), no. 6, 3361–3371.
- [KSS12] Ori Katz, Eran Small, and Yaron Silberberg, *Looking through walls and around corners with incoherent light : Wide-field real-time imaging through scattering media*, [Http://Arxiv.Org/Abs/1202.2078V1](http://arxiv.org/abs/1202.2078v1) (2012), 1–10.
- [Lab70] Antoine Labeyrie, *Attainment of diffraction limited resolution in large telescopes by Fourier analysing speckle patterns in star images*, Astron. Astrophys. **6** (1970), no. 1, 85–87.
- [LAI⁺16] Simon Labouesse, Marc Allain, Jérôme Idier, Sébastien Bourguignon, Penghuan Liu, and Anne Sentenac, *Blind fluorescence structured illumination microscopy: A new reconstruction strategy*, GretsI, 2016, pp. 2–5.
- [LC11] Bonnie O Leung and Keng C Chou, *Review of super - Resolution fluorescence microscopy for biology*, Vol. 65, 2011.
- [LDCP05] J Leach, M R Dennis, J Courtial, and M J Padgett, *Vortex knots in light*, New. J. Phys. **7** (2005).
- [LGSE13] Marcel A Lauterbach, Marc Guillon, Asma Soltani, and Valentina Emiliani, *STED microscope with Spiral Phase Contrast*, Sci. Rep. **3** (2013jun).
- [Luc74] L. B. Lucy, *An iterative technique for the rectification of observed distributions*, The Astronomical Journal **79** (1974jun), 745, available at [arXiv:1011.1669v3](https://arxiv.org/abs/1011.1669v3).
- [MBG⁺12] E Mudry, K Belkebir, J Girard, J Savatier, E Le Moal, C Nicoletti, M Allain, and A Sentenac, *Structured illumination microscopy using unknown speckle patterns*, Nat. Photon. **6** (2012may), no. 5, 312–315.
- [Ntz10] Vasilis Ntziachristos, *Going deeper than microscopy: the optical imaging frontier in biology*, Nature Methods **7** (2010aug), no. 8, 603–614.
- [OHP⁺17] Gerwin Osnabrugge, Roarke Horstmeyer, Ioannis N Papadopoulos, Benjamin Judkewitz, and Ivo M Vellekoop, *Generalized optical memory effect*, Optica **4** (2017aug), no. 8, 886–892.
- [PBM99] E J G Peterman, S Brasselet, and W E Moerner, *The fluorescence dynamics of single molecules of green fluorescent protein*, J. Phys. Chem. A **103** (1999), no. 49, 10553–10560.

- [PDMLS10] George Patterson, Michael Davidson, Suliana Manley, and Jennifer Lippincott-Schwartz, *Superresolution Imaging using Single-Molecule Localization*, Annual Review of Physical Chemistry **61** (2010mar), no. 1, 345–367.
- [PLC⁺10] S. M. Popoff, G. Lerosey, R. Carminati, M. Fink, A. C. Boccara, and S. Gigan, *Measuring the Transmission Matrix in Optics: An Approach to the Study and Control of Light Propagation in Disordered Media*, Phys. Rev. Lett. **104** (2010mar), no. 10, 100601, available at [ArXiv:0910.5436](https://arxiv.org/abs/0910.5436).
- [POA⁺13] Julien Pernier, Jozsef Orban, Balendu Sankara Avvaru, Antoine Jegou, Guillaume Romet-Lemonne, Berengere Guichard, and Marie-France Carlier, *Dimeric WH2 domains in Vibrio VopF promote actin filament barbed-end uncapping and assisted elongation*, Nature structural & molecular biology **20** (2013sep), no. 9, 1069+.
- [PTEG16] Marco Pascucci, Gilles Tessier, Valentina Emiliani, and Marc Guillon, *Superresolution Imaging of Optical Vortices in a Speckle Pattern*, Phys. Rev. Lett. **116** (2016mar), no. 9, 93904.
- [RBZ06] Michael J Rust, Mark Bates, and Xiaowei W Zhuang, *Sub-diffraction-limit imaging by stochastic optical reconstruction microscopy (STORM)*, Nat Methods **3** (2006), no. 10, 793–795.
- [Ric72] William Hadley Richardson, *Bayesian-Based Iterative Method of Image Restoration*, Journal of the Optical Society of America **62** (1972jan), no. 1, 55.
- [RSM⁺12] E Hesper Rego, Lin Shao, John J Macklin, Lukman Winoto, Göran A Johansson, Nicholas Kamps-Hughes, Michael W Davidson, and Mats G L Gustafsson, *Nonlinear structured-illumination microscopy with a photoswitchable protein reveals cellular structures at 50-nm resolution*, Proceedings of the National Academy of Sciences **109** (2012jan), no. 3, E135–E143.
- [RWH09] E Rittweger, D Wildanger, and S W Hell, *Far-field fluorescence nanoscopy of diamond color centers by ground state depletion*, EPL **86** (2009), no. 1.
- [SDS⁺17] Daniel Sage, Laurene Donati, Ferreol Soulez, Denis Fortun, Guillaume Schmit, Arne Seitz, Romain Guiet, Cedric Vonesch, and Michael Unser, *DeconvolutionLab2: An open-source software for deconvolution microscopy*, Methods - Image Processing for Biologists **115** (2017feb), 28–41.
- [SHL10] Lothar Schermelleh, Rainer Heintzmann, and Heinrich Leonhardt, *A guide to super-resolution fluorescence microscopy*, Journal of Cell Biology **190** (2010), no. 2, 165–175.
- [Sib05] Jean-Baptiste Sibarita, *Deconvolution Microscopy*, Microscopy Techniques (2005may), 201–243.
- [SPM⁺09] Fedor V Subach, George H Patterson, Suliana Manley, Jennifer M Gillette, Jennifer Lippincott-Schwartz, and Vladislav V Verkhusha, *Photoactivatable mCherry for high-*

- resolution two-color fluorescence microscopy*, Nature Methods **6** (2009feb), no. 2, 153–159.
- [SS96] Y Y Schechner and J Shamir, *Parameterization and orbital angular momentum of anisotropic dislocations*, Journal of the optical society of america A -optics of the image science and vision **13** (1996may), no. 5, 967–973.
- [SSP11] Nadja Spitzer, Gregory S Sammons, and Elmer M Price, *Autofluorescent cells in rat brain can be convincing impostors in green fluorescent reporter studies*, Journal of neuroscience methods **197** (2011), no. 1, 48–55.
- [WON09] Jörg Wiedenmann, Franz Oswald, and Gerd Ulrich Nienhaus, *Fluorescent proteins for live cell imaging: Opportunities, limitations, and challenges*, Vol. 61, Wiley Subscription Services, Inc., a Wiley company, 2009.
- [WPS⁺12] Dominik Wildanger, Brian R. Patton, Heiko Schill, Luca Marseglia, J. P. Hadden, Sebastian Knauer, Andreas Schönle, John G. Rarity, Jeremy L. O’Brien, Stefan W. Hell, and Jason M. Smith, *Solid Immersion Facilitates Fluorescence Microscopy with Nanometer Resolution and Sub-Angström Emitter Localization*, Advanced Materials **24** (2012), no. 44, OP309–OP313.
- [WV11] Ashley J. Welch and Martin J C Van Gemert, *Optical-thermal response of laser-irradiated tissue*, Vol. 2, Springer, 2011.
- [YMLTW⁺14] Ayako Yamada, Alexandre Mamane, Jonathan Lee-Tin-Wah, Aurelie Di Cicco, Coline Prevost, Daniel Levy, Jean-Francois Joanny, Evelyne Coudrier, and Patricia Bassereau, *Catch-bond behaviour facilitates membrane tubulation by non-processive myosin 1b*, Nature Communications **5** (2014apr).
- [YTW17] Li-Hao Yeh, Lei Tian, and Laura Waller, *Structured illumination microscopy with unknown patterns and a statistical prior*, Biomedical Optics Express **8** (2017feb), no. 2, 695, available at [ArXiv:1611.00287](https://arxiv.org/abs/1611.00287).
- [ZG07] Sheng Zhang and Azriel Z Genack, *Statistics of diffusive and localized fields in the vortex core*, Phys. Rev. Lett. **99** (2007), no. 20.
- [ZKKO04] R Zondervan, F Kulzer, M A Kol’chenko, and M Orrit, *Photobleaching of rhodamine 6G in poly(vinyl alcohol) at the ensemble and single-molecule levels*, J. Phys. Chem. A **108** (2004mar), no. 10, 1657–1665.
- [ZKT⁺17] Guangyuan Zhao, Mohammad M Kabir, Kimani C. Toussaint, Cuifang Kuang, Cheng Zheng, Zhongzhi Yu, Xu Liu, Kimani C Toussaint Jr, Cuifang Kuang, Cheng Zheng, Zhongzhi Yu, and Xu Liu, *Saturated absorption competition microscopy*, Optica **4** (2017jan), no. 6, 1–14, available at [ArXiv:1701.06358](https://arxiv.org/abs/1701.06358).